Technische Universität Dresden

MILLIMETER-WAVE SUPER-REGENERATIVE RECEIVERS FOR WIRELESS COMMUNICATION AND RADAR

Hatem Ghaleb

der Fakultät Elektrotechnik und Informationstechnik
der Technischen Universität Dresden
zur Erlangung des akademischen Grades

Doktoringenieur
(Dr.-Ing.)

genehmigte Dissertation

Vorsitzender:	Prof. Dr.-Ing. Dirk Plettemeier
Gutachter:	Prof. Dr. sc. techn. habil. Frank Ellinger
	Prof. Dr.-Ing. Hermann Schumacher

Tag der Einreichung:	12. April 2022
Tag der Verteidigung:	14. Oktober 2022

Acknowledgments

First and foremost, I would like to thank my girlfriend, Carmen, for being the kindest and most supportive partner, and whom I love very much. She has helped me greatly through many shifting circumstances while building her own career. For this and many other reasons, I am sincerely in her gratitude. I am grateful to my parents, Nahla and Fayek, for their love and support, and for providing me the best education possible that prepared me for my Ph.D. research. I am thankful to my sister, Nariman, for her humbling belief in me and for many helpful and understanding conversations. I am incredibly grateful to the memory of my grandfather, Geddo Mohyee, who raised me to always respect science, and encouraged me to pursue my doctorate degree.

I would like to thank Prof. Frank Ellinger for the opportunity to study and work at the Chair for Circuit Design and Network Theory (CCN), as well as for his hard work to provide access to the best lab equipment and the fastest technologies. I owe a lot to my group leader, Niko Joram (Local Positioning and Radar Research Group), who has been a great boss and colleague, helping me with a wealth of scientific knowledge and an incredibly supportive personal attitude. Additionally, I am grateful for his review and improvement suggestions for the manuscript of this thesis.

I would like to thank Prof. Hermann Schumacher from Universität Ulm for my studies at the Communications Technology Master program, as well as my Bachelor thesis project. I have enjoyed and learned a great deal from his lectures about Modern Semiconductor Devices, Monolithic Microwave ICs in High-Speed Systems, and High-Frequency Microsystems. His lectures and research work at the Institut für Elektronische Bauelemente und Schaltungen (EBS) have had a strong positive impact on my interest and later career in millimeter-wave circuits and systems. I would also like to thank the EBS research scientists, especially Bernd Schleicher for supervising my Bachelor thesis, and Gang Liu for supervising my Master thesis.

I would like to thank Ali Ferschischi for the joint work on SRO theory and analysis, of which I included a small part in section 2.2, and for multiple other collaborations. I am grateful to Mohammed El-Shennawy for many exciting circuit design discussions and collaborations in which he shared insights from his technical expertise. I would like to thank David Fritsche for his pioneering work on millimeter-wave circuit design, and the many conversations and collaborations that led to the improvement of this work. I would also like to thank Mohammad Mahdi Khafaji for taking the time to discuss with me various circuit problems in detail, which always led to innovative design solutions and much learning on my side.

I am grateful to Sami Ur Rehman for sharing his excellent Ph.D. thesis with me, which was very helpful to me during the writing of my thesis. I would like to thank Paul Stärke for helping me with mixer measurement techniques and the waveguide packaging concepts used in section 3.7. I would also like to thank Florian Protze for lending me his wire bonding skills and many hours of his time at the height of a pandemic lockdown. I would like to thank my former students, Vaidhyanathan Elumalai, Georg Meller and Shaif Grover, for their motivation

and dedication throughout their thesis work. I especially thank Yu Zhu for a lot of hard work and a fun work relationship, leading to the results described in section 4.2 and others.

I am grateful to so many of my CCN colleagues for the enriching collaborations and discussions. Among others, they include Adrian Figueroa, Alexandru Giuglea, Amirali Taghavi, Andres Seidel, Belal Al-Qudsi, Corrado Carta, Felix Schwarze, Gregor Tretter, Guido Belfiore, Jan Pliva, Jens Wagner, László Szilágyi, Mantas Sakalas, Manu V. Thayyil, Marco Gunia, Markus Schulz, Marvin Barahona, Mengqi Cui, Naglaa El Agroudy, Reza Shabanpour, Robert Kostack, Robert Paulo, Rui Ma, Songhui Li, Stefan Schumann, Tom Drechsel, Udo Jörges, Vincent Rieß, and Zoltán Tibenszky.

I would like to thank the CCN administrative staff, Katharina Isaack, Anja Muthmann, and Peter Brandl, as well as the IT administrator, Frank Bindrich, for their help and support on many occasions.

I would like to thank the German Research Foundation (DFG) for publicly funding the majority of this scientific research work, through the research projects SPARS, MSPARS, and 3D-LommID. I am grateful to my research project partner from the Friedrich-Alexander-Universität Erlangen-Nürnberg (FAU), Christian Carlowitz, whose contributions and knowledge of wireless system concepts were instrumental to the results presented in section 3.6. I am also grateful to Thomas Girg from FAU and Xuan-Quang Du from Universität Stuttgart for the good partnership and their novel work on transmitter and analog-to-digital converter circuits.

I am incredibly grateful to my dear friend and colleague, Mohammad Alloh, from Technische Universität Dresden (TUD), for his help with Figure 3.47 and other editing work in this thesis. More than anything, I am thankful to him for sharing many good times together and being supportive through the difficult times. I am also grateful to TUD and the city of Dresden for many life experiences and beautiful memories during this unforgettable journey.

Abstract

Today's world is becoming increasingly automated and interconnected with billions of smart devices coming online, leading to a steep rise in energy consumption from small microelectronics. This coincides with an urgent push to transform global energy production to green energies, causing disruptions and energy shortages, and making the case for efficient energy use ever more pressing. Two major areas where high growth is expected are the fields of wireless communication and radar sensors. Millimeter-wave frequency bands are planned for fifth-generation (5G) and sixth-generation (6G) cellular communication standards, as well as automotive frequency-modulated continuous wave (FMCW) radar systems for driving assistance and automation. Fast silicon-based technologies enable these advances by operating at high maximum frequencies, such as the silicon-germanium (SiGe) heterojunction bipolar transistor (HBT) technologies. However, even the fastest transistors suffer from low and energy expensive gains at millimeter-wave frequencies.

Rather than incremental improvements in circuit efficiency using conventional approaches, a disruptive revolution for green microelectronics could be enabled by exploring the low-power benefits of the super-regenerative receiver for some applications. The super-regenerative receiver uses a regenerative oscillator circuit to increase the gain by positive feedback, through coupling energy from the output back into the input. Careful bias and control of the circuit enables a very large gain from a small number of transistors and a very low energy dissipation. Thus, the super-regenerative oscillator could be used to replace amplifier circuits in high data rate wireless communication systems, or as active reflectors to increase the range of FMCW radar systems, greatly reducing the power consumption.

The work in this thesis presents fundamental scientific research into the topic of energy-efficient millimeter-wave super-regenerative receivers for use in civilian wireless communication and radar applications. This research work covers the theory, analysis, and simulations, all the way up to the proof of concept, hardware realization, and experimental characterization. Analysis and modeling of regenerative oscillator circuits is presented and used to improve the understanding of the circuit operation, as well as design goals according to the specific application needs. Integrated circuits are investigated and characterized as a proof of concept for a high data rate wireless communication system operating between 140–220 GHz, and an automotive radar system operating at 60 GHz. Amplitude and phase regeneration capabilities for complex modulation are investigated, and principles for spectrum characterization are derived. The circuits are designed and fabricated in a 130 nm SiGe HBT technology, combining bipolar and complementary metal-oxide semiconductor (BiCMOS) transistors.

To prove the feasibility of the research concepts, the work achieves a wireless communication link at 16 Gbit/s over 20 cm distance with quadrature amplitude modulation (QAM), which is a world record for the highest data rate ever reported in super-regenerative circuits. This was powered by a super-regenerative oscillator circuit operating at 180 GHz and providing 58 dB of gain. Energy efficiency is also considerably high, drawing 8.8 mW of dc power consumption, which corresponds to a highly efficient 0.6 pJ/bit. Packaging and module inte-

gration innovations were implemented for the system experiments, and additional broadband circuits were investigated to generate custom quench waveforms to further enhance the data rate. For radar active reflectors, a regenerative gain of 80 dB is achieved at 60 GHz from a single circuit, which is the best in its frequency range, despite a low dc power consumption of 25 mW.

Zusammenfassung

Die moderne Welt wird zunehmend automatisiert und mit Milliarden von intelligenten Geräten vernetzt, was zu einem schnellen Anstieg des Energieverbrauchs kleiner mikroelektronischer Schaltungen führt. Dies fällt mit einem dringenden Vorstoß zusammen, die globale Energieerzeugung auf grüne Energie umzustellen, welche Störungen und Energieknappheiten verursacht. Zwei Hauptbereiche, in denen ein hohes Wachstum erwartet wird, sind die drahtlose Kommunikation und die Radarsensorik. Für die fünfte (5G) und sechste (6G) Generationen der mobilen Kommunikation, sowie frequenzmodulierte Dauerstrichradarsysteme (FMCW) zur Fahrassistenz und Automatisierung, sind Millimeterwellen-Frequenzbänder geplant. Schnelle siliziumbasierte Technologien ermöglichen diese Fortschritte, indem sie bei hohen Maximalfrequenzen arbeiten, wie z.B. mit dem Silizium-Germanium-Heterojunction-Bipolartransistor (SiGe-HBT). Allerdings ist es selbst für die schnellsten Transistoren sehr energieintensiv, im Bereich der Millimeterwellen nennenswerte Verstärkungsfaktoren zu erreichen.

Anstelle von inkrementellen Verbesserungen der Schaltungseffizienz unter Verwendung herkömmlicher Methoden könnte eine Revolution grüner Mikroelektronik ermöglicht werden, indem die Vorteile des superregenerativen Empfängers mit geringem Stromverbrauch für spezielle Anwendungen untersucht werden. Der Empfänger verwendet eine regenerative Oszillatorschaltung, um die Verstärkung durch positive Rückkopplung zu erhöhen, indem Energie vom Ausgang zurück in den Eingang gekoppelt wird. Eine sorgfältige Steuerung und Bestimmung des Arbeitspunktes der Schaltung ermöglicht eine sehr große Verstärkung mit einer kleinen Anzahl von Transistoren, und einen sehr geringen Energieverbrauch. Somit könnte der superregenerative Oszillator verwendet werden, um Verstärkerschaltungen in drahtlosen Kommunikationssystemen mit hoher Datenrate zu ersetzen, oder als aktive Reflektoren, um die Reichweite von FMCW-Radarsystemen zu erhöhen, wodurch der Stromverbrauch stark reduziert wird.

Die Arbeit in dieser Dissertation präsentiert wissenschaftliche Grundlagenforschung zum Thema energieeffiziente superregenerative Millimeterwellenempfänger für den Einsatz in zivilen drahtlosen Kommunikations- und Radaranwendungen. Diese Forschungsarbeit umfasst Theorie, Analyse und Simulationen bis hin zu Proof-of-Concept, Hardwarerealisierung und experimenteller Charakterisierung. Die Analyse und Modellierung von regenerativen Oszillatorschaltungen wird vorgestellt und verwendet, um das Verständnis der Schaltungen zu verbessern und Optimierungsziele des Entwurfs zu erreichen. Integrierte Schaltungen werden als Proof-of-Concept für ein drahtloses Kommunikationssystem mit hoher Datenrate, das zwischen 140–220 GHz arbeitet, und ein Fahrzeugradarsystem, das bei 60 GHz arbeitet, entworfen und charakterisiert. Amplituden- und Phasenregenerationsfähigkeiten für komplexe Modulationen werden untersucht und Prinzipien für die Charakterisierung von Spektren abgeleitet. Die Schaltungen werden in einer 130 nm SiGe-HBT-Technologie entworfen und hergestellt, die bipolare und komplementäre Metalloxid-Halbleiter-Transistoren (BiCMOS) kombiniert.

Um die Machbarkeit zu prüfen wird eine drahtlose Kommunikationsverbindung mit 16 Gbit/s über 20 cm Entfernung mit Quadraturamplitudenmodulation (QAM) realisiert. Es handelt sich um die höchste Datenrate, die jemals in superregenerativen Schaltungen erreicht wurde, und stellt dabei einen Weltrekord dar. Erreicht wird dieses Ergebnis mit einer superregenerativen Oszillatorschaltung, die bei 180 GHz arbeitet und eine Verstärkung von 58 dB liefert. Auch die DC Leistungsaufnahme ist mit 8,8 mW besonders gering, was einem Energieverbrauch von 0,6 pJ/Bit entspricht. Für die Systemversuche werden Gehäuse- und Modulintegrationsinnovationen implementiert, und es werden zusätzliche Breitbandschaltkreise untersucht, um anwendungsspezifische Schaltsignale zu erzeugen, um die Datenrate weiter zu verbessern. Für aktive Radarreflektoren wird eine regenerative Verstärkung von 80 dB bei 60 GHz mit einer einzelnen Schaltung nachgewiesen. Dies stellt zusammen mit der geringen Leistungsaufnahme von 25 mW einen Rekord für diesen Frequenzbereich dar.

Contents

1 Introduction

1.1 Super-Regenerative Receivers: A Motivation

1.1.1 For Wireless Communication

A significant driver of human civilization has always been the continuous improvement of communication media. Humans came up with many creative inventions over the centuries to relay a message as robustly and effectively as possible. With the invention of telegraphy in the 19th century, most human communication was transformed to an electrical nature, and the age of telecommunication systems had begun. The pursuit to advance both the speed and distance of communication channels has never stopped since. Many thousands of kilometers of cables were extended to expand the telegraph network, and the same approach was later used to connect human beings with the wired telephone network. Wired communication was costly and immobile, only limited to previously constructed point-to-point communication terminals. So already before the end of the 19th century, the first successful attempts at wireless communication had been demonstrated, and later experiments focused on expanding their distance as well as speed. That was the beginning of the age of radio.

In the beginning of the 20th century, minds were focused on inventing the best radio receiver architectures, in terms of robustness and performance, but also very importantly, cost. At the time, the three-terminal gain elements of choice were vacuum tubes or triodes, which were bulky, expensive, and prone to overheating and breakdown. It was around that time that the super-heterodyne receiver was invented with its superior selectivity and practicality, due to the use of a fixed intermediate frequency (IF) signal that allowed for easy filtering and detection. However, the relative complexity of the super-heterodyne receiver required a large number of devices, making the cost and size prohibitive to large scale use at that time.

The regenerative receiver offered many advantages to overcome these problems, and was incidentally invented and championed by the same electrical engineer who invented the super-heterodyne receiver [1]. An illustration of the regenerative receiver concept is shown in Figure 1.1. The design of the regenerative receiver carefully coupled back power from the output of the circuit and added it constructively to the input, resulting in instability and oscillation.

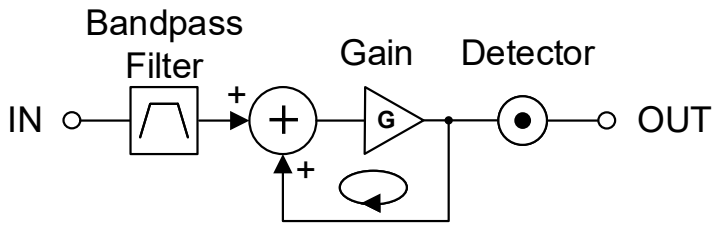

Figure 1.1: First order illustration of a regenerative receiver (Based on [1]. *Reprinted/adapted by permission from Springer Nature* ©2007 Springer)

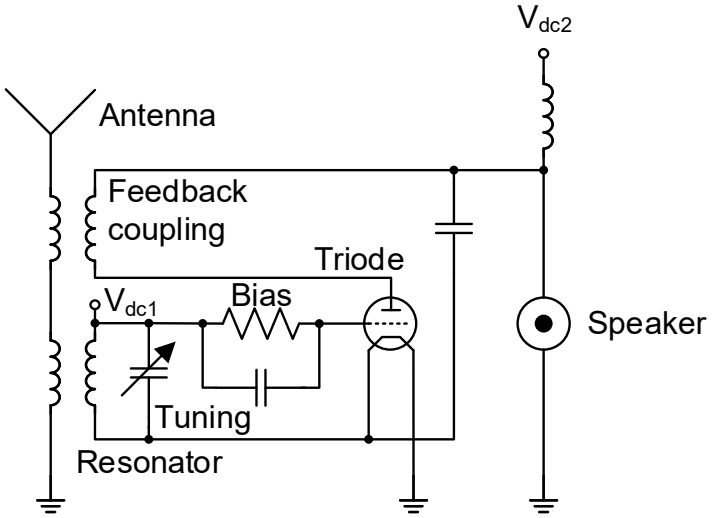

Figure 1.2: Simplified schematic of a regenerative receiver (Based on [1]. *Reprinted/adapted by permission from Springer Nature* ©2007 Springer)

However, a large increase in gain and sensitivity was consequently made possible by this positive feedback approach, which allowed to drastically decrease the number of required triodes. Figure 1.2 shows the circuit schematic of a regenerative receiver employing a single triode. Later, the circuit was modified to include an additional quench oscillator, leading to the invention of the super-regenerative receiver. The function of the quench oscillator was to periodically shut down the circuit and prevent it from getting saturated in a low sensitivity state. Thus, even higher gain and better performance and control were made possible, and wireless receivers could finally become simple to design, low cost and power efficient. The super-regenerative receiver opened the door for the first time to wide adoption of consumer products with a built-in wireless radio.

After the invention of transistors made of semiconductor materials, as well as the advances in lithography and fabrication techniques, devices became small and ubiquitous leading to a great reduction in cost. It was then that higher circuit complexity became feasible and even desirable, as it was possible to fully reap the advantages of the super-heterodyne receiver. Simplified detection and processing at low IF, as well as superior frequency selectivity that offered immunity to interference from neighboring bands were among the factors that led to the dominance of super-heterodyne receivers in wireless systems. The importance of the super-regenerative receiver largely faded, being pushed into a small number of low cost, low power and low data rate applications.

In today's world, we face many scenarios with circuit design problems that are fundamentally similar to the early days of radio. Despite having powerful transistor technologies with high dc gain, we may find ourselves forced to operate these transistors at high operating frequencies, where the gain of the transistors could be severely degraded but good receiver performance would still be required. Some examples could be found in mainstream civilian consumer applications such as wireless cellular communication. While the world is currently expanding its 5G capabilities, discussions are already ongoing over the plans and requirements of future 6G networks [2]. One of the main requirements is ever higher data throughput up to 100 Gbit/s, and since these need a large bandwidth in order to be realized at a practical

Frequency Band (GHz)	Contiguous Bandwidth (GHz)
116–123	7
174.8–182	7.2
185–190	5
244–246	2
Total	**21.2**

Table 1.1: Unlicensed spectrum allocated by FCC above 100 GHz [3]

signal-to-noise ratio (SNR), more frequency bands in the millimeter-wave range are being proposed. The United States Federal Communications Commission (FCC) has already allowed the use of 21.2 GHz of unlicensed spectrum above 100 GHz, which are divided as shown in Table 1.1.

The link budget challenges that come with such an upwards move in frequency are three-fold: higher free-space propagation loss, higher atmospheric attenuation, and lower transistor gain. Consequently, more dc power has to be pumped into more receiver gain stages in order to compensate for the missing gain, and since these receivers are typically built into mobile battery-powered devices, they drain the battery in a much shorter time. Solutions that aim to tackle these problems by increasing the circuit complexity would result in higher component cost, which would not be acceptable in these consumer applications. The good news, however, is that this set of problems can be solved by adopting a familiar approach. When the gain elements in the system are inefficient, and using more of them becomes too expensive and power-hungry, it helps to simplify the system and rely on fewer gain elements. The super-regenerative receiver offers this possibility, and no scientific reason could be found to restrict its use to only low data rate applications. Despite this, no investigation had been done in the literature to utilize super-regenerative receivers in the millimeter-wave range for high data rate wireless communication. Therefore, this work attempts to investigate this novel approach to improve the throughput while also improving the power efficiency of wireless communication.

1.1.2 For Radar

Radar sensing is another branch of wireless systems that would benefit from a shift to higher millimeter-wave frequency. In order to improve the resolution and be able to detect smaller objects, a large bandwidth is needed since it is inversely proportional to the resolution [4]. The majority of automotive FMCW radars today are already operating in the dedicated millimeter-wave band at 77–81 GHz, and more applications could be covered by implementations in unlicensed frequency bands, such as indoor localization in tunnels and parking garages. The shift to millimeter-wave bands would result in the same power challenges as previously discussed in section 1.1.1, leading to a reduction in range or an increase in power consumption, and the subsequent high cost and short battery life. Here, too, the super-regenerative receiver could provide a neat solution.

There are generally two broad types of radar systems, depending on the number of transceiver stations: reflective radar and one-way radar. A conventional reflective radar relies on one transceiver station that can transmit and receive radar signals at the same time.

The signals get reflected off the passive targets and travel back to the station, which could calculate the distance to the targets from the time it took the transmitted signal to return. The main advantage of reflective radars is the simple hardware implementation, since only one transceiver is needed, but there are various disadvantages. The maximum range is limited to around half of that of a one-way radar, since the signal has to travel twice the distance to the target. High isolation has to be guaranteed between the transmit and receive antennas to avoid saturating the receivers, and there is no easy way to distinguish between different targets, since they are passive, except by their reflected powers. On the other hand, a one-way radar is a radar that consists of several transceiver stations, each typically employing some amount of signal processing in each station, and with the transmitter and receiver operating in different time slots. Since each target is also a transceiver station, the range is significantly increased, and it is possible to distinguish between different targets. However, requiring a full transceiver station for each target does increase the complexity, cost, and power consumption of the whole system, apart from the difficult synchronization challenges between the base station and the targets.

Super-regenerative circuits could offer the necessary functionality to overcome the difficulties of both approaches. They could function as active reflectors to expand the detection range, while saving energy, reducing size, and saving cost. Since they contain active hardware, they could also implement techniques to allow target identification, and they would not require highly accurate synchronization. These advantages could be made possible by utilizing the phase regeneration capabilities of super-regenerative circuits to repeatedly sample, amplify and re-transmit an incident FMCW signal through sampling its phase, as has been explored in recent years [5]. The use of positive feedback and pulsed operation results in great improvements in energy efficiency, and the signal processing requirements in the active target are greatly reduced. This work aims to investigate these advantages by building super-regenerative active reflectors for civilian FMCW radars at higher millimeter-wave frequencies and better energy efficiency than previously reported. At the same time, the state of the art is advanced through design improvements of the gain and the bandwidth of active reflectors at these frequencies, in order to improve the range and the resolution of such systems, respectively.

1.2 Technology Overview: the IHP 130 nm SiGe BiCMOS Process

The circuits and systems presented in this thesis were designed and fabricated in the 130 nm SiGe BiCMOS technology SG13G2 by IHP GmbH. At the time of writing, it is one of the fastest silicon technologies in production, with HBTs that reach a peak f_T up to 300 GHz, and a peak f_{max} up to 500 GHz, with typical values around 450 GHz [6]. A high f_{max} is important for this work since it specifies the frequency at which the unilateral gain (U) of the transistor falls to 1, thus setting the absolute limit on oscillation frequency. In practice, however, oscillator designers normally target an oscillation frequency around one-fifth to one-third of f_{max} to guarantee oscillation against multiple factors, such as process, voltage and temperature (PVT) variations. Since super-regenerative systems mainly rely on a fundamental oscillator as the main component, and the oscillator loop gain is one of the main design parameters as will be discussed in later chapters, it becomes even more crucial to use fast transistors in order to allow more design flexibility. For the wireless communication systems

in this work, a center frequency of 180 GHz was targeted, which is a challenging 36% of the peak f_{max}.

The HBTs have a collector-emitter breakdown voltage BV_{CEO} of 1.6 V [6], and the sizing of the transistors is typically done by adding multiple emitters with minimum emitter area $A_{E,min}$ to the transistor layout in parallel. The process also offers bulk NMOS and PMOS devices with adjustable channel length and width down to 130 nm. Two gate oxide thicknesses are provided: a thin gate oxide for the 1.2 V process and a thick gate oxide for the 3.3 V process. These have different breakdown voltages, which were useful e.g. for building MOS decouple capacitors for different power domains. CMOS transistors were also used to implement various switch and control functions outside of the millimeter-wave receiver chain, such as the oscillator quench control circuit.

The process also offers useful passive components, such as thick gate oxide MOS varactors, precision and non-precision poly silicon resistors, and metal-insulator-metal (MIM) capacitors that are built into the back end of line (BEOL) of the technology. These are provided as custom pcells in the process development kit (PDK). The BEOL includes a metal stack consisting of five thin metals and two thick metal layers on top, which facilitate the design of low-loss high-Q inductors and transmission lines for RF and millimeter-wave frequencies. All of these features, as well as good device models, make this process a practical and reliable candidate for the design of high-performance RF and millimeter-wave system-on-chip (SoC) architectures.

1.3 Objective and Structure

The research work in this thesis was especially supported by the German Research Foundation (DFG) within the frame of the publicly funded research projects SPARS, MSPARS and 3D-LommID. The objective of this work is to perform fundamental scientific research into the topic of millimeter-wave super-regenerative receivers, and to investigate as a proof of concept the study of super-regenerative circuits and systems for two main applications.

- Wireless communication: Several features of super-regenerative circuits have remained largely unexplored in the literature, which would be very important for civilian wireless communication applications. Among these are the simultaneous use of phase and amplitude modulation to improve spectral efficiency, as well as maximizing the achievable data rates in such circuits. This work aims to investigate these novelties, while delivering superior energy efficiency in comparison to more conventional approaches, and maintaining low complexity and cost.

- Radar: Super-regenerative circuits can be useful to expand the range of civil automotive radar systems, while at the same time improving the energy efficiency and the battery life. One novel feature is high bandwidth in order to utilize super-regenerative active reflectors in high resolution radars. Thus, it would be necessary to study radars in unlicensed millimeter-wave bands where large bandwidth is available. This work aims to investigate millimeter-wave super-regenerative active reflectors for FMCW radar systems, while improving the gain and the energy efficiency against the current state of the art.

The thesis is structured in the following way. The current first chapter presents an introduction and motivation for this work, discussing the background and applications of super-regenerative receivers, and presenting an overview of the features of the semiconductor technology that was used for the fabrication of the circuits in this work. Following that, chapter 2 discusses the theory and operation of super-regenerative oscillators (SRO), which are the main components of super-regenerative systems. The amplitude sampling and phase sampling aspects of SROs, and the characterization of SROs in spectrum domain are examined using analytical equations. A simplified circuit model of the SRO is also derived and simulated using CAD tools in order to improve the understanding of SRO design goals.

Chapter 3 presents the design and characterization of millimeter-wave circuits for wireless communication in the range between 140–220 GHz. Three different design approaches to SRO circuits are presented, and the advantages and shortcomings of SRO1 and SRO2 are discussed, leading up to improved all-round performance in SRO3. A mixer design and improvements on it are also presented, as well as the design of an integrated passive balun. Ultimately, a system experiment is built and a wireless data transmission is carried out using 16-QAM signals, proving the phase and amplitude modulation capabilities of super-regenerative receivers, and leading to world record data rate results.

Chapter 4 examines the quench waveform requirements of high data rate SROs, and proposes the generation of high-speed rectangular signals to increase the data rate. Two broadband circuits are designed and characterized to address these requirements, one is based on limiting amplifiers and the other is based on RF Schmitt trigger approach. The latter circuit advances the state of the art significantly in terms of maximum speed and duty cycle tuning capability.

In chapter 5, the use of super-regenerative circuits is proposed for FMCW radar applications. A radar system concept for civil automotive parking localization is presented and its pros and cons are compared against a conventional one-way radar system. A receiver frontend circuit and a SRO active reflector circuit are designed and characterized, and the experimental results are discussed. The SRO circuit demonstrated a superior gain as well as energy efficiency performance compared to other circuits in its frequency range.

Chapter 6 presents the conclusion of this work and the outlook for future work. The ways in which this work has advanced the state of the art are summarized, and suggestions are provided for key aspects to be explored and improved in further work.

1.4 Previously Published Original Work

Within this document, previous original work that was published under the copyright of IEEE is reused in chapters 2 to 5 of this dissertation. No formal license is required by IEEE to reuse this copyrighted material in a thesis, according to the obtained IEEE permission grant. All reused material is properly referenced in accordance with the IEEE copyright policies. Any figures, tables, or excerpts of text that were taken directly from previously published documents with small or no modifications are marked with ©20XX IEEE for IEEE publication material. 20XX denotes the year of publication. A footnote at the beginning of each chapter clearly mentions which sections borrow material from the self-authored papers. To clearly distinguish them from other citations in the text, original publications where I am the lead author are specifically marked with [X]♠ in the text. Therefore, X represents the citation

index, as found in the bibliography. In addition, a list of these publications is included at the end of the dissertation, titled as ”List of Original Publications”.

2 Theory and Operation of Super-Regenerative Oscillators

2.1 The Super-Regenerative Oscillator

The SRO is the main component in a super-regenerative receiver, a small circuit that provides an ingenious solution to the problem of low device gain. At the very high sub-terahertz frequency, circuit designers often find their devices operating at the limit of their capabilities. For the case of mm-wave and sub-terahertz systems, one direct solution was attempted in research by cascading many of these devices (or transistors) in many stages to multiply their gains, and thus compensate for the gain limitations of single devices [10]. This inevitably increases the complexity and power consumption of a system, making these aspects in many cases prohibitive for use in battery-powered applications. Recently, alternative architectures based on the use of an SRO with phase and amplitude sampling capabilities and large regenerative gain have been proposed [11]–[13]. The circuit concept is presented in Figure 2.1.

The signal is fed to the oscillator core and the phase and amplitude information is sampled at the turn-on instant, when the oscillator is most sensitive. The oscillation then grows exponentially to its steady-state level with the phase information preserved. To receive the following symbols, the oscillator has to be periodically quenched, thus each oscillation pulse represents one symbol. Depending on the quenching time T_{on}, the SRO circuit can have two modes of operation [14]:

- linear mode, or
- logarithmic mode.

A depiction of these two modes is shown in Figure 2.2, produced by numerical simulations of a 180-GHz SRO model. If the SRO is quenched before a steady-state is reached, there is a linear dependence between the input and output amplitudes, and the oscillator is said to be in linear mode. This is suitable for applications in which amplitude modulation or on-off keying is used. In case the SRO amplitude is allowed to saturate, the amplitude information is

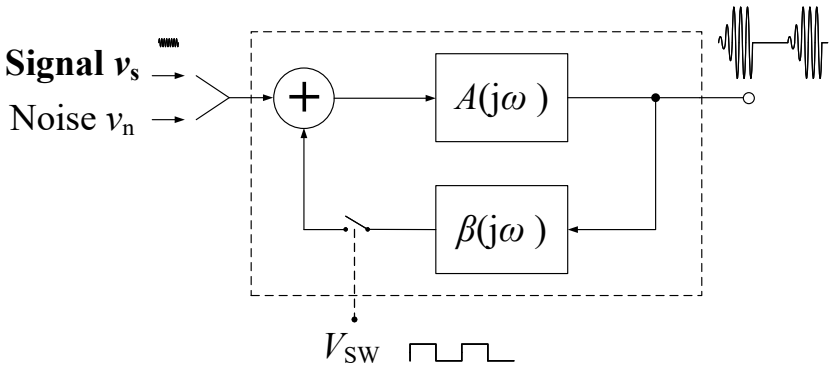

Figure 2.1: SRO operation principle based on positive feedback [7]♠ ©2020 IEEE

corrupted, and the SRO is in logarithmic mode. This mode is beneficial for phase modulation applications, as it leads to the highest regenerative gain. The possibility of simultaneous phase and amplitude modulation in linear-mode SROs allows for their use with more complex modulation schemes, such as QAM, which leads to better spectral efficiency.

Figure 2.2 also illustrates the possibility of amplitude modulation by varying the input amplitude of the SRO. The SRO output waveform and envelope are shown for the cases of low as well as high input amplitudes. The different input amplitudes result in different output amplitudes reached at the quench instant $T_{on,lin}$, in the case of linear mode. This was already a popular modulation method for very early SROs, due to the simple implementation of its transmitters and detectors [15]. In case of logarithmic mode operation, the output amplitude is largely independent of the input amplitude, as shown in the figure.

On the other hand, Figure 2.3 illustrates the possibility of SRO phase modulation based on the input phase. The input signal is set to have two different phases, namely 0° and -90°, and the output signal's phase is seen to follow. This has become popular in more recent SROs, partly due to its capability to regenerate FMCW chirp signals through repeated sampling and re-transmission of their phase information [16]. Phase modulation can be performed equally well in linear and logarithmic modes, by repeatedly sampling the phase of the input signal over a series of quench periods, thus discretely tracking the phase. However, logarithmic modes offers the advantage of higher regenerative gain (in case amplitude modulation is not simultaneously desired), as the SRO is allowed to reach its maximum steady-state output amplitude.

The advantages of this super-regenerative approach include low complexity, as well as high power and area efficiency, since one block can replace multiple gain stages in the receiver. Through pulsed operation by repeated quenching, the power consumption is further reduced. On the other hand, the high sensitivity of the super-regenerative circuit leads to susceptibility to interferers in adjacent channels. This limitation is, however, relieved by the large channel bandwidth in mm-wave bands, as well as the high propagation loss, which allows for frequency reuse after a short distance.

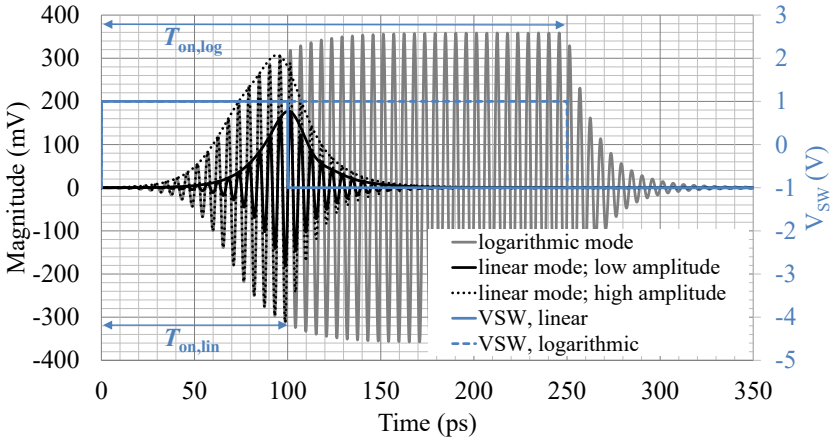

Figure 2.2: Numerical simulations for a 180-GHz SRO output at different amplitude modulation levels. The plot also shows the quench signal V_{SW} for the two distinct modes of operation: linear and logarithmic [7]♠ ©2020 IEEE

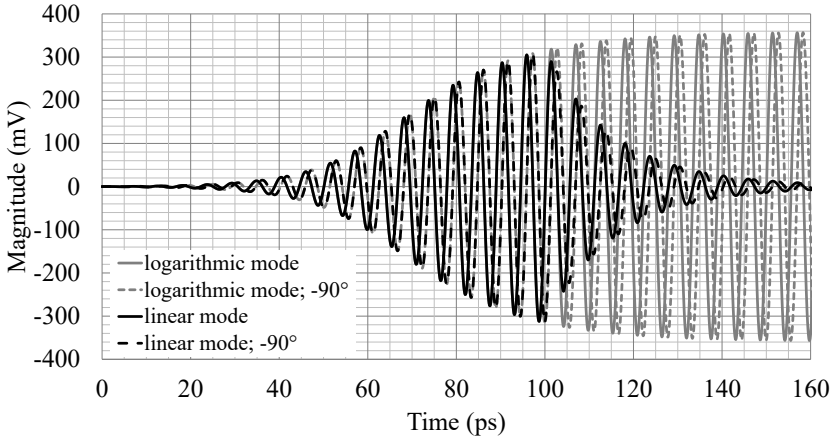

Figure 2.3: Numerical simulations for a 180-GHz SRO output at two different phase modulation values: 0° and -90°. The plot shows the SRO phase modulation in both linear and logarithmic modes of operation [7]♠ ©2020 IEEE

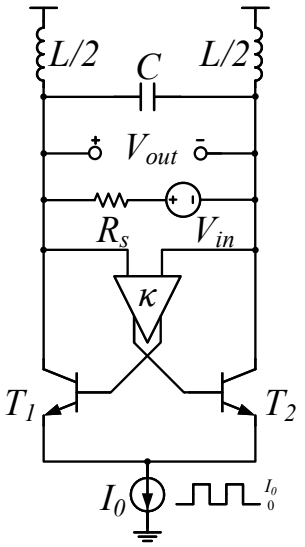

Figure 2.4: Cross-coupled SRO model [8]♠ ©2017 IEEE

2.2 Cross-Coupled SRO Analysis

To understand and explore the relationships between various SRO design parameters, an analysis of the SRO circuit was performed using the cross-coupled oscillator model. The results of this analysis are presented and discussed in this section, and the derivations of the equations are found in detail in [9]. The circuit schematic of the model is shown in Figure 2.4, and features an input voltage V_{in} and an output voltage V_{out}. The model includes a tail current source that is alternately drawing a current of I_0 in the ON state and zero in the OFF state. To simplify the mathematical analysis, the current switching waveform is assumed to have a rectangular shape.

2.2.1 Amplitude Analysis

For the cross-coupled SRO model in Figure 2.4, the system behavior in the ON state ($I_0 \neq 0$ A) is described by the equation [16]

$$\ddot{V}_{out} + \frac{1}{\tau}\left(1 - G_L + G_L \tanh^2\left(\frac{\kappa V_{out}}{2V_T}\right)\right)\dot{V}_{out} + \omega_0^2 V_{out} = \frac{1}{\tau}\dot{V}_{in}. \tag{2.1}$$

The time constant τ is defined as

$$\tau = R_s \cdot C. \tag{2.2}$$

The natural resonance frequency ω_0 is defined as

Acknowledgment: *This is to acknowledge that section 2.2 contains the results of a joint work on SRO theory and analysis, for which my colleague at Technische Universität Dresden, Ali Ferschischi, was the lead author. He was also the first author of [9], in which this work was first published, and where more details on the derivation and verification of the analysis can be found. I would like to express my gratitude for his contributions and for his permission to report on this work in my thesis.*

$$\omega_0 = \frac{1}{\sqrt{LC}}. \tag{2.3}$$

The loop gain G_L is described by the equation

$$G_L = \frac{\kappa I_0 R_s}{4V_T}, \tag{2.4}$$

where κ is the cross-coupling feedback factor and V_T is the thermal voltage. Lastly, the input voltage V_{in} is defined as follows

$$V_{in}(t) = A_{in} \cdot \sin(\omega_{in} t + \phi_{in}), \tag{2.5}$$

where A_{in} is the amplitude, ω_{in} is the angular frequency, and ϕ_{in} is the phase of the input signal. Equation 2.1 is a second-order differential equation, for which a single solution is difficult or unlikely to be found [17]. Therefore, a different approach was followed to solve for the output voltage envelope $V_{ENV}(t)$, assuming that

$$V_{out}(t) = V_{ENV}(t) \cdot \sin(\omega_0 t + \phi_{out}). \tag{2.6}$$

For simplicity, it was assumed that $\omega_{in} = \omega_0$, and two solutions were found, depending on the magnitude of $V_{ENV}(t)$.

For **small magnitudes**, i.e. $V_{ENV}(t) \leq 2V_T/\kappa$

$$V_{ENV}(t) = \frac{A_{in}\cos(\phi_{in} - \phi_{out})}{G_L - 1}\left(-1 + \exp\left(\frac{(G_L-1)t}{2\tau}\right)\right) + V_0 \exp\left(\frac{(G_L-1)t}{2\tau}\right), \tag{2.7}$$

where $V_0 = V_{ENV}(0)$ is the value of the envelope function at the turn-on time, i.e. at $t = 0$. Note that the last term can be removed if the previous oscillation is allowed to dissipate to a negligible value, i.e. $V_0 \approx 0$.

From Equation 2.7, the time t_d can be defined and calculated as the start-up delay time of the oscillation, which is approximately the time when the envelope for small magnitudes reaches the value $V_{ENV}(t_d) = 2V_T/\kappa$. Thus, Equation 2.7 is only considered valid for $t \leq t_d$. After some simplification, t_d is found to be

$$t_d \approx \frac{2\tau}{G_L - 1} \ln\left(1 + \frac{2V_T}{\kappa}\frac{G_L - 1}{A_{in}}\right). \tag{2.8}$$

In fact, Equation 2.8 describes the basis for amplitude modulation in the SRO circuit, due to the dependence of t_d on A_{in}. Other important design parameters influencing this amplitude modulation behavior include the loop gain G_L and the time constant τ. For example, in order to have fast quenching and high symbol rate in the system, small values of t_d would be needed, thus the design goals of the SRO might include a small time constant τ and a large loop gain G_L.

For **large magnitudes**, i.e. $V_{ENV}(t) > 2V_T/\kappa$ or $t > t_d$

$$V_{ENV}(t) \approx \frac{2I_0 R_s}{\pi}\left(1 - \exp\left(-\frac{t - t_d}{2\tau}\right)\right), \tag{2.9}$$

where the magnitude contribution of A_{in} has been assumed to be negligibly small compared to I_0R_s. However, A_{in} still has a large influence on the output magnitude through t_d, as can be seen in Equation 2.9. Modulation of the input amplitude results in a modulation of the start-up delay time, thus resulting in a modulation of the output amplitude, for a fixed sampling instant of time. Thus, this equation can help the designer to choose important signal processing and system design parameters, such as the sampling instant and the symbol rate. Another important design parameter is the steady-state output power $P_{out,max}$, which can also be calculated from Equation 2.9, with an output load resistance of R_L, as

$$P_{out,max} = \frac{1}{2R_L}\left(\frac{2I_0R_s}{\pi}\right)^2. \tag{2.10}$$

$P_{out,max}$ is a very important parameter, since it directly contributes to the maximum SRO regenerative gain $G_{SRO,max}$, defined as the difference between $P_{out,max}$ and the input sensitivity $P_{inj,min}$ (see Equation 3.2). The parameter $P_{out,max}$ also has implications for the design of the subsequent stages. For example, a large $P_{out,max}$ would relax the baseband gain requirements, but might place additional challenges on the input linearity of the mixer.

2.2.2 Phase Analysis

In the case of using the SRO for regenerating phase information or modulation, it becomes important to investigate the dependence of the output phase on the input phase, and how this dependence is influenced by circuit design choices. By understanding these relations, the circuit designer is enabled to improve the phase coherence between the input and output, thus improving the sensitivity of the receiver and the regenerative gain. For more details on the derivations of these relations, the reader is referred to [9]. Starting with Equation 2.6, it can be shown that

$$\dot{\phi}_{out}(t) = -\frac{1}{\omega_0}\frac{1}{\dot{V}_{ENV}(t)} \cdot \sin(\omega_0 t + \phi_{out}(t)) \cdot f(t). \tag{2.11}$$

Solving this for $V_{out}(t)$ in terms of $V_{in}(t)$, the following approximate relation was derived

$$\cot(\phi_{out}) \approx \cot(\phi_{in}) - \frac{1}{\omega_0}\frac{G_L}{2\tau}. \tag{2.12}$$

This equation shows that the phase coherence degrades with increasing loop gain G_L and with decreasing time constant τ, which means that slow start-up leads to better accuracy for phase modulation of the SRO. This can be understood intuitively in the following way: as more time is allowed in the small magnitude domain (i.e. $V_{ENV}(t) \leq 2V_T/\kappa$) when the SRO phase sensitivity is high, this gives more time for the incoming input signal to influence the start-up phase, which improves the phase coherence of the SRO output signal [5]. Conversely, with fast start-up, the SRO shoots past this sensitive domain and only a short time is allowed for good phase sampling. Additionally, this can also be influenced externally through the shape of the quench signal, as has been previously shown by other researchers, such as by introducing an integrating capacitor [18], or by quench waveform shaping [19]. In these cases, artificial external control of the SRO start-up has led in a similar way to better phase sensitivity. These techniques would be tolerated in radar applications where the quench rate is relatively

low. However, for wireless communication purposes with high data rate requirements, fast SRO start-up would be desired, even at the cost of phase sensitivity. A careful design trade-off of these considerations would thus be needed.

It is notable that Equation 2.12 predicts no effect for A_{in} on the relation between the input and output initial phases. However, it must also be noted that the analysis, for simplification reasons, did not take noise into consideration. Thus, an important factor influencing the phase sampling accuracy was missing from these results. In [16], an analysis of noise in SRO phase sampling was performed, and found that below a certain A_{in} that is related to the noise power, the phase sampling errors start to increase, thus degrading the SRO sensitivity. This highlights the importance of a good SNR at the SRO input, and defines the minimum input power $P_{inj,min}$ that a phase sampling SRO can coherently regenerate.

2.2.3 Spectrum Analysis

The characterization of microwave and millimeter-wave circuits is typically done in frequency domain, since time-domain measurements are in most cases difficult, or they provide an incomplete picture of the circuit performance. In order to assist and quantify the millimeter-wave SRO characterization, the frequency-domain behavior of the circuit was analyzed. For this purpose, only the large magnitude part of the output envelope was taken into account, and rectangular switching with fast oscillation start-up was assumed. The input signal of the SRO that is present in the ON state is considered to be

$$V_{in}(t) = A_{in}\sin(\omega_{in}t). \tag{2.13}$$

It was also beneficial to assume the initial phase of the input signal to be zero, as it would simplify the mathematical derivation. If the phase of the output signal was equal to the phase of the input (i.e. for ideal phase sampling), the Fourier transform of the SRO pulse train would yield a positive SRO spectrum ($f \geq 0$) that is described by

$$|V_{out}(f)| = \underbrace{\frac{2I_0R_s}{\pi}}_{\text{max. amplitude}} \cdot \overbrace{\frac{T_{on}}{T_{sw}}}^{\text{duty cycle}} \cdot \underbrace{\left|\operatorname{sinc}(\pi T_{on}(f-f_{osc}))\right|}_{\text{sinc envelope}} \cdot \overbrace{\sum_{n=-\infty}^{+\infty}\delta((f-f_{inj})-nf_{sw})}^{\text{Dirac comb}}. \tag{2.14}$$

The complete derivation is found in [9]. Equation 2.14 shows that, in case of perfect phase coherence, the SRO output spectrum is composed of a superposition of two components:

1. a **sinc-shaped envelope** that is scaled by the maximum steady-state amplitude and the duty cycle, and centered around the oscillation frequency of the SRO (not the input frequency), and

2. a **Dirac comb train of impulses** at the input frequency and frequency offsets that are multiples of the quench rate in both directions.

If the above conditions are fulfilled in the SRO output spectrum, it can be concluded that the SRO is operating as a regenerative amplifier with good phase coherence. This is very useful

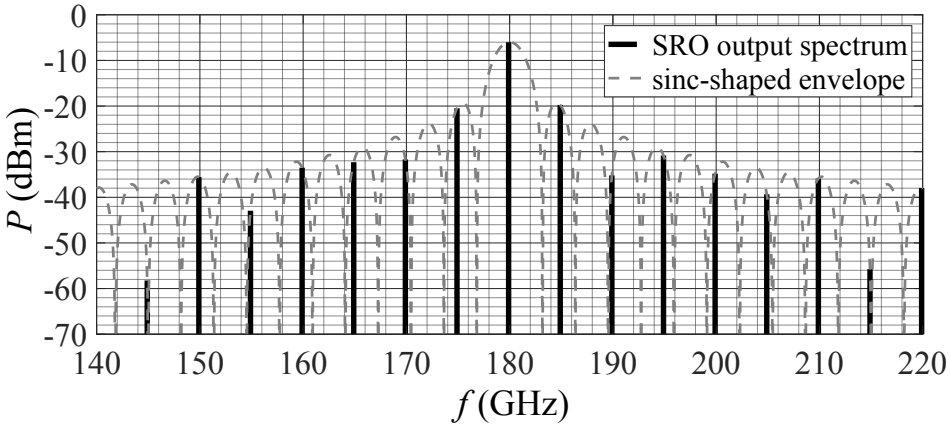

Figure 2.5: SRO power spectrum and envelope based on numerical calculations of Equation 2.14. Max. amplitude = 317 mV (0 dBm at 50 Ω), duty cycle = 50%, f_{osc} = 180 GHz, f_{inj} = 179.9 GHz, and f_{sw} = 5 GHz.

for SRO characterization, since it would otherwise be very difficult to verify phase coherence between input and output signals in time domain. For millimeter-wave SROs, it becomes even more crucial to characterize the spectrum in frequency domain, as the frequency of operation is often beyond the time-domain sampling capabilities of available lab instrumentation. On the other hand, spectrum analyzers in combination with mixer modules can readily cover a large range of frequencies.

Figure 2.5 shows an example for visualization of an SRO spectrum, based on numerical calculations of Equation 2.14. Typical values were chosen for a 180 GHz SRO with a fast quench rate of 5 GHz e.g. for use in wireless communication. The sinc-shaped envelope was also plotted and clearly shows the superposition of the sinc function, centered around f_{osc}, and the Dirac comb that is ruled by f_{inj} and f_{sw}.

2.3 The Switched Injection-Locked Oscillator

A moderately recent publication claimed a novel circuit with the name of Switched Injection-Locked Oscillator (SILO) [20], which was promoted for use as active reflector to extend the range of FMCW radar systems. While the paper reignited the interest in super-regenerative circuits and opened the door for new applications, the choice of a new name for the circuit was unfortunate for several reasons. The name SILO decoupled this type of circuit from the wider research domain of super-regenerative circuits. A few circuits of that type have been published under the name SILO in the years following the publication, which presented their work as a new invention and cited only other SILOs (and the same approach was initially followed by the author of this dissertation). In fact, the operation concepts of the circuit are identical to those of a phase-sampling SRO, which have been explained in the previous few sections.

Another considerable aspect is that the name SILO is factually misleading, due to the use of the adjective ‘injection-locked’ in the name. The SILO, or SRO, circuit does not exhibit any frequency injection-locking as in the case of injection-locked oscillators, since the input power is typically too low to pull or lock the oscillator frequency. The SRO spectrum merely

appears locked to the input frequency due to the spectral lines seen at $f_{inj} \pm n f_{sw}$, as predicted by Equation 2.14. However, the same equation also shows that the sinc-shaped envelope is centered around the actual oscillation frequency of the SRO f_{osc}. In actuality, what happens is that the SRO pulses periodically sample the phase of the input signal in a discrete manner. Thus, they appear in the spectrum to be regenerating the frequency of that input signal. This is a result of sampling theory, and is indeed the property of SROs that is very useful in FMCW active reflectors. Therefore, to avoid confusion and strengthen collaboration in the research community, the term SRO is uniformly used in this thesis to refer to super-regenerative circuits with amplitude and/or phase sampling capabilities. Circuits that have previously been published under the name SILO have also been cited and included under the general category of SROs.

2.4 SRO Modeling using CAD and Verilog Models

Super-regenerative oscillators are the main building blocks of any regenerative system, and combine the functionalities of signal synthesis and amplification. They have to be quenched in every symbol period to dissipate the energy from the previous symbol and return to the off-state before receiving the next symbol, in order to prevent inter-symbol interference. Thus, the start-up stage of the oscillator presents the most sensitive and most critical part of its operation, and needs to be carefully studied to set design goals.

Due to the nonlinearity of the gain device, in this case a bipolar transistor, it is not possible to obtain a general closed-form analytical solution for this problem. Therefore, the use of nonlinear modeling and numerical analysis tools becomes the next best option to study the circuit [21]. In this work, as opposed to [22], an electrical design tool is preferred over mathematical tools for several reasons, such as the readily available implementations of basic circuit components, the availability of various simulation modes for many circuit analysis scenarios, as well as the ease of comparison with transistor-level simulations. The model is derived from the circuit parameters and the large-signal behavior of the devices, and can be used to predict design features that cannot be directly measured at high frequency [8]♠.

SRO Circuit Description

The circuit schematic in Figure 2.6 contains all the necessary elements for building a super-regenerative oscillator. It is based on a common-emitter cross-coupled oscillator topology, which uses two bipolar transistors, T_1 and T_2, interconnected in a positive-feedback loop to satisfy both the amplitude and phase conditions for oscillation. The feedback contains a coupling factor κ, which can be set by the designer up to a value of one, if implemented e.g. as a capacitive divider. The circuit has an injection input V_{in} for the modulated information signal. A second input V_{sw} is used to quench the tail current source of the circuit periodically, thus switching off the gain and allowing the oscillation to dissipate in the passive network.

Acknowledgment: *This is to acknowledge that section 2.4 contains the results of a joint work on SRO modeling, for which my colleague at Technische Universität Dresden, Mohammed El-Shennawy, was a major contributor. He was also a co-author of [8]♠, in which this work was first published. I would like to express my gratitude for his contributions.*

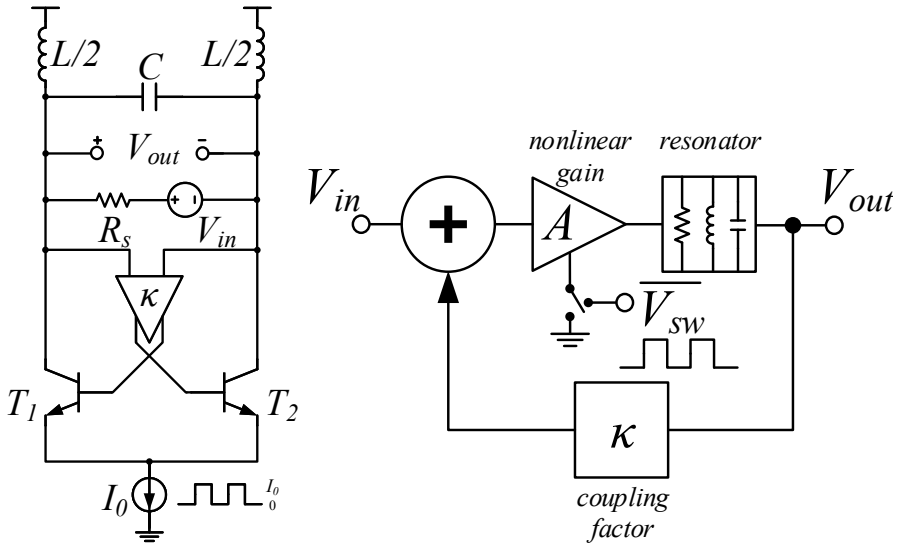

Figure 2.6: Schematic of a cross-coupled SRO circuit (left), and block diagram of the positive feedback model (right) [8]♠ ©2017 IEEE

Figure 2.6 also shows a representative block diagram of the circuit with all components in a feedback loop.

Device-Level Model

A nonlinear model of the circuit was studied based on the BJT large signal model in a one-to-one fashion. Each of the transistors T_1 and T_2 was replaced by a voltage-controlled current source that models its nonlinear large-signal behavior. The source was implemented in Verilog to represent the collector current I_C according to the equation

$$I_C = I_S \exp\left(\frac{\kappa V_{be}}{V_T}\right) \tag{2.15}$$

and included as a circuit symbol as shown in Figure 2.7. Thus, κ was implemented as a variable quantity in the equation to be set with more flexibility. The base currents have been neglected, assuming high current gain.

Simplified Model

For purely differential signals without operating point and common-mode considerations, the equivalent circuit in Figure 2.8 was derived, since the common-mode signals are suppressed by the ideal current source. The differential current in the cross-coupled pair I_{diff} is described as

$$I_{diff} = I_0 \tanh\left(\frac{\kappa V_{be}}{2V_T}\right). \tag{2.16}$$

Thus, the two exponential gain elements were replaced by one hyperbolic-tangent element. Both I_S and the supply voltage V_{CC} fall out of consideration, simplifying the calculations. The

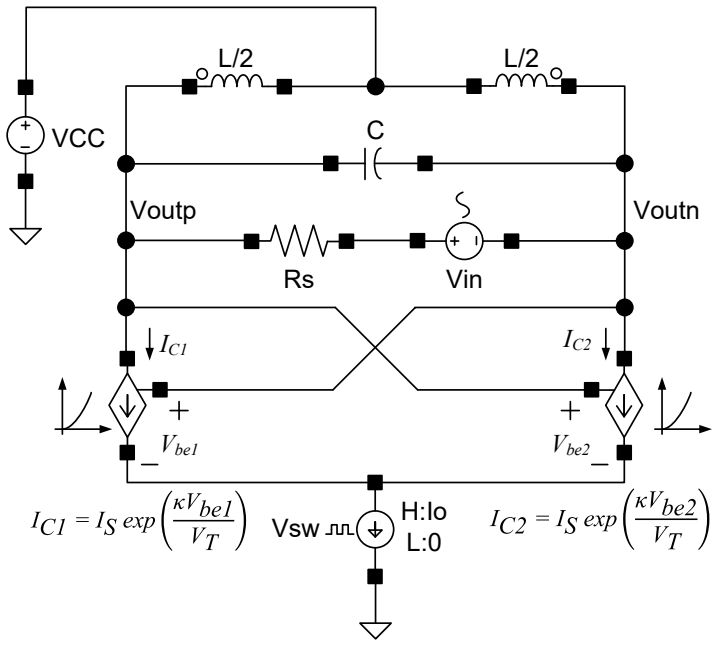

Figure 2.7: Device-level model of the cross-coupled circuit with transistors replaced by their nonlinear large-signal model (CAD labels are in Arial font, whereas the underlying model equations are in Times New Roman) [8]♠ ©2017 IEEE

current is loaded by the parallel connection of $L/2$, $2C$, and $R_S/2$. V_{in} is assumed small enough to be neglected compared to the oscillation amplitude. Therefore, Figure 2.7 and Figure 2.8 are equivalent regarding differential signals. Note that the oscillation frequency f_{osc} remains unchanged at

$$f_{osc} = \frac{1}{2\pi\sqrt{LC}}. \tag{2.17}$$

Simulation Results

The simulation results of the SRO models are presented in this section. To verify the equivalence of the two models, a transient analysis was run for each model with the same parameters to compare the startup behavior of the two modeling approaches. The capacitance and inductance values were chosen for an oscillation frequency of f_{osc} = 145 GHz. Avoiding the need for setting the dc operating point or the process-dependent saturation current, as required in the first approach, makes the second approach more generic and adaptable to more application scenarios. With reference to Figure 2.7, the output voltage V_{out} is defined for the differential model as

$$V_{out} = V_{outp} - V_{outn}. \tag{2.18}$$

The time-domain simulation results are shown in Figure 2.9, and an excellent agreement of the waveforms can be observed during startup. The oscillation frequency, the startup phase, the settling time, and the steady-state amplitude all align well. In [9], it was also shown that these numerically simulated results produce an excellent fit with V_{ENV}, as predicted by

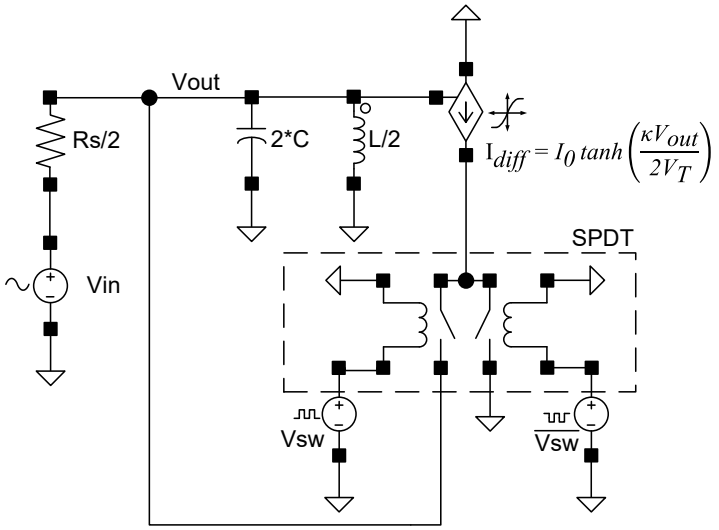

Figure 2.8: Simplified model of the cross-coupled oscillator based on the analysis of differential currents, SPDT stands for a single-pole double-throw switch (CAD labels are in Arial font, whereas the underlying model equation is in Times New Roman) [8]♠ ©2017 IEEE

equations 2.7 and 2.9 in section 2.2.

In addition to the time-domain response, the stability analysis was performed to determine the loop gain and phase as a function of frequency, and the results are also shown in Figure 2.10. Once again, the models perform in an identical manner over various frequencies. An important requirement when performing the stability analysis for a differential circuit, as in the first model, is to use the differential stability probe "diffstbprobe" from the *"analogLib"* library rather than a single-ended probe, so as not to introduce imbalance in the circuit that would alter the operating point and produce wrong results. That is also true for the cross-coupled oscillator in transistor-level simulations.

The loop gain is seen to reach a maximum at the resonance frequency of 145.3 GHz, which follows from the values used for L and C. The loop phase reaches a value of 0° at that frequency, marked by the dashed vertical marker. The loop gain maximum value of 8.65 follows from the system's closed-loop gain G_L that is calculated as

$$G_L = \frac{\kappa I_0 R_S}{4V_T}. \tag{2.19}$$

This expression and the simulation results confirm the equivalence of the models. The results fulfill both the amplitude and the phase conditions for oscillation, and the circuit starts to oscillate upon the introduction of an external signal. In the absence of any noise sources in the model, the oscillation is started by the input V_{in}.

In the next part, the effect of the amplitude and phase of the injection signal V_{in} on the oscillation output is investigated. For that purpose, the coupling factor κ is lowered to 0.35, bringing down the overall closed-loop gain to 3. This presents a more realistic target for mm-wave oscillators, in which the gain might not be exceedingly high. Since the models have so far been shown to be equivalent, only results from the simplified model are presented in the following.

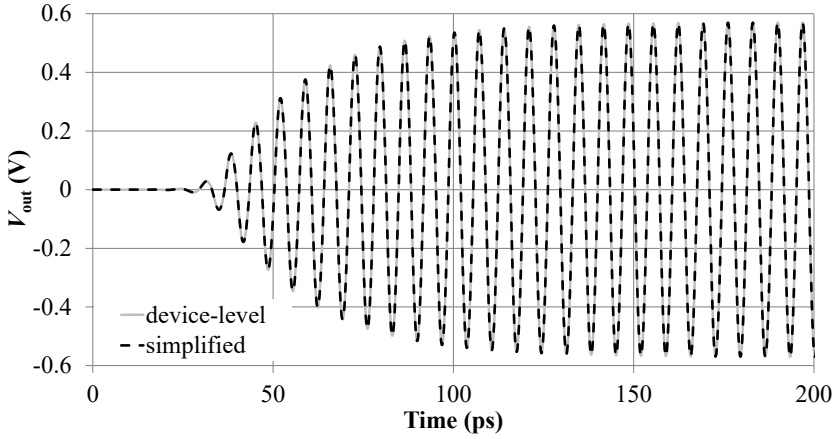

Figure 2.9: Simulated transient response for both models with the same element values. $V_{out} = (V_{outp} – V_{outn})$ for the differential device-level model [8]♠ ©2017 IEEE

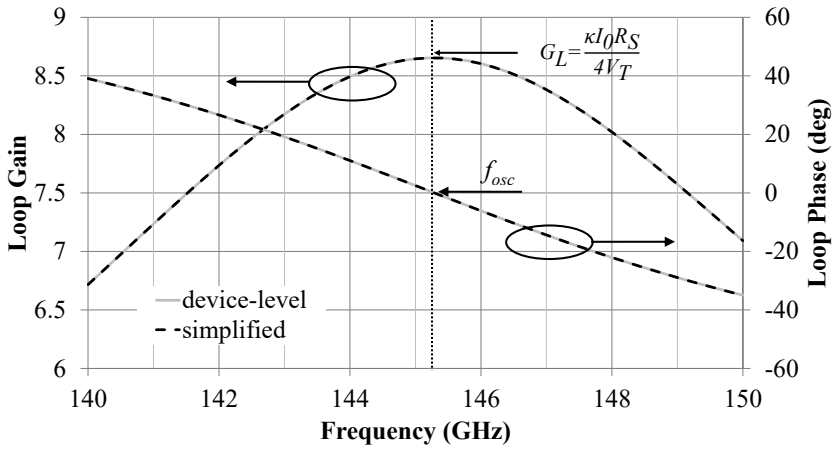

Figure 2.10: Simulated loop gain and phase for both models given by stability analysis. The same element values as for the transient simulations were used [8]♠ ©2017 IEEE

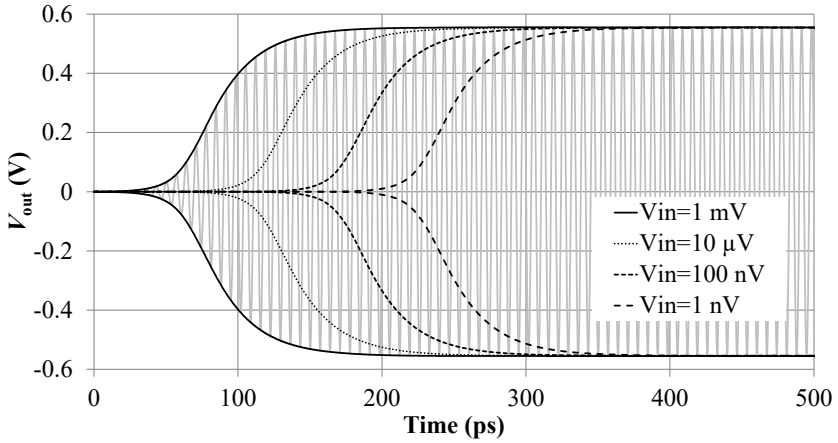

Figure 2.11: Simulated startup envelopes for different V_{in} amplitudes at $\kappa = 0.35$ using the simplified model [8]♠ ©2017 IEEE

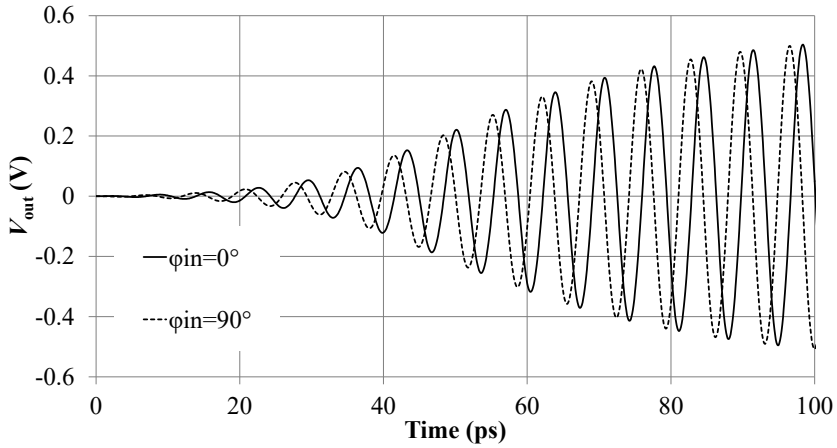

Figure 2.12: Simulated startup waveforms for input signal phases 0° and 90° using the simplified model at V_{in} amplitude = 10 mV [8]♠ ©2017 IEEE

The input amplitude is swept and the envelope of the output V_{out} at each amplitude value is shown in Figure 2.11. The peak envelopes were calculated from the signal waveforms using MATLAB. It is apparent that the onset of oscillation occurs faster for higher input amplitudes. If the oscillator gain is quenched after 500 ps, then the energy in this pulse is indirectly modulated by input amplitudes that can be very small. Thus, for periodic switching and varying input amplitude from one symbol to the next, this is equivalent to amplitude modulation at a rate of 1 GHz (assuming 50% duty cycle). Noteworthy is also the huge gain potential for very small input amplitudes (≈100 dB for 1 μV). In reality, this is limited by the noise floor at the frequency of operation, such that the input amplitude must be higher than the noise level.

Another promising aspect of the super-regenerative oscillator that can be studied with the help of this model is the phase coherence between the input and output. Figure 2.12 shows the output waveforms for two different initial input phases during startup. It can be seen that varying the input phase by 90° causes the output signal phase to follow by the same phase difference. The same effect can be similarly shown for any desired phase difference. The input phase is sampled at the onset of oscillation and the output builds up with the same phase for the rest of the symbol duration. This presents excellent potential for phase modulation by varying the input phase at the start of every symbol period and demodulating the phase at the middle or the end of the pulse. The phase can also be influenced by very small input signals but the output is boosted to high levels, relaxing the baseband requirements on signal levels e.g. lower VGA gain is tolerated. However, the input signal again needs to have a sufficiently high signal-to-noise ratio. Below a certain level, the noise governs the oscillator's startup phase and no phase modulation is possible.

Experimental Results

The measurements of a realized SRO are used to validate the model. The circuit was fabricated in a 130 nm SiGe HBT technology and oscillates at a frequency of 145 GHz [23]♠. The oscillator's waveforms cannot be directly observed in time domain, since the oscillation frequency is too high for even the fastest state-of-the-art oscilloscopes. Therefore, the circuit was switched at a relatively low rate of 10 MHz, and the mm-wave output was down-converted

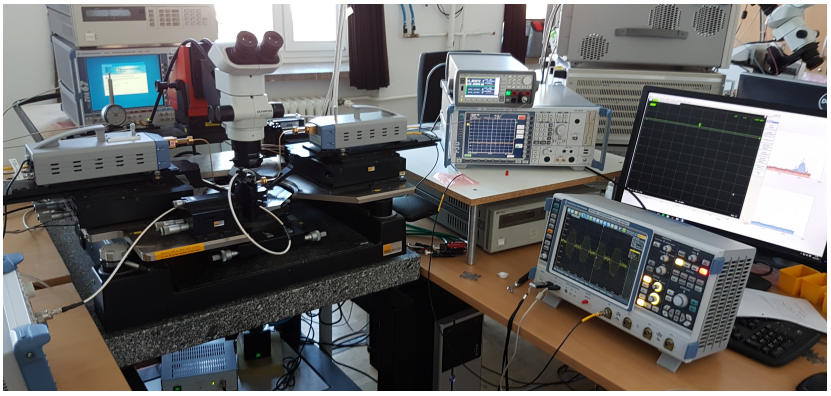

Figure 2.13: Measurement setup for 145-GHz super-regenerative oscillator [8]♠ ©2017 IEEE

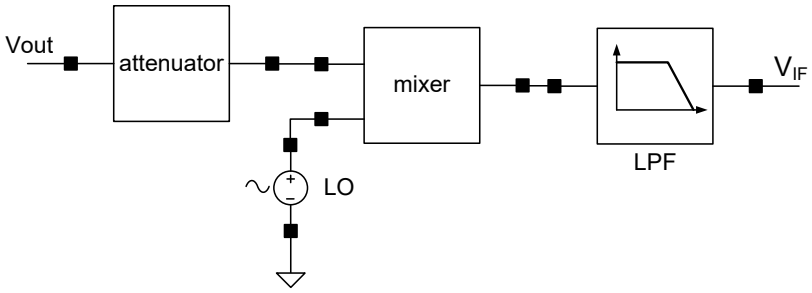

Figure 2.14: Down-conversion model consisting of attenuator, mixer, LO generation and lowpass filter [8]♠ ©2017 IEEE

to an IF of 279 MHz using frequency converter modules for network analysis, with a limited bandwidth of 500 MHz. The output was measured using a real-time oscilloscope. The setup photo is shown in Figure 2.13.

To reproduce the same waveforms, the model in the previous section is extended with the blocks shown in Figure 2.14. An attenuator is inserted to model the losses in the converter module, the waveguide, and the probe. The LO source at 145 GHz and the mixer together down-convert the high-frequency oscillations to IF. The lowpass filter models the converter module bandwidth-limiting filter. The "attenuator" and "mixer" cells are used from the *"ahdlLib"* library, while the LPF is implemented as an RLC filter as shown in Figure 2.15. The design values are included, and the simulated frequency response shows a 3-dB bandwidth of 560 MHz.

Figure 2.16 shows the comparison between down-converted 10 MHz pulses from model simulations and measurements. The pulses align very well in frequency of oscillation and switching, but the measured pulses seem to be suffering from frequency-dependent losses of the modulated spectrum during the down-conversion process, unlike the model output. The startup time is now dominated by the filter's settling time, but the duty cycle is correctly predicted at about 50%.

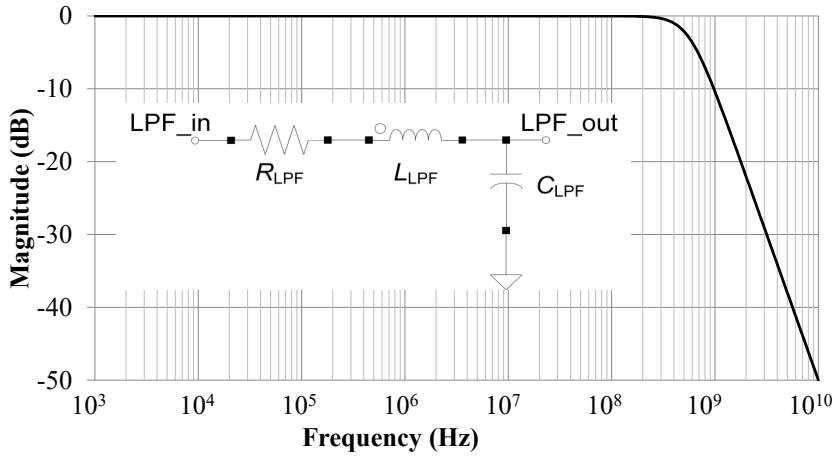

Figure 2.15: Filter design and frequency response in dB, f_{3dB} = 560 MHz [8]♠ ©2017 IEEE

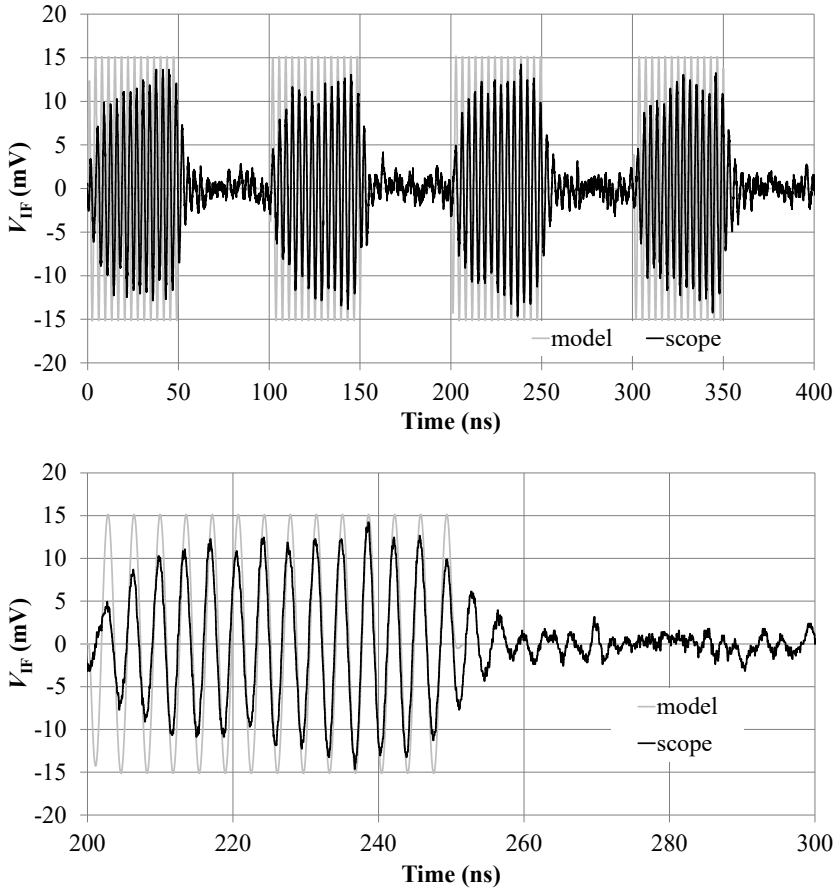

Figure 2.16: Down-converted pulses of simulated model against measurement (top) and close-up view of a single pulse with clear agreement between model simulation and measurement (bottom) [8]♠ ©2017 IEEE

3 140–220 GHz Super-Regenerative Circuits for Wireless Communication

The rising demand for high data rates in wireless communication of smart mobile devices raises interest in the millimeter-wave frequency band (30–300 GHz) due to the availability of large and unallocated contiguous bandwidth. This enables high-speed communication applications at low or moderate spectral efficiency. However, it comes at the cost of high power consumption, as the transistor gain decreases at high frequency and multiple cascaded amplifier stages are consequently needed. This problem is worsened by the high free-space path loss and the high attenuation due to weather or objects in the signal path, such that the communication link becomes increasingly less efficient as the frequency increases. An approach to overcoming these challenges has been presented in [12] by employing positive feedback in an SRO to recover phase- and amplitude-modulated data in a communication receiver, thus enabling the use of quadrature techniques to reach high data rates. Consequently, significant reductions in receiver power consumption are possible, leading to superior energy efficiency in comparison to homodyne receivers.

To prove the feasibility of efficient wireless communication using super-regenerative techniques, the following components have been investigated and characterized as detailed in this chapter. The frequency band for WR-5 rectangular waveguides that spans 140–220 GHz was chosen as a tradeoff. On the one hand, it lies at the edge of maximum achievable oscillation frequencies for SROs, up to 36% of the peak technology f_{max} at the midpoint of the range. On the other hand, it offers a wide bandwidth in the millimeter-wave band, and the high oscillation frequency lends itself well to fast switching, leading to high symbol rates. As a novel scientific research effort, it is a very challenging as well as rewarding project, since the low transistor gain at these high frequencies permits only a very tight design margin, so difficult compromises must be met. Excellent modeling is also important, since in the case of SROs, a minor deviation from the simulated gain could mean that the oscillation does not start, thus no gain from positive feedback would be possible. In fact, at the time of writing this document, no other super-regenerative circuits with high data rate requirements have yet been reported above 60 GHz.

The following performance parameters are considered as requirements for the SRO and are defined as follows:

- A **fundamental oscillation frequency of 180 GHz**, thus chosen to be in the middle of the WR-5 frequency band in order to facilitate the measurements. Although 180-GHz steady-state oscillators have been proven in the same technology, this remains a challenge for SROs as the low gain leads to slow oscillator start-up, therefore low data rates. Additionally, the already limited gain cannot be traded off for other parameters, such as output power or noise performance, which limits the design choices. Since accurate phase modulation is needed, only a fundamental oscillator can be used and this also rules out push-push oscillator techniques to extend the frequency.

- **Fast switching**, as the rate of quenching the oscillator is equivalent to the symbol rate e.g. quenching with a 10 GHz clock is equivalent to 10 GBaud. This poses another challenge, as fast switching requires fast start-up of the oscillator, and becomes less attainable as the switching frequency increases relative to the oscillation frequency. Some techniques could be used to speed up the oscillator start-up, but it is not allowed to inject energy into the oscillator core as this could corrupt the received information.

- **Low dc power consumption** to ensure energy efficient operation. To achieve this, the SRO relies on positive feedback in the oscillator for gain. Additionally, the switching of the oscillator further reduces the power consumption according to the following relation:

$$P_{dc}\ (\text{mW}) = D_{sw} \times P_{dc,ON}\ (\text{mW}), \tag{3.1}$$

  where P_{dc} is the dc power consumption, D_{sw} is the switching duty cycle, and $P_{dc,ON}$ is the dc power consumption in case of free-running non-switched operation. Therefore, D_{sw} should be kept small and all parts of the SRO circuit that are not needed in the OFF-state should be switched off. The use of passive mixing in the system could also ensure that the full system performance is also highly efficient.

- **High sensitivity**, which relates to the minimum input signal power $P_{inj,min}$ for which the phase and amplitude information can be coherently regenerated in a way that is distinguishable from noise. Counter-productively, it has been found that slower SRO quenching leads to better sensitivity [28], so this must be traded off against fast switching requirements.

- **Moderate output power** $P_{out,max}$, which in combination with the low $P_{inj,min}$ derives the maximum SRO gain $G_{SRO,max}$ as below:

$$G_{SRO,max}\ (\text{dB}) = P_{out,max}\ (\text{dBm}) - P_{inj,min}\ (\text{dBm}) \tag{3.2}$$

  However, the output power should not be so high that it drives the mixer into compression, as this would lead to the loss of amplitude-modulated information.

- **High SRO gain**, which is needed to compensate the losses of the received signal in free space and inside the receiver chain e.g. due to passive mixing.

The following sections present three SRO designs, a passive mixer, as well as other passive components that have been used to fulfill the system requirements. Packaging of the millimeter-wave SRO into a WR-5 waveguide module is then presented. Finally, an experimental system setup is discussed, complete with a high data rate wireless transmission.

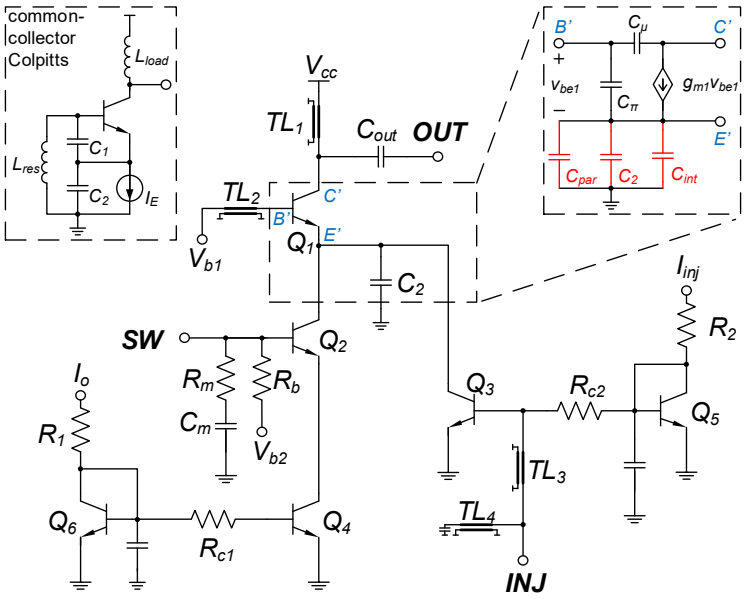

Figure 3.1: Schematic of the single-ended Colpitts-based SRO1. The small-signal representation of the oscillation core is depicted. RF signals are highlighted in bold [24]♠ ©2016 IEEE

3.1 SRO1: A 160-GHz Single-Ended Colpitts SRO

The availability of bandwidth in the mm-wave frequency range above 100 GHz is attractive for multi-Gb/s wireless communication applications. Moreover, the smaller wavelengths of the signals employed reduce the form factor of antennas and enable them to be integrated on the transceiver chip, reducing consequently the system footprint and allowing new applications. However, low transistor gain at high frequency requires several amplifier stages, which lead to large chip sizes, increased cost and power consumption. An approach to overcome these challenges has been presented in [12] by employing positive feedback in an SRO to recover phase- and amplitude-modulated data in a communication receiver, thus enabling the use of QAM schemes to reach high data rates. The SRO acts as a regenerative amplifier with high single-stage gain, and the use of pulse self-mixing [29] circumvents the need for a dedicated local oscillator for down-conversion of the received signal, further simplifying the system architecture and reducing power consumption in the receiver [24]♠.

3.1.1 Circuit Design and Layout

The circuit is based on the common-collector Colpitts oscillator, in which feedback by the capacitive divider C_1 and C_2 is used to produce the oscillation, as shown in Figure 3.1. The frequency of oscillation is given by

$$f_{osc} = \frac{1}{2\pi\sqrt{L\left(\frac{C_1 C_2}{C_1+C_2}\right)}}. \tag{3.3}$$

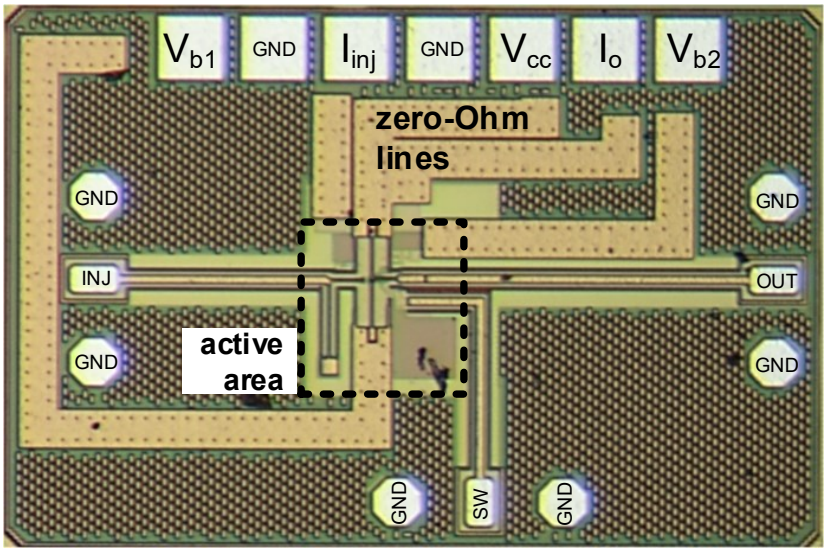

Figure 3.2: Micrograph of SRO1. Area = 990 × 650 μm^2 [24]♠ ©2016 IEEE

To achieve a high f_{osc}, C_1 was set to the minimum that is the transistor's intrinsic base-emitter capacitance C_π, which is scaled down by the small technology feature size. Additionally, C_2 was set to a correspondingly small value. The parasitic capacitances thus become significant, and are modeled in Figure 3.1 by C_{int} and C_{par} for the interconnects and transistors parasitics. They were estimated using EM and circuit simulation tools. f_{osc} is therefore determined by their equivalent $C_2' = C_2 + C_{int} + C_{par}$. The load and the resonator inductors are realized as transmission lines TL_1 and TL_2. Transistors Q_2 and Q_3 are also kept as small as required by the design, and transistor Q_1 reuses the current from both transistors. Transistor current gain β is larger than 300 at the chosen bias. The choice of the circuit architecture and the small transistors enables fast operation at low dc power.

The information signal is injected into the tank through transistor Q_3, which also acts as a buffer to isolate the SRO from leakage signals in the receiver. The switching signal is applied to the base of Q_2, which periodically stops the oscillation by driving down the voltage at its emitter node, turning off the tail current mirror (Q_4 and Q_6) during the off-phase. A sinusoidal signal is used for switching, which reduces the generation of harmonics close to the frequency of operation, in comparison to rectangular pulses. These harmonics could otherwise cause self-locking to the switching signal transients, resulting in reduced sensitivity of the SRO.

The total chip area including the pads is 0.64 mm^2 but the active part occupies a much smaller area of approximately 0.05 mm^2. Zero-Ohm lines distribute the dc bias from the pads to the circuit core as in [30]. This helps to provide a reliable ac ground where needed, which is especially critical for single-ended high-speed designs, as well as to provide good isolation from supply noise and back leakage of the SRO's own output.

3.1.2 Spectrum Analysis using a Vector Network Analyzer

To overcome the lack of both time-domain and direct spectrum analysis capabilities in the frequency range of interest at the time, a measurement method was investigated using a vector network analyzer and frequency conversion modules for the 140–220 GHz band, which is

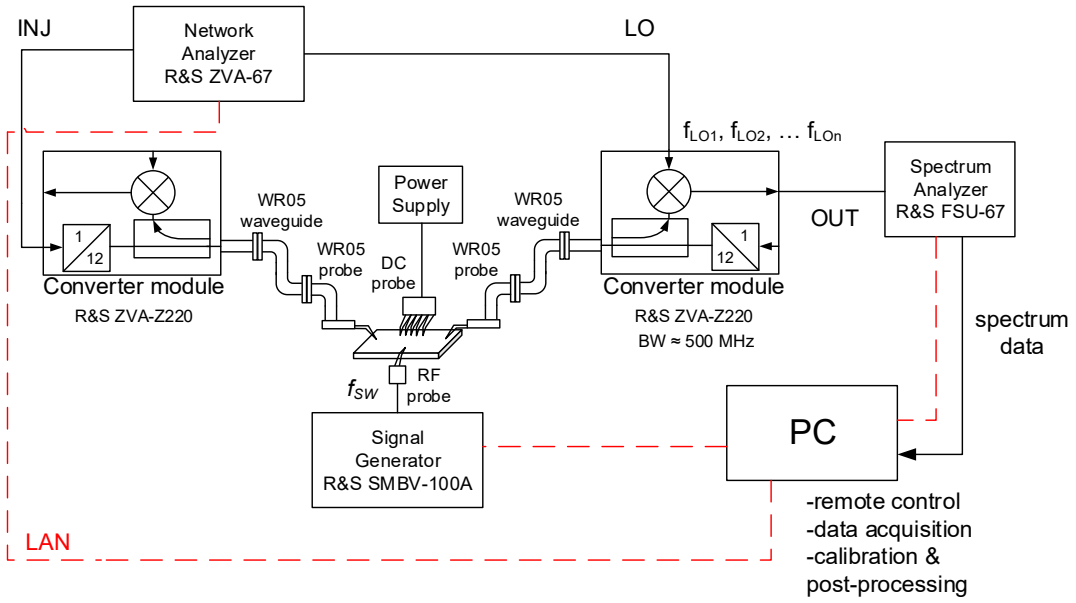

Figure 3.3: Measurement setup for wideband spectrum measurement of the SRO output. A PC-controlled loop is set to aggregate a picture of the full WR-05 spectrum from many smaller 300-MHz measurements limited by the converter modules bandwidth [24]♠ ©2016 IEEE

shown in Figure 3.3. The injection signal is generated by the network analyzer and multiplied by 12 in the converter module to the desired frequency. The output signal is subharmonic-mixed with the LO signal and fed to a spectrum analyzer operating at IF. Through this approach, the limited bandwidth of the converter modules is extended to cover the whole band by sweeping the LO frequency and aggregating the spectrum measurements for seamless acquisition. This also has the advantage of utilizing the relatively low conversion loss of these modules, resulting in an increased dynamic range over most external mixers.

To remove spurious components that arise from mixing odd LO harmonics with the RF signal, the data is recorded twice, accounting for both signal configurations in relation to LO (RF <> LO). The data is compared for both measurements at each frequency point and the minimum power reading is taken to suppress spurious power while keeping the down-converted RF power. This has the disadvantage of measuring a slightly lower RF power by always taking the measurement with the higher conversion loss. Care is taken during data acquisition at the spectrum analyzer to optimize the number of sweep points for a sufficiently coarse power detection (e.g. 1 MHz/sweep point), in order to avoid inaccuracies related to oscillator jitter. The data is power-calibrated to account for the losses of the frequency converters, the waveguides and the probe tips using a power meter, and the input/output measurements are presented at the wafer pads. A commercial PC is used to remotely control and synchronize the instruments, do the data acquisition, as well as the data post-processing for spurious removal and power calibration.

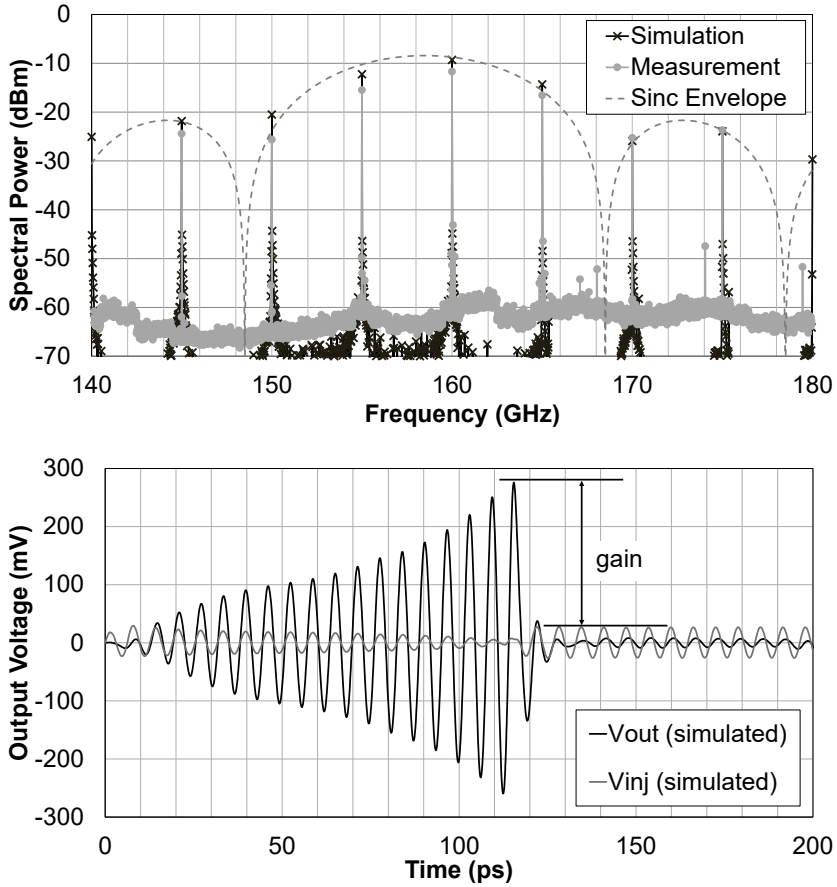

Figure 3.4: SRO spectrum measurement and simulation for $f_{inj} = 160$ GHz and $f_{sw} = 5$ GHz (top), and related time-domain simulation results (bottom) [24]♠ ©2016 IEEE

3.1.3 Experimental Results

To prove the concept, the SRO was characterized at $V_{b1} = 2.2$ V, $V_{b2} = 1.2$ V, and $V_{cc} = 3$ V. The power consumption is 11.1 mW during continuous operation, but falls to 6.6 mW during pulsed operation. Figure 3.4 shows the acquired output spectrum from 140 to 180 GHz, for an injection frequency f_{inj} = 160 GHz and a switching frequency f_{sw} = 5 GHz. The measurement results are compared against simulations obtained by the discrete Fourier transformation of the transient simulations of a large number of periods. On the other hand, the measurements are obtained directly in spectrum as described in section 3.1.2. The characteristic Dirac comb of the amplitude spectrum can be seen, as the oscillator locks to the injection signal. This measurable amplitude spectrum is described in its ideal noiseless case in equation 3.8.

However, this formula assumes instantaneous startup of the oscillator, thus the amplitude must be corrected for the oscillator's startup time. The SRO output shows spectral components at exactly the injection frequency f_{inj}, indicating locking, and at integer multiple offsets of the switching frequency f_{sw}. The impulse train is multiplied by a sinc envelope, which is shifted by the free-running frequency of the oscillator. Although the low spectral resolution of the measured output defined by D_{sw} hides most of the characteristic envelope, a sinc envelope was calculated according to equation 3.8 for D_{sw} = 50% and overlayed on Figure 3.4.

Due to the unavailability of time-domain measurement options at this frequency, the pulses

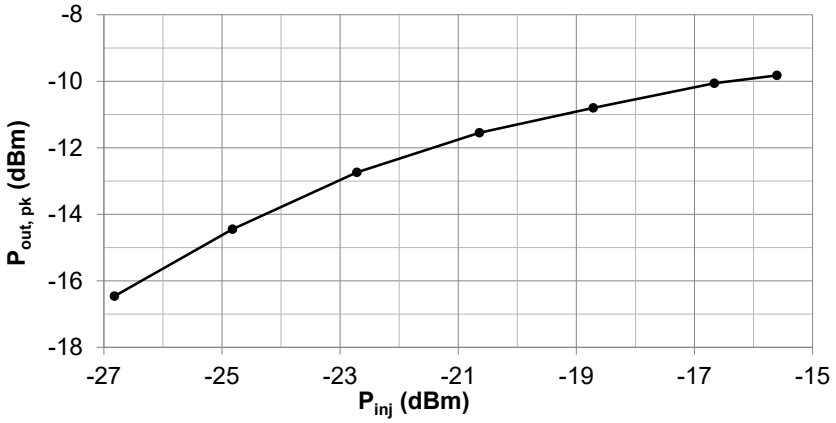

Figure 3.5: Measured maximum value of spectral power $P_{out,pk}$ vs injection power P_{inj} [24]♠ ©2016 IEEE

can only be simulated. Therefore, the time-domain simulation of one of the pulses used to produce the comparison in Figure 3.4 is presented, where an explicit definition of the gain can be given. Both the measurements and simulations were done at an injection level P_{inj} of -22.8 dBm. The maximum value of the spectral peak vs injection power was also measured and is shown in Figure 3.5 for the phase-coherent condition. This shows a sensitivity down to -27 dBm, resulting in a regenerative gain of 18.4 dB.

Figure 3.5 shows the possibility of using the SRO for amplitude modulation with high regenerative gain. In addition to that, the phase-coherent oscillation exhibited by spectrum measurements provides potential for simultaneous phase modulation, and is thus suitable for use to recover signals modulated with QAM modulation schemes [12]♠, [23]♠.

A comparison of the SRO performance against other SROs in the literature is shown in Table 3.1 at the end of section 3.3. SRO1 was the first super-regenerative circuit with phase regeneration capability above 100 GHz. It was also the first published SRO to achieve the ultra-fast switching rate of 5 GHz. The reported regenerative gain of 18 dB at a very low dc power consumption of 6.6 mW was a successful proof of concept for SROs at such high frequencies. This showed that SROs can become a competitive power-efficient alternative to conventional amplifiers at millimeter-wave frequencies, enabling novel QAM transceiver architectures to be used for high data rate communication.

On the other hand, the single-ended topology of SRO1 made it highly susceptible to common mode noise in the circuit, and limited the achievable sensitivity and gain. If passive mixing were to be used in the receiver, the SRO would have to provide more gain to compensate the losses and noise, and enable a favorable link budget with high efficiency. Output power improvements would also lead to better signal-to-noise ratio in the receiver. Thus, the need for these performance improvements led to the investigation of further SRO circuits as detailed in the following sections.

3.2 SRO2: A 148-GHz Cross-Coupled SRO

The cross-coupled topology is a common and well-understood network that realizes oscillators using positive feedback. It can be used as shown in Figure 2.6 in section 2.4 to build an SRO.

An injection input is connected to the tank for the information signal, and a switch input is added to periodically quench the oscillator [23]♠.

The coupling factor κ can be realized using feedback capacitors, which allows more flexibility for setting the loop gain without changing the tail current I_0 and, consequently, the output power. This also boosts the generation of negative conductance by reducing the effect of the base-collector capacitance, enabling oscillation at higher frequencies [31].

The time-domain response of this circuit is governed by a second-order nonlinear differential equation, which presents no closed-form analytical solution. In order to enable the circuit analysis and provide design guidelines, a model was studied by extending the work in [16]. This was implemented in the CADENCE design environment, as shown in Figure 2.8. It used components from the standard *"analogLib"* library to represent circuit blocks, with an approach similar to [22], simplifying the analysis.

The differential current of the transistor pair is described by

$$I_{diff} = I_0 \tanh\left(\frac{\kappa V_{out}}{2V_T}\right). \tag{3.4}$$

This hyperbolic-tangent relation is implemented in Verilog and included as a PCell that acts on an input voltage, and produces a corresponding current value. The powerful SPECTRE tool is used to produce a numerical transient solution of the system.

The system has a loop gain of

$$G_L = \frac{\kappa I_0 R_S}{4V_T}, \tag{3.5}$$

at the resonance frequency of

$$f_{osc} = \frac{1}{2\pi\sqrt{LC}}. \tag{3.6}$$

The system begins to oscillate upon the introduction of a small injected signal. In the absence of any noise sources, the phase of the resulting oscillation is dependent on the injected signal's phase at the moment the oscillator is turned on. Thus, the phase is said to be "sampled".

Transient simulations were run to investigate the phase coherence between the input and output signals. The oscillator was turned on at $t = 0$ and allowed to run for 1 ns. The oscillation startup is shown in Figure 3.6 for an injection amplitude of 1 nV. When the input phase is set to 90°, the output phase follows with the same shift. Also, increasing the injection amplitude by a factor of 10 causes the oscillator to start faster, which increases the pulse energy considerably if fast switching is applied. This behavior indicates in qualitative terms the potential for simultaneous phase and amplitude regenerative sampling.

To quantify the phase sensitivity, the last two zero-crossings were used to calculate the oscillation frequency, and the oscillation phase was calculated accordingly at the time of the last zero-crossing. The results for an input phase of 0° were taken as a reference, and the relative phase for an input phase of 90° was simulated. From that, the phase error $\Delta\phi$ was noted. The loop gain was varied for different coupling factors κ, and the resulting phase error was plotted in Figure 3.7. It can be seen that the optimum gain for phase coherence approaches one, which is convenient for high-frequency millimeter-wave circuits. However, this has to be traded off against startup time, which is slower for lower loop gains, if high symbol rates are

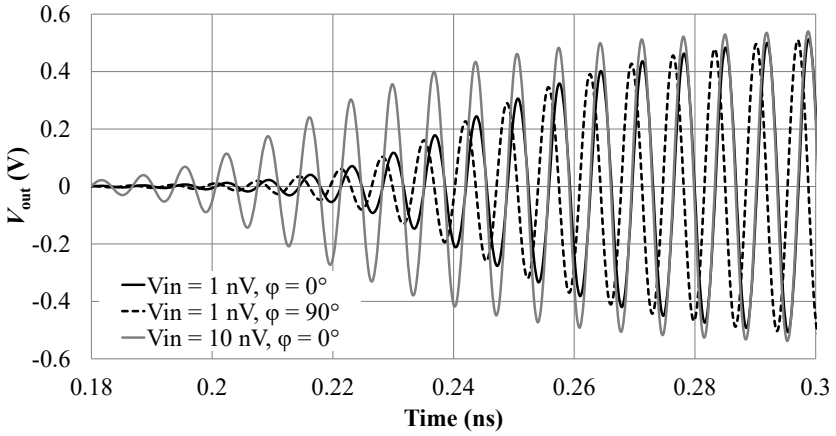

Figure 3.6: Startup response of the modeled SRO for different injection amplitudes and phases [23]♠ ©2017 IEEE

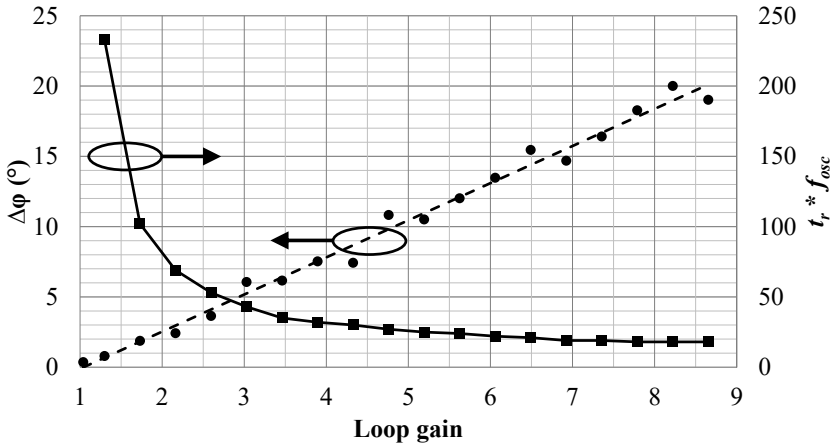

Figure 3.7: Simulated phase error $\Delta\phi$ (left) and number of startup periods $t_r * f_{osc}$ (right) vs loop gain of the oscillator. t_r is the time when the oscillation reaches 90% of its steady state level [23]♠ ©2017 IEEE

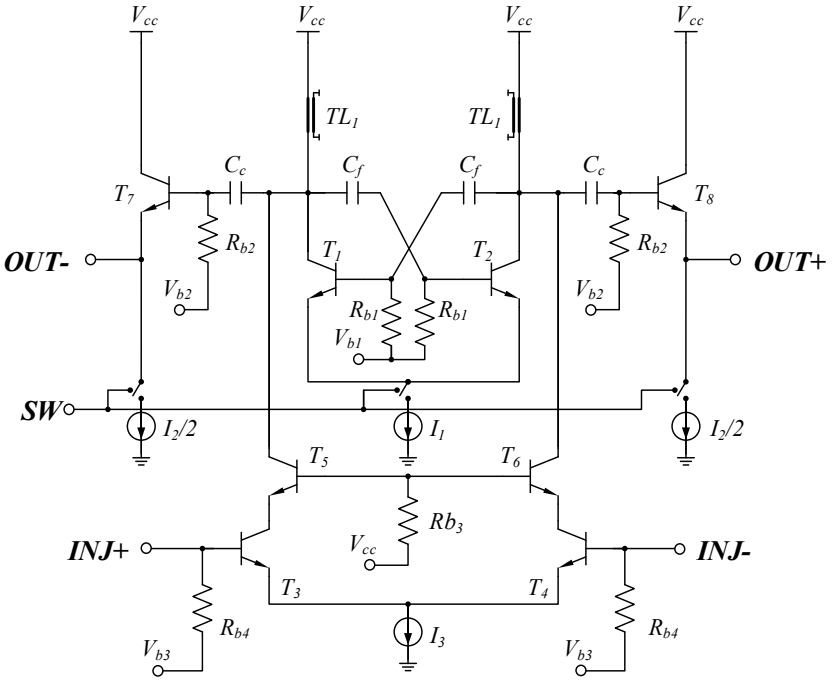

Figure 3.8: Schematic of the cross-coupled super-regenerative oscillator, with input and output buffers. The oscillator and its output buffer are switched, but the input buffer is always on [23]♠ ©2017 IEEE

desired. It is noted that, below a loop gain of 3, a phase error of only 5° is achievable. This leads to a startup time of 42 oscillation periods. Here, the startup time is defined as the time when the oscillation reaches 90% of its steady state. For comparison, half a switch period at 1 GHz comprises 73 oscillation periods.

3.2.1 Circuit Design and Layout

A common-emitter cross-coupled regenerative sampling oscillator was designed as shown in Figure 3.8. The feedback capacitors C_f couple part of the output signal from the collector of one transistor to the base of the other one, and separate the base bias from the supply. This capacitance, in addition to the parasitic capacitances in the circuit, forms the capacitance of the LC resonator, whereas the inductance is implemented as a center-tapped micro-strip.

Buffers are added for the input and output to avoid greatly degrading the quality factor of the resonator, and to guarantee the isolation between input and output signals. The input buffer is implemented as a differential cascode amplifier, which shares the inductive load of the resonator. This amplifier also acts as an active balun for the injection signal, eliminating the need for differential input signal generation, which is not readily available from laboratory setups in this frequency range. The output buffers are implemented as two common-collector stages and are ac-coupled to the oscillator output using the capacitors C_c.

The switching signal is applied to the tail current sources of the oscillator core and its output buffers. The input buffer is always on to guarantee the presence of the information signal to be sampled at the onset of oscillation. The switch is implemented as a MOS transistor and does not have an ideally abrupt switching behavior. This allows gradual quenching of the circuit

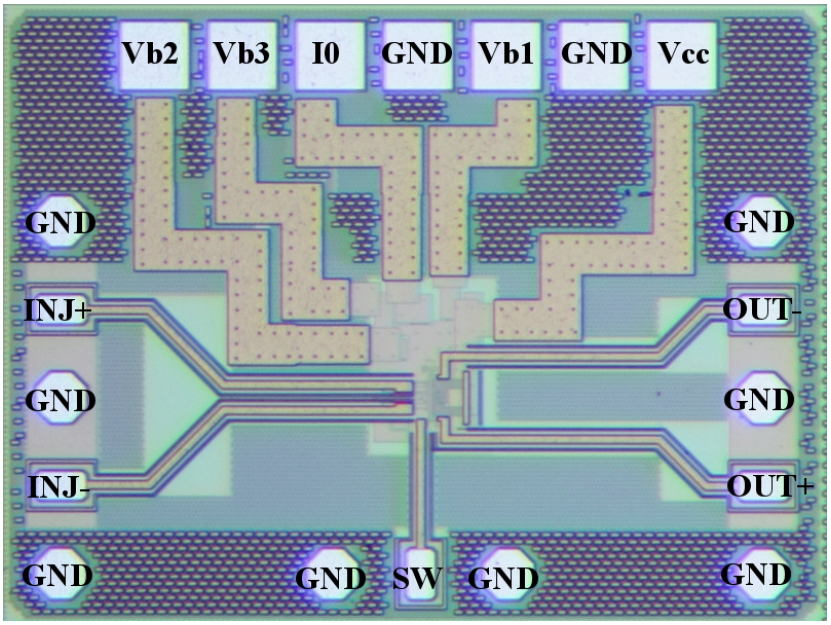

Figure 3.9: Die photo of the cross-coupled SRO chip (940 μm $\times$ 700 μm) [23]♠ ©2017 IEEE

using a sinusoidal wave, which provides a wider bandwidth than sharper switching signals. It also reduces the harmonic generation of the switch signal in the frequency range where the circuit is sensitive. This becomes more critical for high switching rates.

The dc routing was done using zero-Ohm lines, which further attenuate most of the undesired ac signal coupling [30]. The die photo of the circuit is shown in Figure 3.9. The chip was fabricated as a proof of concept over a total area of 0.66 mm^2, but the active part is very compact and occupies less than 0.03 mm^2.

3.2.2 Experimental Results

The circuit was measured at V_{b1} = 2.4 V, V_{b2} = 2.2 V, V_{b3} = 2.2 V, and V_{cc} = 3 V. The power consumption during pulsed operation is 48 mW, including input and output buffers. The frequency of operation is beyond the range of available oscilloscopes, thus the circuit can only be characterized in the frequency domain.

For the up- and down-conversion of mm-wave signals, a vector network analyzer and its frequency converter modules were used. The low bandwidth of the down-conversion mixer was extended to cover a wide range by iteratively varying the LO frequency and aggregating measurements, similar to how a network analyzer sweeps the frequency, and the IF signal was analyzed using a spectrum analyzer [24]♠. This was done because a harmonic mixer module for spectrum analysis extension was not available at the time of measurement. A signal generator was additionally used for the switching signal, and the acquired data was processed to eliminate image frequencies and power-calibrate the test setup losses. The free-running output power of the oscillator was characterized using a sub-THz power meter.

Injection was done near the free-running oscillation frequency at f_{inj} = 147.6 GHz $\approx f_{osc}$, where the oscillator is most sensitive. The injection was fed as a single-ended input to the pads and the output was taken at one of the terminals. The switch frequency was set to 1 GHz. The

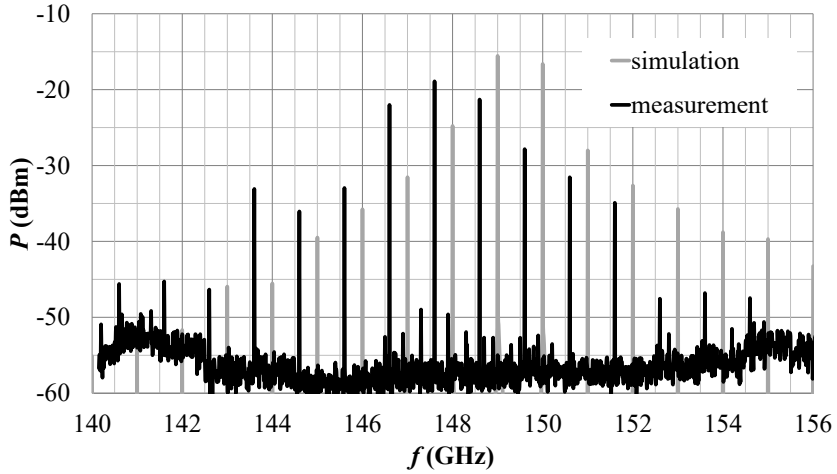

Figure 3.10: Output spectrum of the cross-coupled SRO [23]♠ ©2017 IEEE

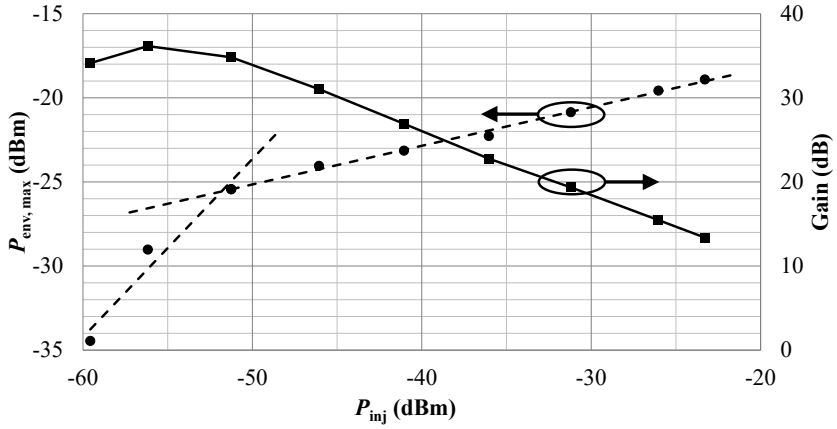

Figure 3.11: Measured maximum spectral power $P_{env,max}$ (left) and the estimated regenerative gain in dB (right) plotted against injection power P_{inj} [23]♠ ©2017 IEEE

output spectrum was recorded, as shown in Figure 3.10, for an injection power of -23 dBm. It shows a line spectrum with a spectral separation equal to the pulse repetition frequency. The component with the maximum power is locked to the exact injection frequency, and the other components decay away from it. The simulation results were obtained by running a long transient simulation of a large number of pulses and applying the discrete Fourier transform. The simulated oscillation frequency was found to be 149 GHz, which deviates very little from the measured f_{osc}, thus, and for clarity reasons, injection was applied at that frequency in simulation. The loop gain of the oscillator was also simulated using CADENCE stability analysis and found to be equal to 2.

The regenerative gain of the circuit is defined as the difference between the injection signal level and the maximum output level reached during one symbol. The output level can be assumed to be equal to the measured steady-state output power, given that the oscillator reaches the steady state before being quenched. Thus, for an injection signal level of -59 dBm and a steady-state output power of -6 dBm, the maximum regenerative gain of this circuit is calculated as 53 dB.

The maximum spectral envelope power $P_{env,max}$ is plotted against the injection power P_{inj} in

Figure 3.11 on the left axis, and the gain is plotted on the right axis. The gain is seen to start decreasing around P_{inj} = -51 dBm. This can be attributed to the point where the oscillation just reaches saturation before the oscillator is turned off. As the injection power increases beyond that point, saturation is reached faster and the output is stable for a longer duration. This translates to reduced gain and is a property of regenerative systems; the gain is higher for smaller input signals [32].

The super-regenerative oscillator is also known in recent literature as the SILO, although it has only been used to sample phase information. No work had previously been presented for simultaneous phase and amplitude regeneration in integrated SILOs. SILOs also typically have input and output at the same node for radar active reflector applications. However, since the operation principle is similar, a comparison of this work with some key parameters of reported SILOs is given in Table 3.1. SRO2 had one of the highest oscillation frequencies reported and the fastest switch rates by far. With a maximum regenerative gain of 53 dB, it significantly improved the gain over SRO1 and presented one of the best gains in a millimeter-wave circuit. SRO2 is also a compact design, owing to the smaller wavelength and the inductorless buffers. The circuit's power consumption is comparable to the best reported below 100 GHz despite the significant upscale in frequency.

Nevertheless, the bipolar cross-coupled oscillator topology proved unsuitable for oscillation frequencies above one-third of the technology f_{max}. The oscillator loop gain was insufficient to sustain fast switching above 1 GHz, thus limiting the maximum symbol rate in SRO2. The dc power consumption was significantly higher than SRO1, which lead to less efficient performance. Additionally, a frequency tuning component in the SRO would be desirable to adjust the center frequency of the system. These requirements were addressed in SRO3, as presented in the following section.

3.3 SRO3: A 180-GHz Differential Colpitts SRO

3.3.1 Circuit Design and Layout

Figure 3.12 shows a schematic diagram of the SRO circuit, including all input and output signals. The circuit was fabricated in a 130 nm SiGe BiCMOS HBT technology with f_T and f_{max} up to 300 GHz and 500 GHz, respectively [6]. The total chip area including the pads is 0.72 mm^2. A labeled micrograph of the SRO IC is shown in Figure 3.13. The oscillator core is realized with the transistors T_{1-4}, with the diode-connected transistor pair $T_{5,6}$ used as varactors for oscillation frequency tuning through the tuning voltage V_{tune} [7]♠, [26]♠.

The core is based on the differential common-collector Colpitts topology, which had proven superior performance at mm-wave frequencies [33]. A differential common-base output buffer consisting of transistors $T_{3,4}$ boosts the output power delivered to the load, and ensures sufficient reverse isolation to prevent the locking of the oscillator to reflected pulses, in case of output impedance mismatch. The input transconductance stage consisting of transistors T_{7-10} acts as an active balun, injecting differential input currents into the oscillator, similar to the input stage of the micromixer [34]. Additionally, it helps to provide a broadband match due to the low resistive input impedance, which is transformed to 50 Ω by the short transmission line segment TL_{in} as well as the pad capacitance. A small inductor L_1 adjusts the phase balance between the two balun branches.

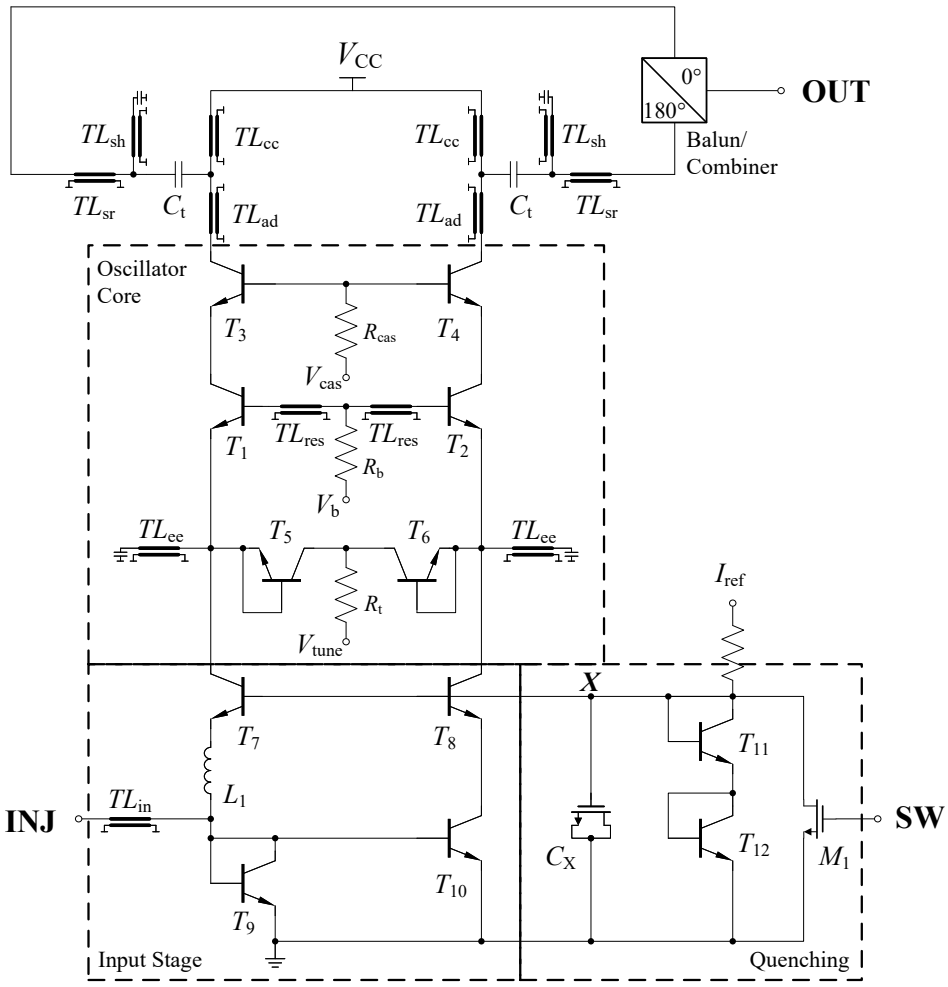

Figure 3.12: Circuit schematic of the 180-GHz SRO chip [7]♠, [26]♠ ©2019 IEEE

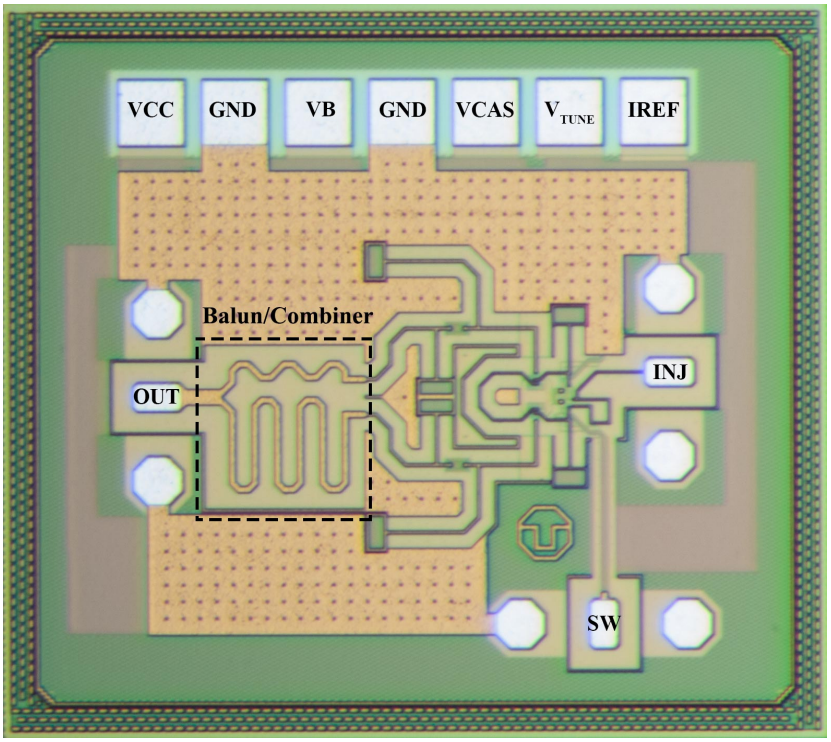

Figure 3.13: Micrograph of the 180-GHz SRO chip (area = 900 × 800 μm^2) [7]♠, [26]♠ ©2019 IEEE

The diode-connected transistors $T_{11,12}$ form a current mirror with $T_{7,9,10}$, which allows the current biasing of the oscillator through I_{ref}. T_8 maintains the voltage common-mode balance between the two differential branches. By adding the NMOS transistor M_1, a signal SW can be applied to periodically quench the oscillator as required, by sinking I_{ref} and pulling down the bias voltage node X. By adding capacitance to that node, the quenching slope of the oscillator at the turn-on instant can be slowed. This has been found to improve the SRO sensitivity in terms of the minimum input power required for low-BER phase recovery $P_{inj,min}$ [19], [28]. However, a large capacitance would limit the quench rate, thus reducing the achievable symbol rate. This slowing behavior was investigated, and simulation results for $V_X(t)$ and $V_{OUT}(t)$ are shown in Figure 3.14. The capacitance values are shown as multiples of a reference capacitance value C_0.

It can be seen from the simulations that the quench slope decreases, but the effective T_{on} also decreases, when increasing C_X. Since the target application of the circuit is in high-data-rate communication, a relatively small capacitance value of C_0 was chosen and implemented as a MOS capacitance.

To determine the optimum load impedance for the SRO, load-pull circuit simulations were carried out. In this case, the highest output power was not the only goal, since fast oscillator startup was also important in order to achieve high symbol rates. From oscillator theory, the maximum amplitude is dependent on the real part of the admittance $R_P = 1/\mathrm{Re}(y_{11})$ according to the relation

$$V_{max} = \frac{2I_0R_P}{\pi} \tag{3.7}$$

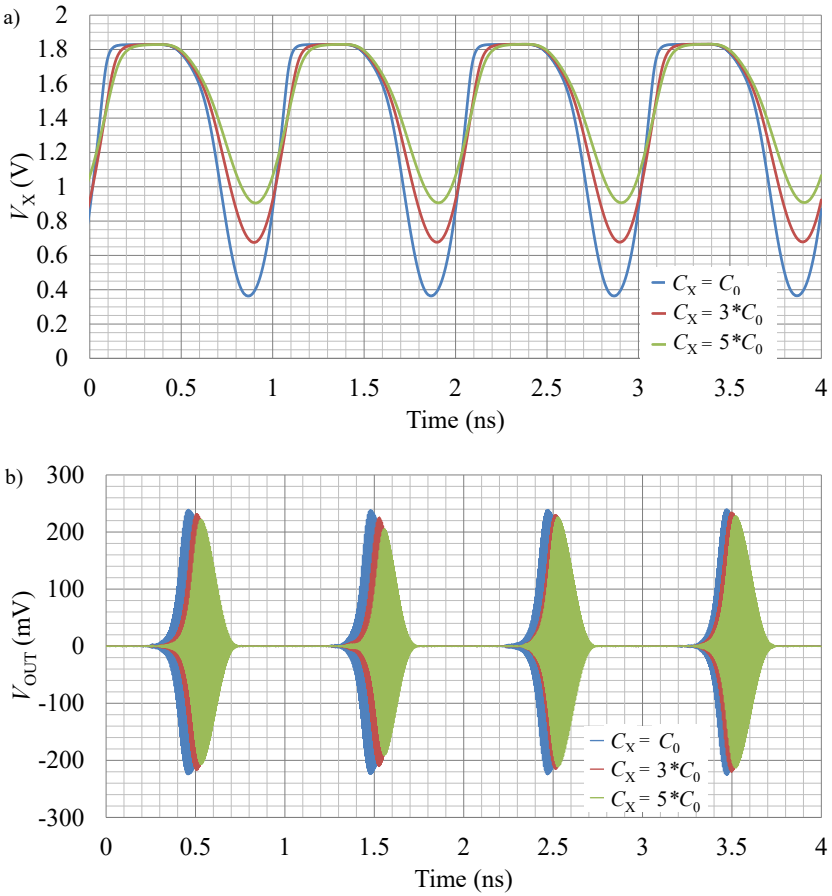

Figure 3.14: Transient simulations for (a) node voltage V_X and (b) output voltage V_{OUT}, for different node capacitances C_X [7]♠ ©2020 IEEE

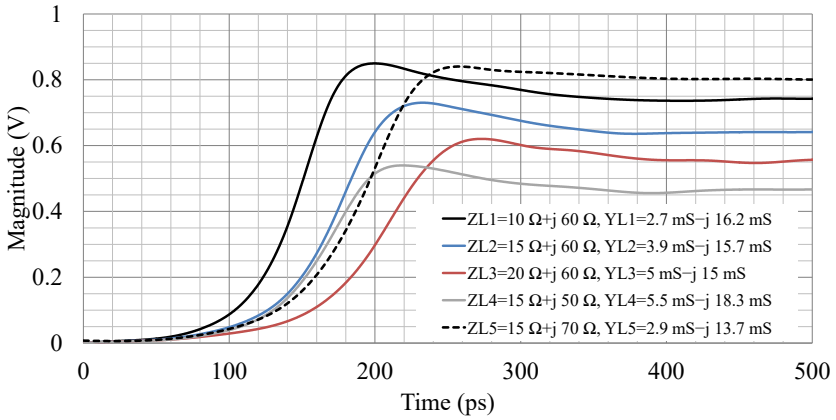

Figure 3.15: Load-pull simulation results showing the SRO transient envelopes for different load impedances and the corresponding admittances [7]♠ ©2020 IEEE

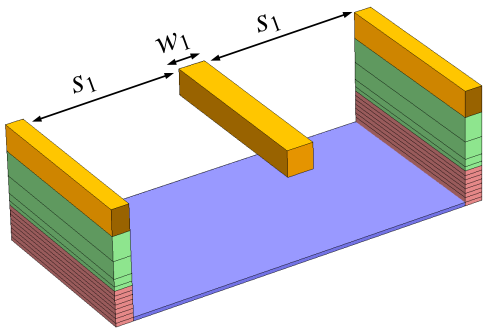

Figure 3.16: 3D view of the shielded microstrip lines used for signal routing and impedance transformation [7]♠ ©2020 IEEE

where I_0 is the tail current. On the other hand, R_P also increases the RC time constant of the load, leading to a slower start-up. The reactive inductive part, therefore, has to be tuned to resonate with the capacitive part, leading to a fast start-up. Thus, a large R_P is required for a large swing, and a moderate inductance value L_P is required for a fast start-up.

The simulated transient amplitude envelopes are shown in Figure 3.15 for different load admittances. In this case, Y_{L1} would therefore be the optimum load, since it achieves the fastest start-up and a high output swing. Capacitive loads were not considered since they increase the time constant, leading to slow startup.

The transmission lines TL_{ad}, TL_{sh} and TL_{sr}, as well as the capacitors C_t and the supply feed lines TL_{cc} were used to implement the impedance transformation network at the output. All transmission lines were implemented as shielded microstrip waveguides as shown in Figure 3.16 at a characteristic impedance of 85 Ω. The differential outputs are combined in a passive microstrip balun, which consists of one $\lambda/4$ and one $3\lambda/4$ transmission line segments, both with a characteristic impedance of 71 Ω [25]♠. The balun also performs the function of impedance transformation of single-ended 50 Ω to differential 100 Ω. Section 3.4 describes the design and characterization of this 180-GHz balun network in more detail.

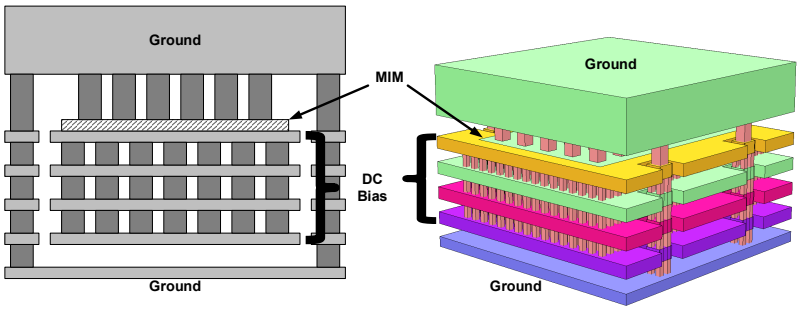

Figure 3.17: Cross-section (left) and 3D view (right) of version 2 of the zero-Ohm line used for dc bias distribution (cell dimensions = $a \times a$) [7]♠ ©2020 IEEE

3.3.2 Zero-Ohm Lines for dc Routing

The design and modeling of dc distribution networks is an important part of the study of millimeter-wave ICs. A uniform highly capacitive and low loss network is preferred in order to provide a low impedance connection to all bias points in the circuit. In some cases, even small inductances could lead to feedback loops that, in turn, lead to oscillations and render the whole system useless. Therefore, careful modeling of the dc network is advised, in order to accurately simulate and correct such problems. These computational problems become increasingly costly for circuits operating at high frequencies, since the networks would have to be divided into many small parts relative to the smallest wavelength, which all have to be solved separately [30].

A more efficient and reliable solution is derived from transmission line theory. Using the technology metal and MIM layers, a highly capacitive cell with fixed geometry and dimensions is designed. This cell can be then arranged in long stripes forming a transmission line with a very low characteristic impedance, which is close to 0 Ω. This line is, thus, called a zero-Ohm line, and it enables much simplified modeling, as the problem is reduced to solving a small cell once. The full zero-Ohm line can then be modeled as a cascade of cells and included in the circuit simulation using CAD tools.

In this circuit and following circuits, the dc routing is done using multi-layer high-capacitance zero-Ohm lines, which are shown in Figure 3.17 for a unit cell side length of a. They are designed to minimize their resistance and inductance, while increasing their capacitance, thus having a line characteristic impedance close to 0 Ω [35]. The use of the MIM layer increases the capacitance further, leading to a small footprint, or improved performance for a given area. This ensures a good and reliable ac ground up to very high frequencies where needed.

The main advantage of using zero-Ohm lines rather than MIM decoupling capacitors is the ease of modeling, since transmission line theory can be used to reduce their analysis to a single unit cell, and costly EM simulations of the full dc routing structure can be spared [36]. The R, L, G and C parameters and the characteristic impedance of the unit cell are simulated at 180 GHz as

$$R_{0\Omega\prime} = 14.8\ \mathrm{k\Omega/m},$$

$$L_{0\Omega\prime} = 51.9\ \mathrm{nH/m},$$

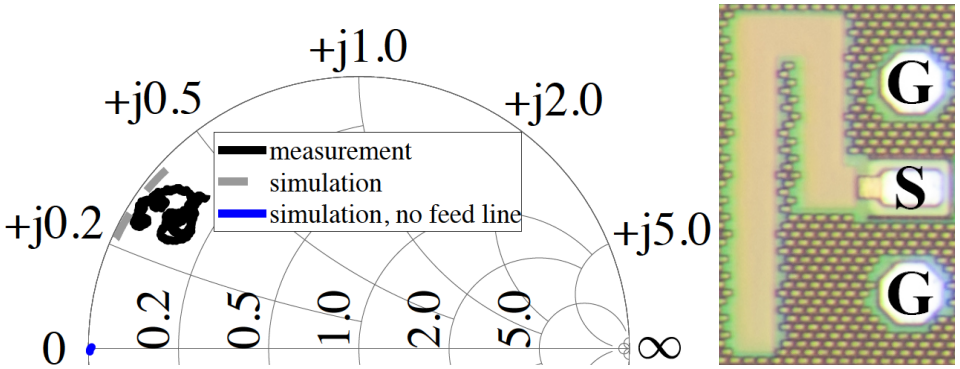

Figure 3.18: Simulated and measured input impedance of a zero-Ohm test structure (left) with a total 4×53 unit cells over the frequency range 140–220 GHz, and a micrograph of the structure (right) showing GSG pads [7]♠ ©2020 IEEE

$$G_{0\Omega\prime} = 546.4\ \mathrm{S/m},$$
$$C_{0\Omega\prime} = 10.1\ \mathrm{nF/m},$$
$$Z_{0,0\Omega} = 2.3\text{–}\mathrm{j}0.2\ \Omega.$$

To verify the performance of the zero-Ohm lines, the test structure shown in Figure 3.18 was fabricated and measured for the desired frequency range of 140–220 GHz, with an open-circuit load as the worst case. It is 4 unit cells wide, and has a total length of 53 unit cells. The measured and simulated input impedances show a significant imaginary part due to the small inductance of the feed line and vias (∼11 pH). This implies the importance of feeding the circuit with short low-impedance lines, preferably on the lower metals. The simulation results without the feed line show an almost ideal short circuit.

3.3.3 Experimental Results

To prove the concept, the SRO circuit was measured on-wafer with the dc and the SW pads wire-bonded on a custom PCB. The dc bias was set at V_{CC} = 4.4 V, V_{cas} = 4.1 V and V_b = 3.2 V. The circuit draws 6 mA during free-running operation. A Virginia Diodes PM4 power meter was used for signal power measurements and the calibration of measurement setup losses. For the spectrum measurements, a Radiometer Physics HM140-220 harmonic mixer was used in combination with a Rohde&Schwarz FSW67 spectrum analyzer. The CW input signal was generated using a Rohde&Schwarz ZVA-Z220 network analyzer converter.

Figure 3.19 shows the measured oscillation frequency f_{osc} and the output power P_{out} as functions of V_{tune}, with both *INJ* and *SW* inputs terminated to 50 Ω. The frequency tuning range extends between 175.9–187.7 GHz, which amounts to ±3.25%, or almost 12 GHz. The output power at 180 GHz is -2 dBm, whereas the maximum output power is 0.5 dBm.

To test the regenerative sampling capability of RF and mm-wave SROs, direct time-domain measurements are not practical. Previous work used a CW input signal of a known frequency f_{inj} and examined the spectrum as in [5], [37]. In case of phase coherence, the output spectrum

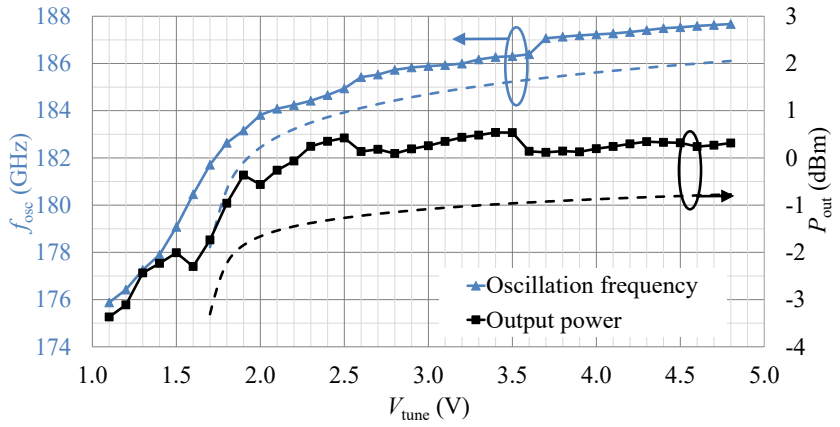

Figure 3.19: f_{osc} and P_{out} as functions of V_{tune} from measurements (solid) and simulations (dashed) [7]♠, [26]♠ ©2019 IEEE

is given by

$$V_{out}(f) = A_{out} D_{sw} |\operatorname{sinc}(\pi T_{on}(f - f_{osc}))| \sum_{n=-\infty}^{\infty} \delta\left((f - f_{inj}) - n f_{sw}\right) \tag{3.8}$$

where A_{out} is the output amplitude, D_{sw} is the duty cycle of the quench signal, and $T_{on} = D_{sw}/f_{sw}$ is the ON-state time before quenching. The spectrum consists of a sequence of Dirac delta spectral peaks at $f_{inj} - n f_{sw}$, where n is an integer, superimposed by a sinc-shaped envelope centered around f_{osc}.

Figure 3.20 shows the SRO spectrum for an input CW signal at 180 GHz and a quench rate of 1 GHz. The duty cycle is set to approximately 30%, with a dc power consumption of 8.8 mW. In Figure 3.20 (a), phase coherence is observed for P_{inj} = -58 dBm with clear spectral lines. In Figure 3.20 (b), P_{inj} is increased by 10 dB, which leads to less sampling errors and improved phase coherence, which is observed as a slight reduction of the noise floor level. The amplitude also rises due to faster SRO start-up. In Figure 3.21, quench rates of (a) 5 GHz and (b) 10 GHz are shown, with input power P_{inj} = -26 dBm.

Figure 3.22 shows simulation as well as measurement results for the peak spectral power $P_{out,pk}$ as a function of the input power P_{inj} for different quench rates f_{sw}. It can be seen that compression occurs at lower input powers for f_{sw} = 1 GHz, but the linearity improves as f_{sw} increases. This is because T_{on} effectively decreases, so the SRO is quenched before reaching saturation, resulting in better linearity. The linearity can also be improved for the 1 GHz case by decreasing the duty cycle D_{sw}. This also has the advantage of improved dc power consumption, since the SRO is turned off for a longer time.

Table 3.1 shows a comparison of SRO3 against SRO1 and SRO2, as well as other published SRO ICs in the RF and mm-wave frequency range. As previously explained, a high quench rate f_{sw} is desirable in order to reach a high data rate in wireless communication applications. However, this is not easy to accomplish, as a principal limitation of SROs is that their maximum achievable quench rate is a small fraction of the oscillation frequency f_{osc}. This is because some time is needed for the oscillation to build up to a sufficiently large magnitude, in order to reach the required regenerative gain. This is especially challenging at large oscillation frequencies close to the transistor f_{max}, since the transistor gain becomes vanishingly small

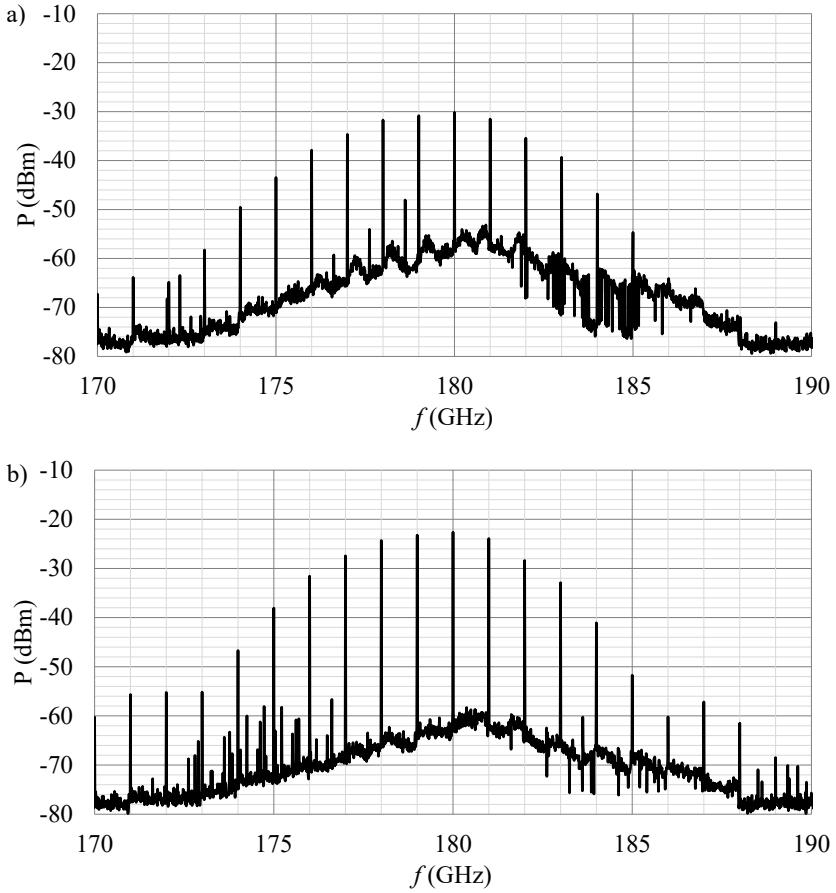

Figure 3.20: Measured SRO spectrum for f_{inj} = 180 GHz, f_{sw} = 1 GHz, and (a) P_{inj} = -58 dBm, (b) P_{inj} = -48 dBm [7]♠, [26]♠ ©2019 IEEE

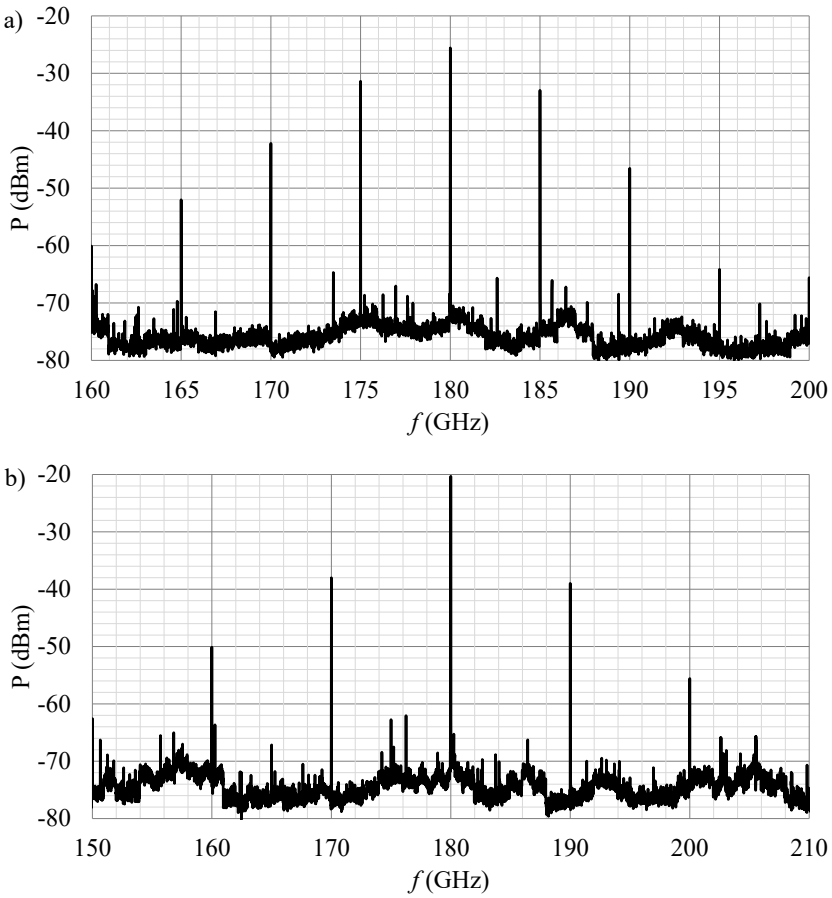

Figure 3.21: Measured SRO spectrum for f_{inj} = 180 GHz, P_{inj} = -26 dBm, and (a) f_{sw} = 5 GHz, (b) f_{sw} = 10 GHz [7]♠, [26]♠ ©2019 IEEE

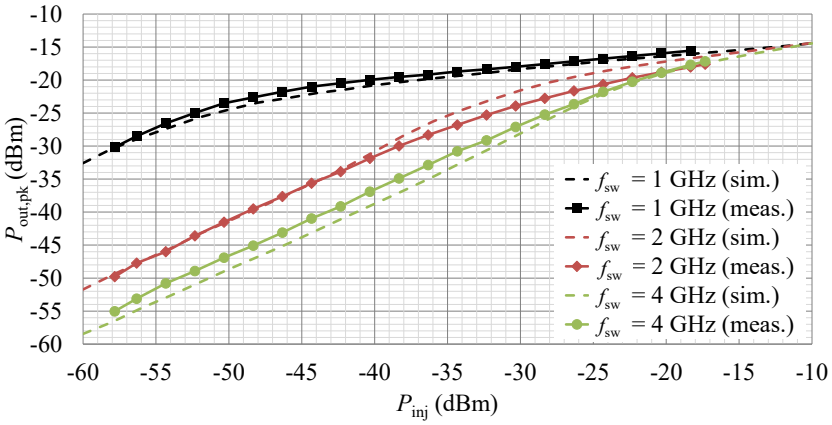

Figure 3.22: Measured and simulated $P_{out,pk}$ as a function of P_{inj}, for f_{sw} = 1, 2 and 4 GHz and f_{inj} = 180 GHz [7]♠ ©2020 IEEE

Ref.	**Technology**	f_{max} **(GHz)**	f_{osc} **(GHz)**	f_{osc}/f_{max} **(%)**	**Tuning Range (%)**	$P_{inj,min}$ **(dBm)**	P_{out} **(dBm)**	**Max. Gain (dB)**	P_{DC} **(mW)**	f_{sw} **(MHz)**	f_{sw}/f_{osc} **(%)**	**Area (mm^2)**	**AM/PM**
[38]	65 nm CMOS	N.A.	100	N.A.	N.A.	-67	N.A.	N.A.	0.9	200	0.2	0.4	AM
[39]	65 nm CMOS	N.A.	130	N.A.	2.7	-84	-13.5	70.5	8.1	12	0.009	0.3	AM
[40]	65 nm CMOS	N.A.	135	N.A.	N.A.	-76.8	N.A.	N.A.	2.8	12.5	0.009	0.26	AM
[41]	65 nm CMOS	N.A.	183	N.A.	N.A.	-72.5	N.A.	N.A.	13.5	150	0.08	N.A.	AM
[42]	180 nm SOI CMOS	N.A.	2.2	N.A.	4.5	-70	N.A.	N.A.	1.7	0.8	0.04	1.6	PM
[43]	180 nm SiGe	120	2.45	2.0	11	-110	7.5	117.5	36	60	2.4	0.76	PM
[44]	180 nm SiGe	120	2.45	2.0	12	-115	12.3	127.3	73	25	1.0	0.92	PM
[18]	180 nm SiGe	120	2.45	2.0	18	-110	12.6	122.6	69	25	1.0	0.8	PM
[45]	250 nm SiGe:C	90	6.8	7.6	N.A.	-65	-4.7	60.3	132	100	1.5	N.A.	PM
[19]	130 nm SiGe	500	25.3	5.1	5.5	-110	7.8	117.8	38	4.5	0.02	0.63	PM
[37]	250 nm SiGe	180	34.5	19.2	8	-80	5.6	85.6	122	75	0.2	0.83	PM
[46]	130 nm SiGe	500	60	12.0	7.5	-31	7.3	37	107	3100	5.2	0.75	PM
[47]	22 nm SOI CMOS	371	60	16.2	10	-42	1.5	43.5	10	10000	16.7	0.49	PM
SRO1 [24]♠	**130 nm SiGe**	**500**	**160**	**32.0**	**N.A.**	**-27**	**-8.4**	**18.6**	**6.6**	**5000**	**3.1**	**0.64**	**AM+PM**
SRO2 [23]♠	**130 nm SiGe**	**500**	**148**	**29.6**	**N.A.**	**-59**	**-6.0**	**53.0**	**48**	**1000**	**0.7**	**0.66**	**AM+PM**
SRO3 [7]♠, [26]♠	**130 nm SiGe**	**500**	**180**	**36.0**	**6.5**	**-58**	**0.5**	**58.5**	**8.8**	**10000**	**5.6**	**0.72**	**AM+PM**

Table 3.1: Comparison of reported RF and mm-Wave SRO ICs

leading to a slow start up. In order to hold a fair comparison against other SROs at different frequencies, the ratio f_{sw}/f_{osc} was introduced. Similarly, the ratio f_{osc}/f_{max} is also listed, as SRO design becomes more challenging at higher oscillation frequencies close to f_{max}.

SRO3 significantly advances the state of the art in several aspects. It has the highest reported oscillation frequency, quench rate, as well as relative oscillation frequency f_{osc}/f_{max} of 36%. The maximum regenerative gain $P_{out} - P_{inj,min}$ of 58.5 dB is the best above 100 GHz, at a competitively low dc consumption of 8.8 mW in pulsed mode.

3.4 A 180-GHz Integrated Passive Balun

Baluns are essential components for microwave circuit design because they enable the conversion between balanced and unbalanced signals for a wide range of applications. They are commonly used for differential LO generation for balanced mixers [10], [48], interfaces between differential/single-ended circuits and antennas [37], and driving differential amplifiers [49]. Baluns can be either active or passive, with the tradeoff commonly being between area and power consumption [25]♠.

The recent interest in the mm-wave frequency bands for high data rate communication presents an increasing demand for integrated balun designs at high frequencies. The low transistor gain in integrated circuits (IC) presses for low insertion loss for a positive link budget. For the passive implementations, this is often highly dependent on the skin depth and the metallization options in the respective technology. On the other hand, the smaller wavelength of mm-waves reduces the size of transmission line structures, consequently lowering their loss.

In this section, a planar monolithic balun design that is based on transmission lines is presented, thus making it broadly suited for implementation in IC technologies. A novel implementation approach is presented, which overcomes measurement difficulties of balun networks at sub-THz frequencies, and enables fabrication in low-cost metal-only runs.

3.4.1 On-Chip Port Termination Technique

Baluns are three port networks that convert single-ended signals to differential; the component requires a complex measurement procedure at high frequency for the characterization of the resulting mixed-mode S-parameter matrix. A common way to simplify this is to connect two baluns back-to-back and reduce the characterization to a two port measurement [50]. However, this approach provides no information about the phase difference between the differential ports, or the individual insertion loss of the two branches. Another simple approach is to terminate each port alternatingly and perform two-port measurements on the other ports, assuming no port coupling occurs [51]. This is the approach that is chosen for this work. Other characterization approaches that use multiple loads with known impedances at each port are not practical for mm-wave IC implementations.

An on-chip port termination was chosen due to the difficulty of differential wafer probing for waveguide-based setups. To enable fabrication in a metal-only wafer run, the termination is composed exclusively of vias and metal pads. Figure 3.23 shows a test pad that utilizes the designed termination, and its lumped elements model. The model is composed of the series

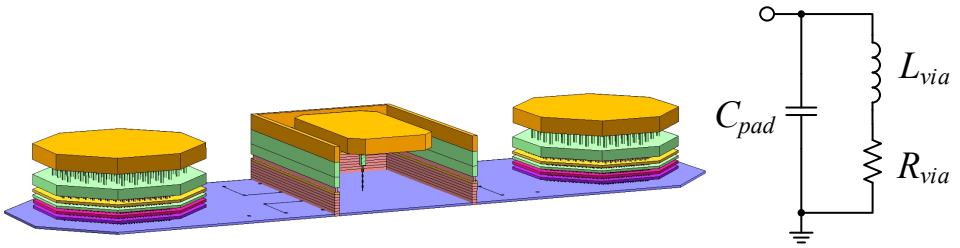

Figure 3.23: 3D view of the via stack termination (left) and lumped elements model of signal pad and termination (right) [25]♠ ©2018 IEEE

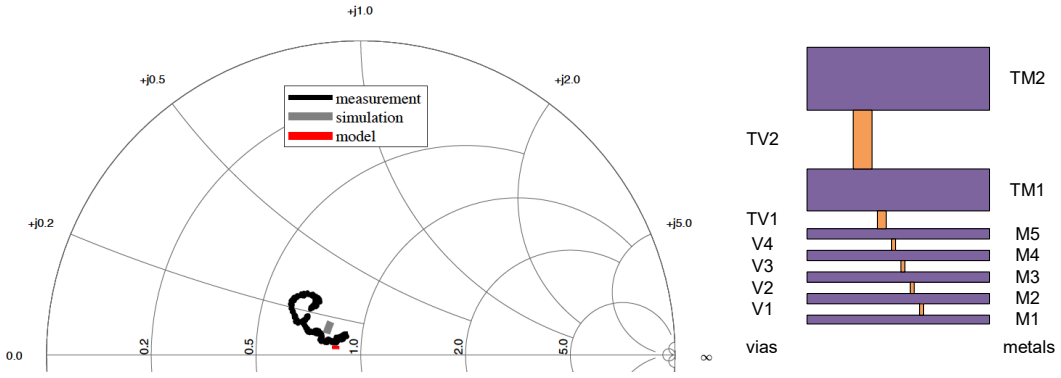

Figure 3.24: Input impedance of via stack termination based on de-embedded measurements (140–220 GHz), EM simulations, and lumped elements model (left), and to-scale metal stack (right) [25]♠ ©2018 IEEE

connection of inductances and resistances in the via stack, combined into L_{via} and R_{via}, in parallel to the pad capacitance C_{pad}.

The following expressions were used to calculate the inductances and resistances of the vias, and for simplicity also the metal pads [52]:

$$L_{via,n} = \frac{\mu_0}{2\pi}\left[h \cdot \ln\left(\frac{h+\sqrt{r^2+h^2}}{r}\right) + \frac{3}{2}\left(r - \sqrt{r^2+h^2}\right)\right] \tag{3.9}$$

and

$$R_{via,n} = R_{dc}\sqrt{1+\frac{f}{f_\delta}} \tag{3.10}$$

where

$$f_\delta = \frac{1}{4\pi\mu_0\sigma r^2} \tag{3.11}$$

where μ_0 is the permeability of free space, h is the height of the via, r is its radius, R_{dc} is its dc resistance, σ is the conductivity of its metal filling, and f is the frequency. This gives a total L_{via} of 1.8 pH, and R_{via} of 42.5 Ω at 180 GHz. The frequency dependence of the resistance is due to the skin effect; however, it is relatively small across the band as most of the lower via diameters are smaller than the skin depth. In addition to the calculated values, the via stack was simulated using a 2.5D EM solver.

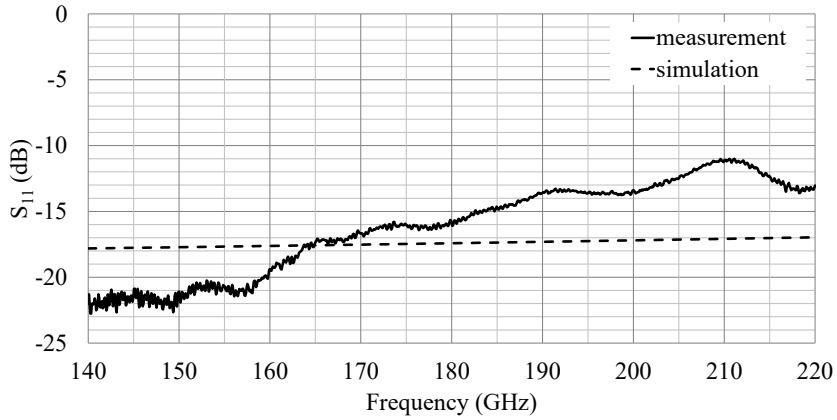

Figure 3.25: Simulated and measured S_{11} of the via stack termination [25]♠ ©2018 IEEE

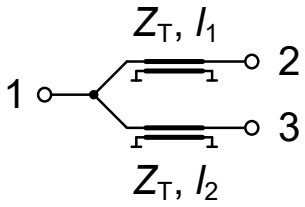

Figure 3.26: Transmission line balun schematic [25]♠ ©2018 IEEE

For validation of the results, the pad in Figure 3.23 was fabricated and characterized in the frequency range 140–220 GHz. Another unterminated – but otherwise identical – pad was measured in order to de-embed the pad capacitance. Figure 3.24 shows the impedance obtained from de-embedded measurements, EM simulations, and model calculations. Each of the three datasets shows a real impedance close to 50 Ω, in addition to a small inductive part. Figure 3.24 also shows a depiction of the metal stack of the technology drawn to scale. The measured S_{11} for the via stack termination is shown in Figure 3.25 against simulation, and shows a high return loss above 11 dB up to 220 GHz.

3.4.2 Balun Design and Layout

A schematic of the designed balun is shown in Figure 3.26, which follows the approach proposed in [50]. The balun is composed of two transmission lines with the characteristic impedance Z_T, and respective lengths l_1 and l_2. In order to provide a phase difference of 180° on the differential side, the line lengths l_1 and l_2 were chosen to be $\lambda/4$ and $3\lambda/4$, respectively, at 180 GHz. Additionally, the lines were designed to perform the impedance transformation between a single-ended impedance of 50 Ω at port 1, and a differential 100 Ω impedance at ports 2 and 3. Thus, Z_T was chosen as:

$$Z_T = \sqrt{Z_D \cdot Z_S} = 70.7\ \Omega \tag{3.12}$$

where Z_S and Z_D are the single-ended and differential port impedances, respectively.

The balun was implemented using microstrip lines, thus only requiring two metal layers. The topmost and thickest metal layer TM2 was used for the signal to reduce the loss, whereas

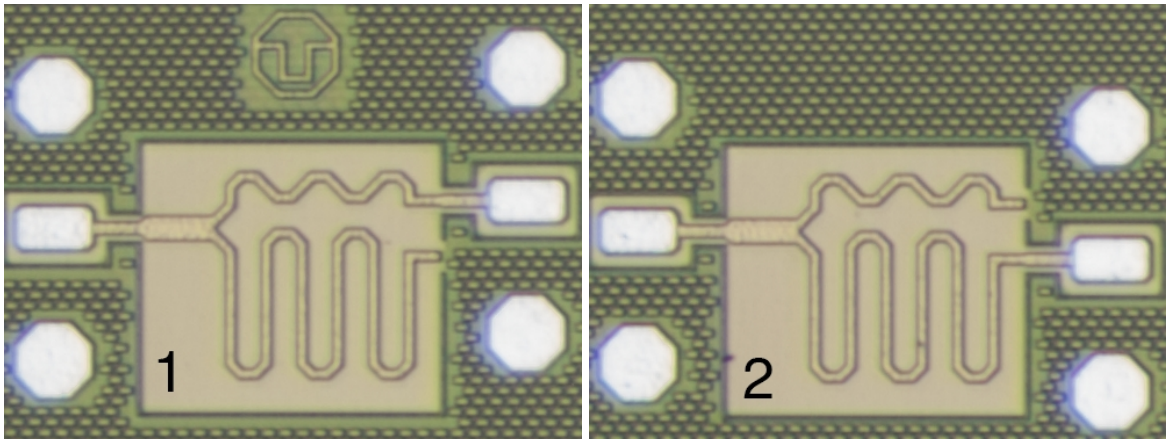

Figure 3.27: Photos of balun test structures with (1) port 3, and (2) port 2 terminated (shielded balun area = 230 × 210 μm^2) [25]♠ ©2018 IEEE

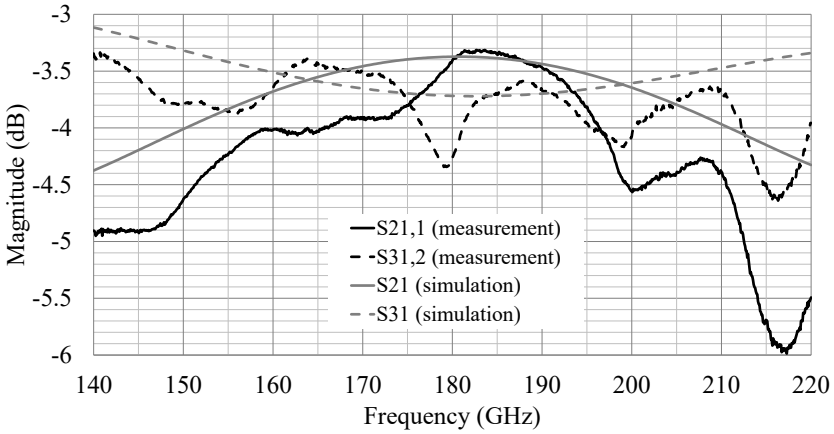

Figure 3.28: Measured and simulated insertion loss of the 180-GHz balun [25]♠ ©2018 IEEE

M1 was used for the ground. Due to the moderate line impedance, this makes the design suitable for implementation in a wide variety of process metallization options. The process used for this work is the BEOL process of a 130 nm SiGe BiCMOS technology. Moreover, the balun was enclosed inside a metal shield extending from M1 to TM2, in order to provide isolation from neighboring components. Two test structures have been fabricated, with each of the differential ports 2 and 3 terminated with the structure presented in the previous section. Their photos are shown in Figure 3.27. Thus, it was possible to measure S_{21} and S_{31} of the balun separately, as presented in Figure 3.28 vs simulations. An index number is added to the label (e.g. $S_{21,1}$) to identify the respective test structure used for the measurement.

3.4.3 Experimental Results

The on-wafer S-parameter measurements show a relatively low minimum insertion loss of 0.32 dB in the desired frequency band, and a maximum of 3 dB towards higher frequencies. A mean insertion loss of 1 dB was calculated.

The input return loss S_{11} was measured at the single-ended port for both test structures and

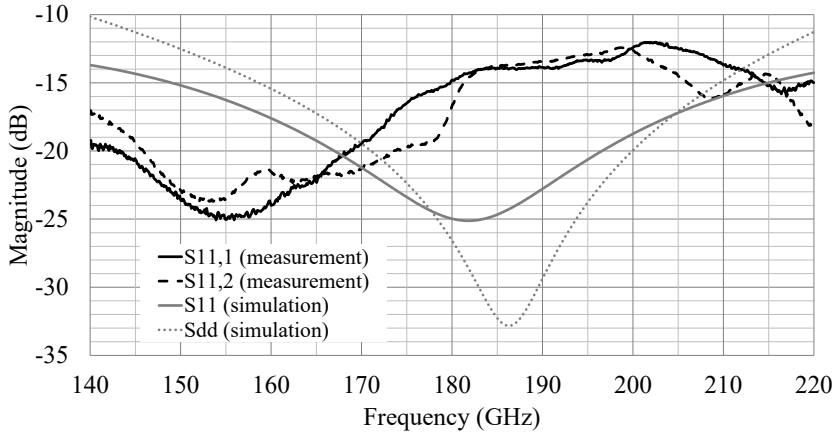

Figure 3.29: Measured and simulated return loss of the 180-GHz balun (differential port S_{dd} only simulated) [25]♠ ©2018 IEEE

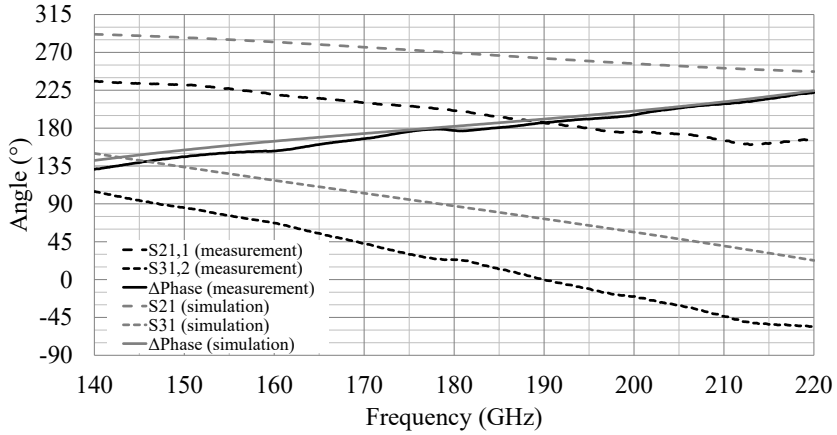

Figure 3.30: Measured and simulated phase difference of the 180-GHz balun [25]♠ ©2018 IEEE

compared against simulations as shown in Figure 3.29. It lies below 12 dB for the measured frequency band. The difference against simulations is attributed to the deterioration of the port termination towards higher frequencies. The output return loss at the differential port S_{dd} cannot be calculated from the available data as it requires information about the isolation S_{23}, which is not available from the current measurements. Instead, the simulation results based on EM simulations are shown.

To obtain the phase difference between the differential ports, the angle components of S_{21} and S_{31} were measured, and are shown in Figure 3.30 vs simulations. The absolute values were optimized in simulations to reach angular values of 90° and 270° at 180 GHz. A constant phase shift is observed in the measurements for both branches, which is due to the pads and their connections. However, this phase shift cancels out at the differential output, and the phase difference is 177.2° at 180 GHz. The phase balance is within ±5° between 174 and 189 GHz, and varies in an approximately linear trend of 1°/GHz over the measured frequency range.

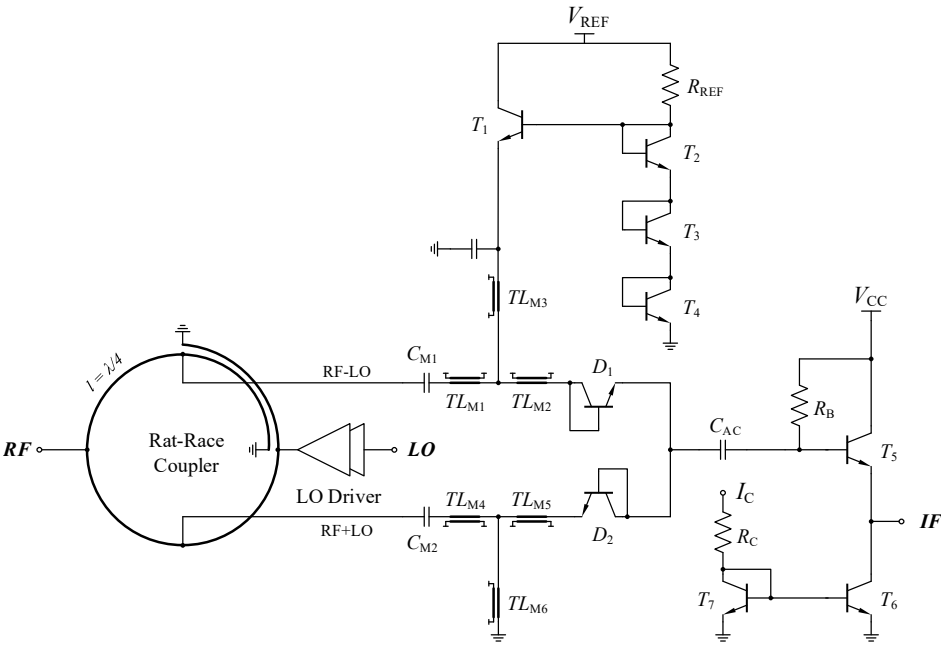

Figure 3.31: Schematic of the 180-GHz passive mixer [27]♠ ©2019 IEEE

3.5 A 180-GHz Single-Balanced Passive Mixer

For the goal of maximizing the efficiency of the receiver frontend, a passive mixer was targeted for frequency down-conversion, which would have close to zero dc power consumption. The conversion loss of the mixer could be tolerated due to the preceding high-gain SRO stage. The high linearity of passive architectures would also boost the dynamic range of the receiver. The design and layout of a passive integrated 180-GHz mixer in a 130 nm SiGe BiCMOS technology, including a broadband rat-race coupler, is presented in the next section.

3.5.1 Circuit Design and Layout

Single-Balanced Diode Mixer

Diode-connected HBTs are very well suited for realizing passive mixers for high-frequency applications, thanks to their fast switching properties [53]. A single-balanced diode mixer consists of two diodes that are connected, with opposite orientations, to two mutually isolated ports of a 4-port hybrid. Their IF outputs are connected in parallel. The RF and LO signals are injected at the other two ports of the hybrid, which are also mutually isolated. Thus, such mixers typically have good LO-to-RF port isolation [54].

A schematic of the mixer is shown in Figure 3.31, which shows the hybrid implemented as an integrated rat-race coupler. The rat-race splits the RF signal with equal phases, and generates a differential LO signal between its mixer ports. The transmission lines TL_{M1-6} form the mixer matching network [27]♠.

The IF currents due to the RF signal add at the diodes output, whereas LO noise currents are out of phase and cancel out. The IF port is single-ended, which is advantageous as it eliminates the need for bulky transformers at IF. A small dc bias current of 25 μA is provided by the network consisting of transistors T_{2-4} and is mirrored through the emitter-follower T_1

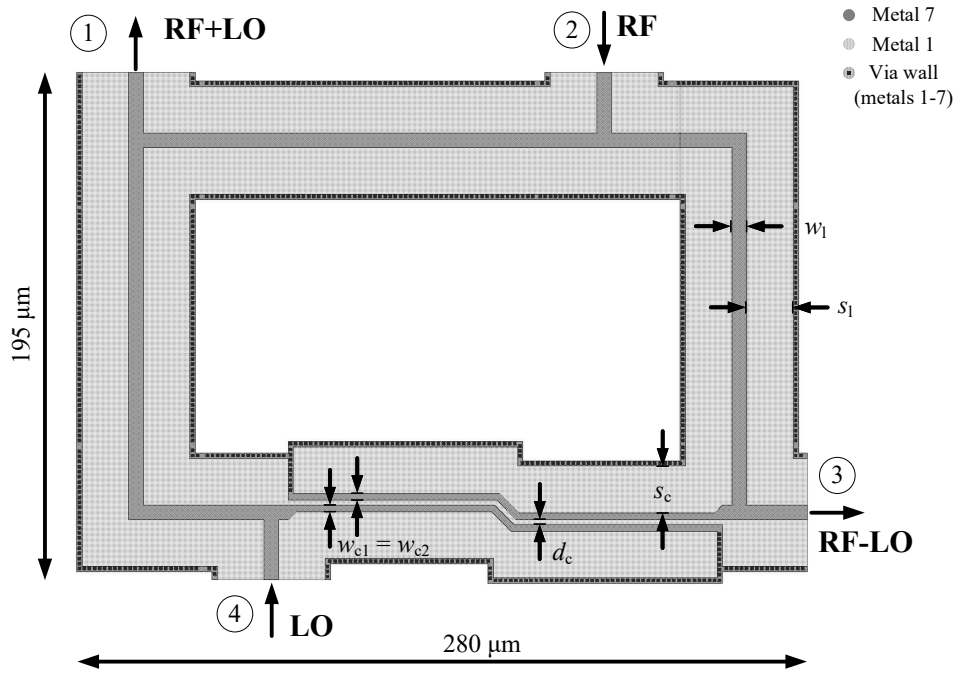

Figure 3.32: Rat-race coupler layout with the main line dimensions and port numbers depicted [27]♠ ©2019 IEEE

to the mixing diodes $D_{1,2}$. This dc current conditions the diodes in forward bias, thus reducing the LO power needed to drive the mixer. The mixer diodes are sized as small as possible in order to reduce their junction capacitances, which in turn also reduces the conversion loss.

A common-collector buffer is designed at the IF port, which presents the mixer IF output with a high-impedance load. This allows trading off IF bandwidth for lower conversion loss, and helps achieve a broadband IF port match to 50 Ω. The buffer transistors are also sized at the smallest size to reduce their dc power consumption. Additionally, the buffer output impedance is thus close to 50 Ω, which facilitates the matching.

Broadband Rat-Race Coupler

The rat-race coupler is conventionally designed as four transmission line segments connecting four ports. Three of those segments are $\lambda/4$ long, whereas the fourth has a length of $3\lambda/4$. Thus, signals injected at opposite ports are added and subtracted at the adjacent ports, while being mutually isolated.

At lower frequency, rat-race couplers are implemented off-chip due to their bulky design. However, at mm-wave frequencies, their size shrinks and they can be integrated on chip, leading to overall better performance. One other limitation of this coupler is its narrowband performance, as the required half-wavelength path difference can be met at only one frequency. This was solved in this work by replacing the $3\lambda/4$ section with a 3-dB coupled-line $\lambda/4$ section with its ends grounded. This provided a frequency-independent phase shift and impedance transformation, similar to other coupled-line hybrids. Consequently, broadband performance was achieved, as well as further chip area reduction due to the removal of the long $3\lambda/4$ section.

The layout of the rat-race coupler design is shown in Figure 3.32 with the main line dimen-

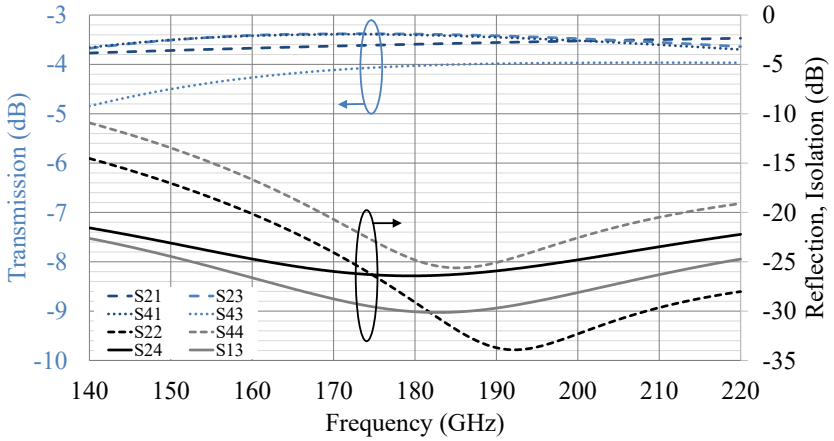

Figure 3.33: EM simulated transmission, reflection and isolation coefficients of the broadband rat-race design [27]♠ ©2019 IEEE

sions depicted. The transmission lines are implemented as grounded coplanar waveguides (GCPW) with a characteristic impedance of 70.5 Ω. The edge-coupled lines have been optimized for even-mode and odd-mode characteristic impedances of 131.9 Ω and 37.9 Ω, respectively. The topmost thick copper layer (metal 7) is used for the signal and the bottom layer (metal 1) is used as the ground shield. The output signals at ports 1 and 3 then go to a transmission-line matching network, which matches the diodes to the rat-race ports impedance of 50 Ω, as shown in Figure 3.31.

The full rat-race design has been simulated using 3D electromagnetic (EM) solvers. The simulated transmission, reflection and isolation characteristics are shown in Figure 3.33. The single-ended-to-differential insertion loss was less than 0.8 dB for the RF signal, and between 0.7 dB and 1.3 dB for the LO signal, for the whole WR-5 frequency band. The input return loss at the RF and LO ports was better than 14 dB and 10 dB, respectively, when the other two ports were matched. Port isolation was better than 21 dB. The amplitude and phase imbalances are shown in Figure 3.34, and proved to be within $\pm$0.3 dB and $\pm 6^\circ$ for the RF signal. The LO amplitude imbalance was between 0.3–1.2 dB whereas the phase imbalance was within $\pm 10^\circ$. The mixer, including the rat-race coupler and the matching networks, occupied an area of 0.13 mm^2, which was a small fraction of the total chip area as shown in Figure 3.35.

LO Driver

The LO signal power that could be generated in the lab was in the range of -20 dBm at the chip pads in the desired frequency range. Therefore, an LO driver [55] has been integrated to allow proper characterization of the mixer. This is, however, not desired in the receiver, as it would saturate the mixer and lead to the loss of SRO amplitude information. Thus, its power and area do not add to those of the receiver frontend.

3.5.2 Experimental Results

Figure 3.36 shows the measured and simulated down-conversion gain vs RF input frequency f_{RF}. The measurement is performed in 100 MHz steps for several constant LO frequencies f_{LO}. A minimum conversion loss of 6–8 dB is achieved over a wide frequency range between

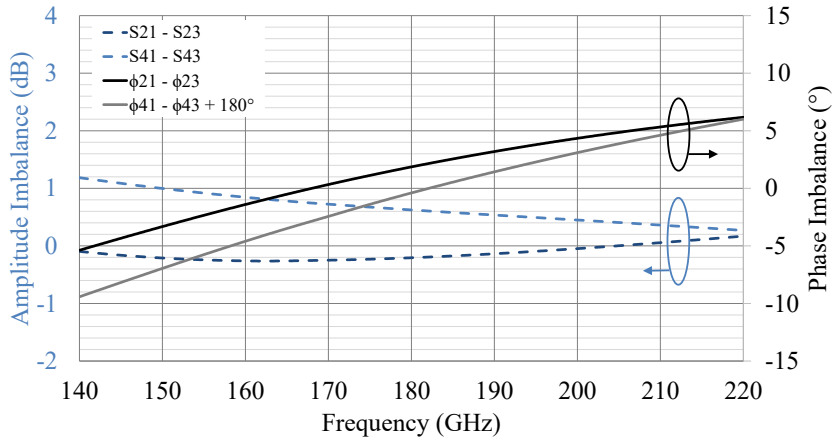

Figure 3.34: EM simulated amplitude and phase imbalances of the rat-race coupler [27]♠ ©2019 IEEE

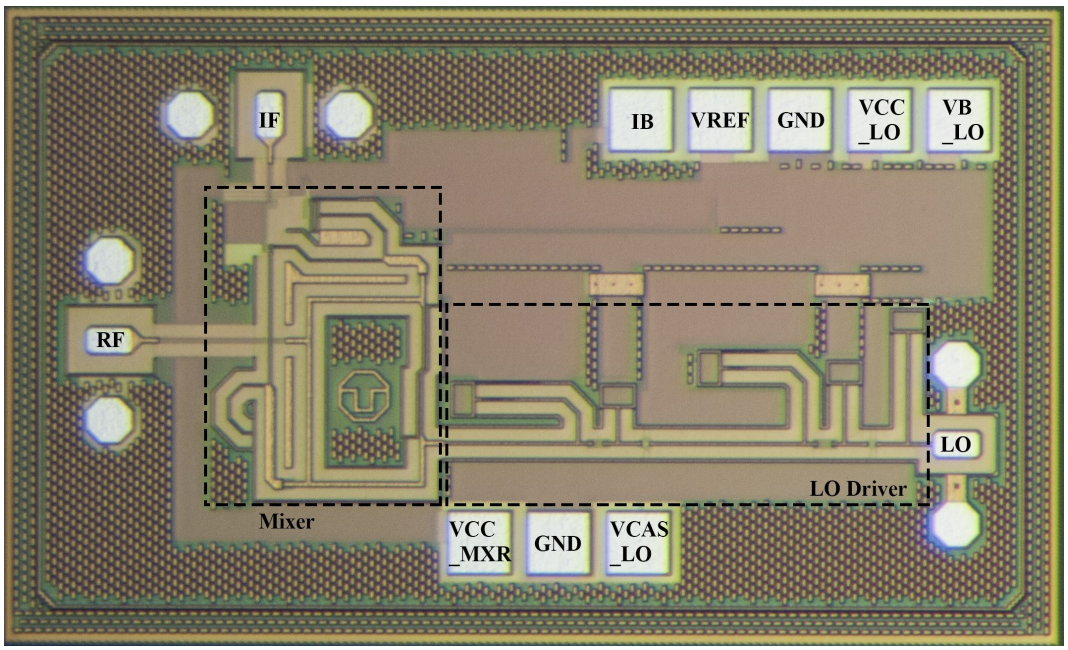

Figure 3.35: Micrograph of the 180-GHz mixer (area = 1240 × 710 μm^2) [27]♠ ©2019 IEEE

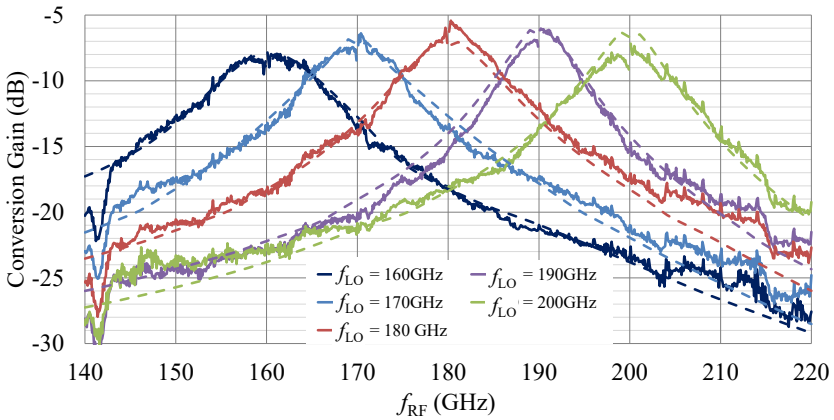

Figure 3.36: Measured (solid) and simulated (dashed) conversion gain against f_{RF} for multiple fixed f_{LO} [27]♠ ©2019 IEEE

160–200 GHz. It is worth noting that the frequency response towards lower frequency is masked by the LO driver bandwidth, which falls off below 170 GHz. In Figure 3.37, the conversion gain is shown as a function of f_{RF} in 1 GHz steps for a fixed f_{IF} of 1 GHz. The measurement shows that the mixer exhibits a very large bandwidth of 50 GHz at the RF and LO ports. This is mainly due to the broadband rat-race design. Furthermore, it is also shown through simulation that the mixer, as a standalone module without LO driver, exhibits higher bandwidth exceeding 80 GHz. The LO input power at the chip pads is also shown for each measurement and shows a weak dependence of the conversion gain to the variations of LO power due to the incorporated LO amplifier.

The dependence of conversion gain on LO input power P_{LO} is shown in Figure 3.38 for an LO frequency f_{LO} of 180 GHz and f_{IF} of 5 GHz. The results for lower-side-band (LSB) and upper-side-band (USB) signals were observed to be almost identical. The conversion gain of the mixer is almost constant above -30 dBm, and does not fall at higher levels as simulated due to the saturation of the LO driver output, which is not considered in simulation. The linearity of the mixer as a function of RF input power P_{RF} is also presented in Figure 3.39 for f_{LO} = 180 GHz and f_{IF} = 5 GHz. The mixer shows high linearity, with an input-referred 1-dB compression point of -7 dBm.

Table 3.2 summarizes the performance of integrated mixers above 100 GHz in the literature. It is shown that this work has the highest conversion gain from a passive mixer at very low dc power consumption. It is also among the most linear with an input-referred compression of -7 dBm. It requires the lowest reported LO power due to the integrated LO driver, which provides around 20 dB of gain. Without it, it still requires a competitively low -10 dBm of LO power, which makes it fit for low power applications.

3.5.3 Second Mixer Design

To address the limitation of IF bandwidth in the first mixer version, in order to enable higher data rates, a second version was realized with some design modifications. The output common-collector buffer was excluded, and an LC filter was designed to extend the IF bandwidth. The LO driver was also excluded, instead opting for laboratory waveguide components to achieve the required LO power, thus leading to cost and power savings. Additionally, port matching

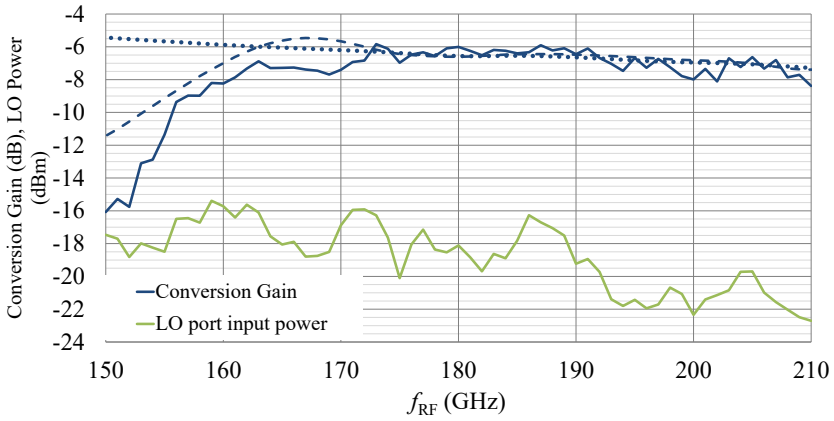

Figure 3.37: Measured (solid) and simulated (dashed) conversion gain against f_{RF} for a fixed f_{IF} of 1 GHz, along with the LO input power for the measurement. Simulation of the mixer conversion gain without LO driver is shown as a dotted line [27]♠ ©2019 IEEE

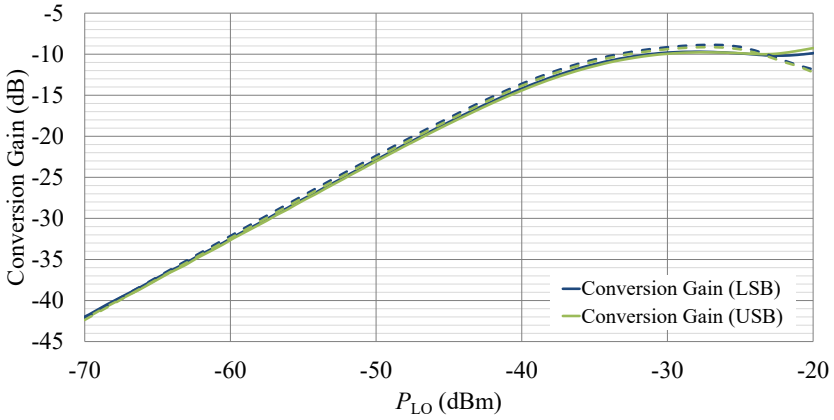

Figure 3.38: Measured (solid) and simulated (dashed) conversion gain against P_{LO} for f_{LO} = 180 GHz and f_{IF} = 5 GHz [27]♠ ©2019 IEEE

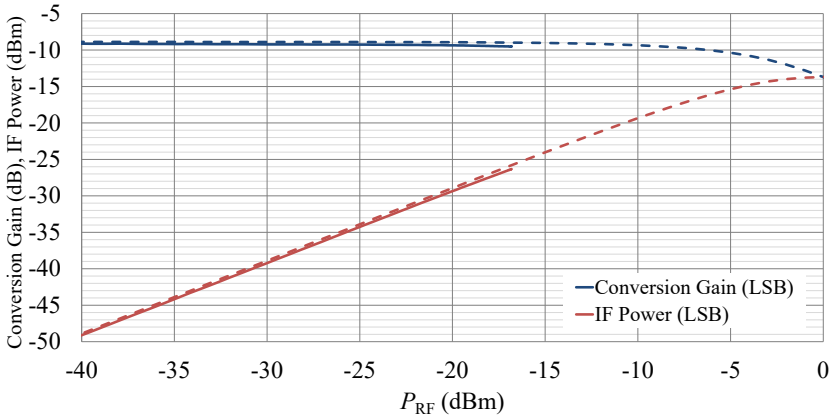

Figure 3.39: Measured (solid) and simulated (dashed) conversion gain against P_{RF} for f_{LO} = 180 GHz and f_{IF} = 5 GHz [27]♠ ©2019 IEEE

Ref.	**Technology**	**Active/ Passive**	**Topology**	f_{max} **(GHz)**	f_{RF} **(GHz)**	**Conversion Gain (dB)**	P_{LO} **(dBm)**	P_{1dB} **(dBm)**	**NF (dB)**	P_{DC} **(mW)**	**Area (mm^2)**
[55]	130 nm SiGe	Active	Micromixer	450	165–215	5.5	-20	-15	16_{DSB}	17.4	0.63
[56]	130 nm SiGe	Active	2nd-Subharmonic	435	200–230	16	0	N.A.	18	72	0.66
[57]	130 nm SiGe	Active	Gilbert	500	225–265	18	-10	-45	18	56	2.1
[58]	130 nm SiGe	Active	4th-Subharmonic	500	235–255	21	N.A.	-37	32_{SSB}	48	1.43
[59]	45 nm CMOS SOI	Active	Single balanced	280	145–165	-5	2	>-16	N.A.	10	0.33
[60]	130 nm SiGe	Passive	APDP, 2nd-SHM	300	117–124	-8	5	-4.5	8.5	0	0.6
[61]	180 nm SiGe	Passive	Schottky, 2nd-SHM	N.A.	175–200	-20	0	N.A.	N.A.	0	0.12
[62]	65 nm CMOS	Passive	Gate-pumped	210	130–170	-20.5	-5	0*	18.3	0	0.17
This work [27]♠	**130 nm SiGe**	**Passive**	**Rat-race + diodes**	**450**	**160–220**	**-6**	**-10***	**-7**	**14_{DSB}***	**2.8**	**0.88**

*simulated

Table 3.2: Comparison of IC down-conversion mixers above 100 GHz [27]♠ ©2019 IEEE

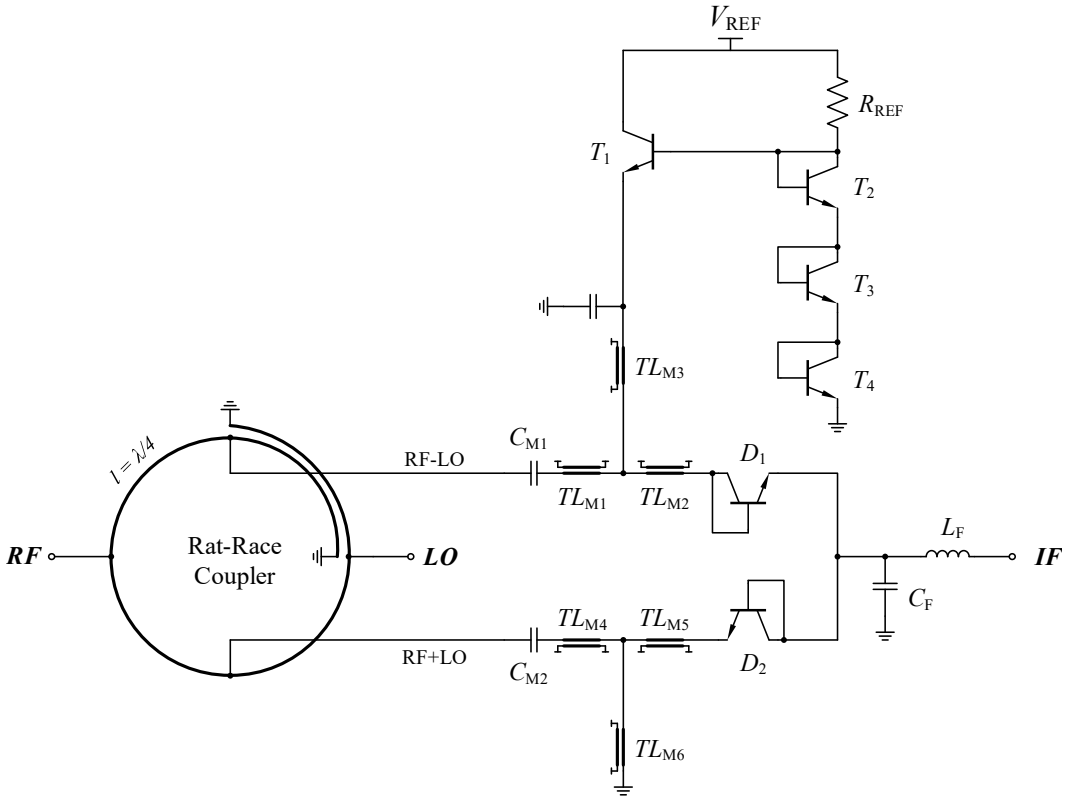

Figure 3.40: Schematic of the mixer second design

was improved at all ports. The schematic and the micrograph of the mixer redesign are shown in Figure 3.40 and Figure 3.41, respectively. The redesign features a smaller silicon area of 0.59 mm^2 compared to 0.88 mm^2 for the original design.

For a performance comparison of the two mixer versions, Figure 3.42 shows the post-layout simulation results of conversion gain as a function of f_{RF} of V2 against the simulations and measurements of V1. The post-layout simulation results of the port matching at all three ports are presented in Figure 3.43. The second version has higher conversion loss, but features significantly enhanced IF and RF bandwidth.

3.6 Proof of Concept System Measurements

In order to study the feasibility of SRO-based regeneration of a modulated signal with high data rate (>1 Gbit/s), the setup depicted in Figure 3.44 has been employed. An n-PSK modulated signal is generated in complex baseband using a digital to analog converter and applied to a 15 GHz CW carrier using a quadrature mixer. Subsequently, the constant envelope signal is up-converted to 180 GHz with a network analyzer converter, which contains

Acknowledgment: *This is to acknowledge that sections 3.6 and 3.7 contain the results of a joint work on SRO system experiments, for which my colleague at Friedrich-Alexander-Universität Erlangen-Nürnberg (FAU), Christian Carlowitz, was a major contributor. He was also a co-author of [7]♠, [26]♠, in which this work was first published. I would like to express my gratitude for his contributions.*

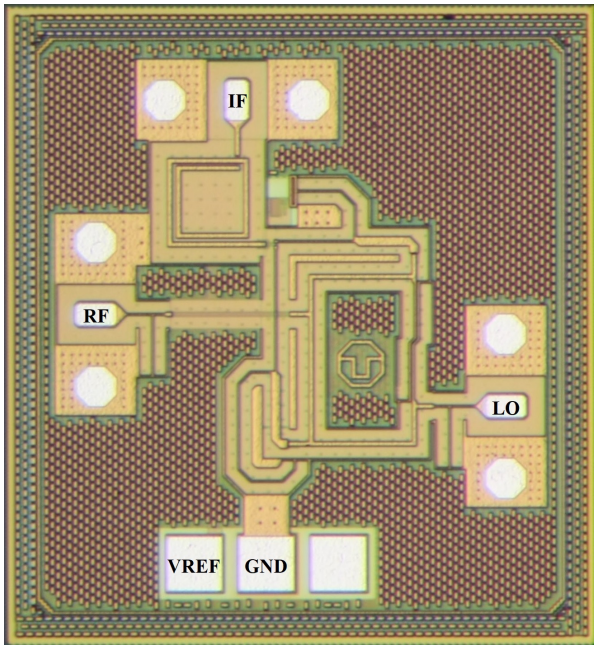

Figure 3.41: Micrograph of the mixer redesign (area = 740 × 800 μm^2)

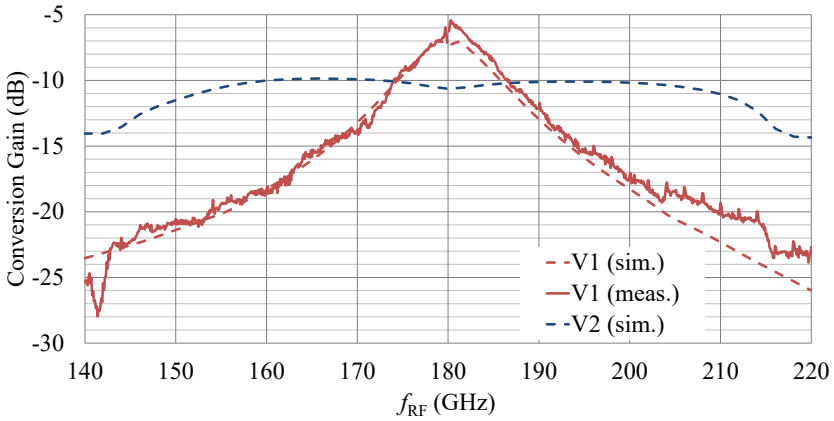

Figure 3.42: Comparison of conversion gain and bandwidth between the first design (simulated and measured) and second design (simulated) of the mixer

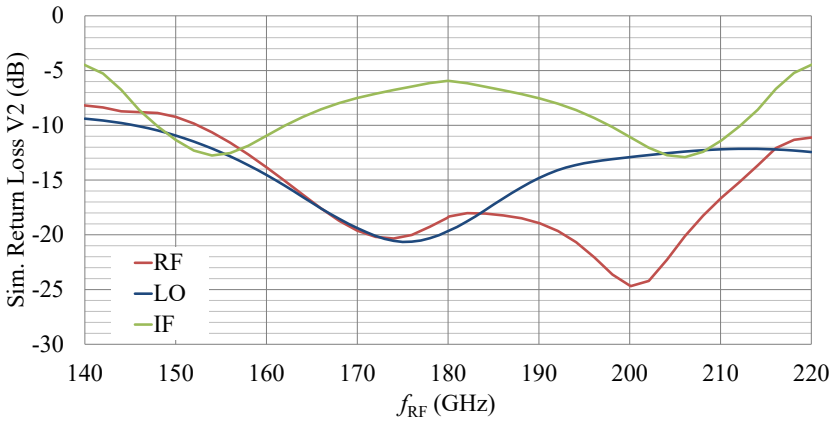

Figure 3.43: Post-layout simulation results for ports matching of the second mixer design

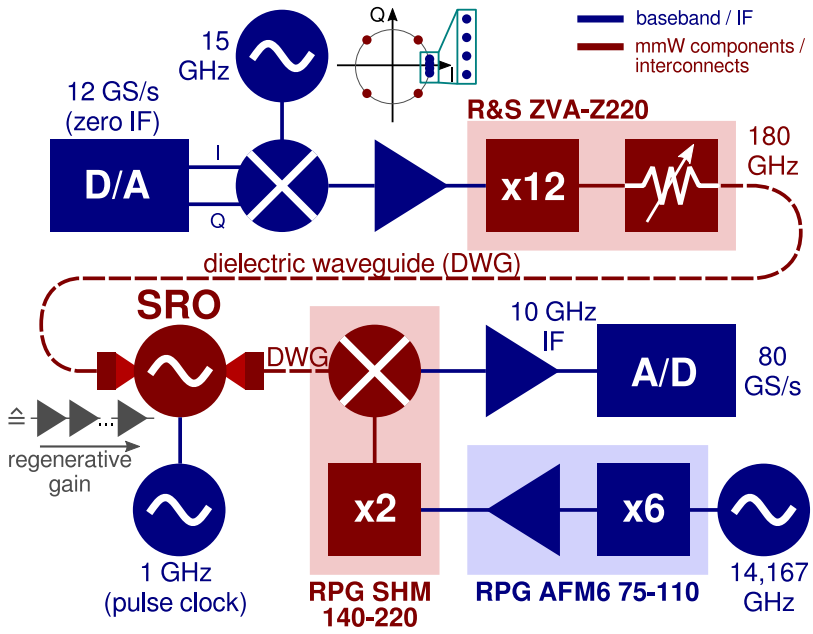

Figure 3.44: Measurement setup for demonstrating SRO-based regeneration of n-PSK modulated signals [7]♠, [26]♠ ©2019 IEEE

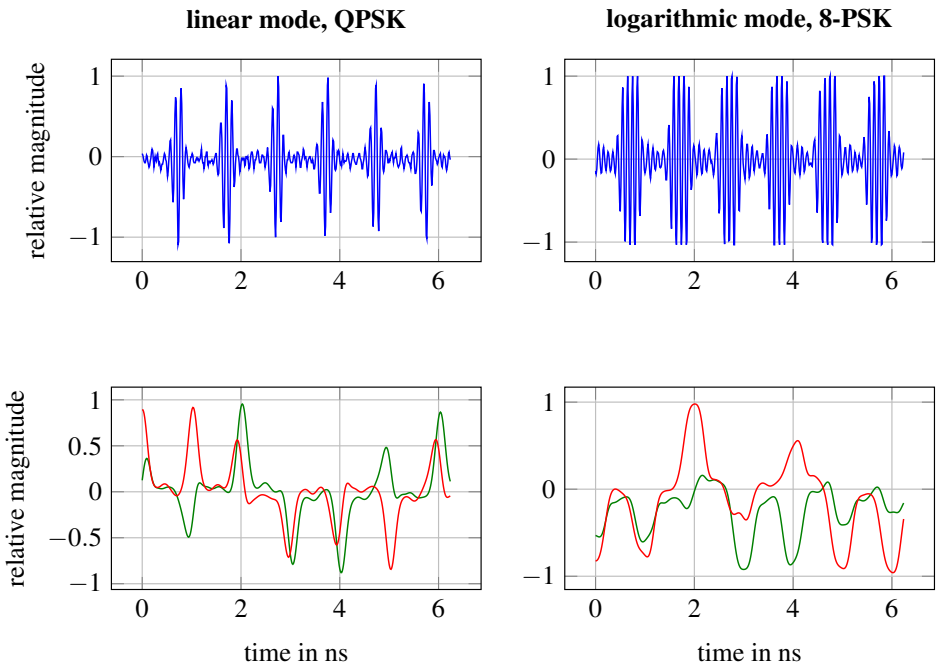

Figure 3.45: Measured IF (top) and complex baseband (bottom) signals in linear and logarithmic modes, showing the regenerated communication signals [7]♠, [26]♠ ©2019 IEEE

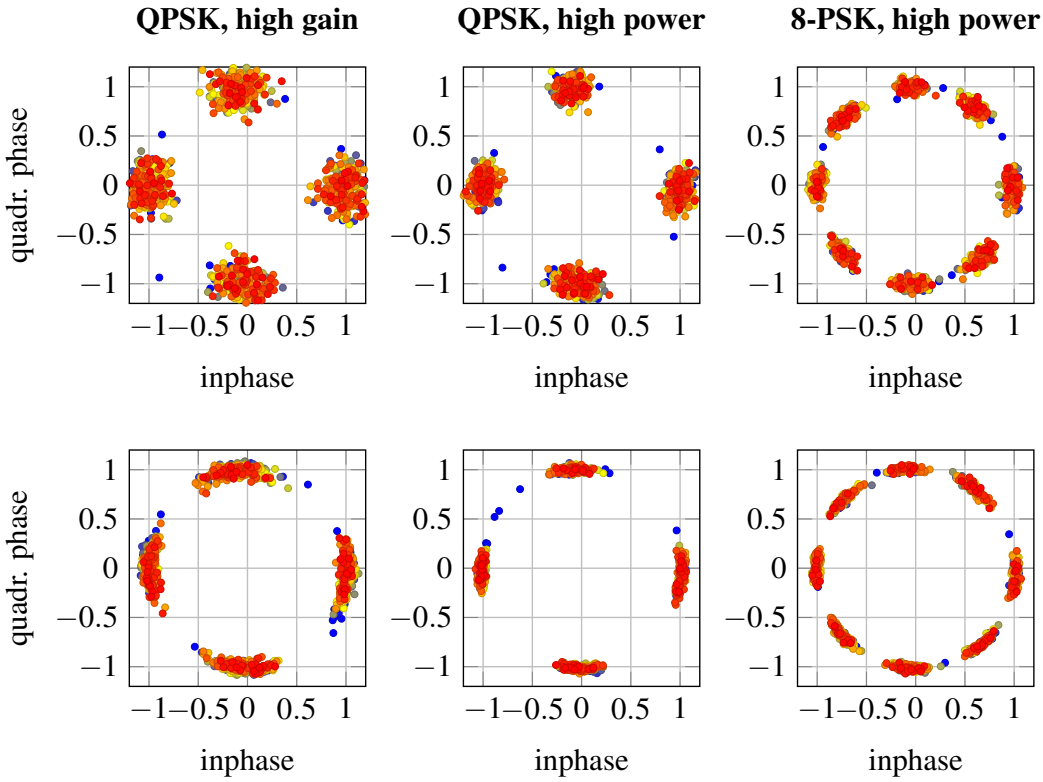

Figure 3.46: Constellation diagrams from measurements without SRO (top) and with SRO (bottom), for (A) QPSK with high gain (20 dB), (B) QPSK with medium gain (15 dB) and moderate compression, and (C) 8-PSK with medium gain (15 dB). The color map indicates the order of reception [7]♠, [26]♠ ©2019 IEEE

a frequency multiplier with a factor of 12. Thus, the baseband signal (blue) needed to be compressed in phase to be correctly mapped after multiplication (red; see top I/Q diagram in Figure 3.44 for an example with QPSK). A subsequent attenuator is used to configure different input magnitudes for the SRO. The SRO itself is contacted with wafer probes and connected to the setup by dielectric waveguide cables (1 m, insertion loss ∼10 dB each). It samples the input communication signal at the center of each symbol and amplifies it repetitively through positive feedback until the desired gain has been reached and the oscillation is turned off. The SRO output signal with one pulse per symbol is down-converted to an IF of 10 GHz [7]♠, [26]♠.

For further processing, the intermediate frequency signal is amplified and digitized. Afterwards, a numerical computation software is used to remove the IF by mixing to complex baseband. Filtering is done by complex conjugate convolution with a pulse shaping filter, in addition to the detection of sampling position and phase offset through correlation with a 1k symbol preamble. Subsequently, 10k symbols are sampled and analyzed for BER and EVM. Communication signals with 180 GHz center frequency and 1 GBaud pulse rate, and modulations of QPSK (2 Gbit/s) and 8-PSK (3 Gbit/s) have been regenerated with a regenerative gain of up to ∼20 dB. This corresponds to a highly efficient 2.9 pJ/bit for 8-PSK.

Figure 3.45 shows the measured IF signal of the SRO output before and after down-conversion to complex baseband. Both linear amplification as well as high output power with compression can be achieved. Figure 3.46 depicts the constellation diagrams before and after sampling the symbols with the SRO. They show very good phase linearity, even for high-order phase modulation. The dynamic range is sufficient for up to 20 dB gain with an EVM that is better than 16 dB. Since the gain can be easily controlled through pulse width over a wide range, gain can be traded off for EVM. This constitutes a notable advantage regarding complexity, system size and power consumption, especially at very high frequencies with very wideband signals since they can act as mm-wave variable gain amplifiers.

3.7 Waveguide Package and Wireless Link Experiment

To realize the regenerative gain capabilities of the SRO in practical use scenarios, it was beneficial to package the circuit into a standalone waveguide module, which achieves portability and flexibility of use. For this purpose, a mechanical construction that incorporates WR-5 waveguides for input and output was designed, and a test package was manufactured from brass. This bare module is shown as a split block in Figure 3.47 (only the lower half is shown). The chip was fixed between the waveguides using epoxy glue, and a printed circuit board was used to route the dc and switching signals. To couple the 180 GHz signals into and out of the chip, bondwire loops were used as E-field probes at the RF signal pads, as an alternative to expensive and impractical substrate probes [63]. Figure 3.48 shows the free-running output power of the waveguide-packaged SRO as a function of tuning voltage. The measured on-wafer output power as well as the calculated packaging loss are also shown. It can be seen that the loss due to the waveguide packaging is approximately 3 dB, with the variation at V_{tune} values below 1.6 V attributed to measurement uncertainty of the on-wafer power.

A wireless link measurement was thus set up with waveguide horn antennas. A 180-GHz transmitter module with IQ inputs and an integrated antenna was used to mix up generated

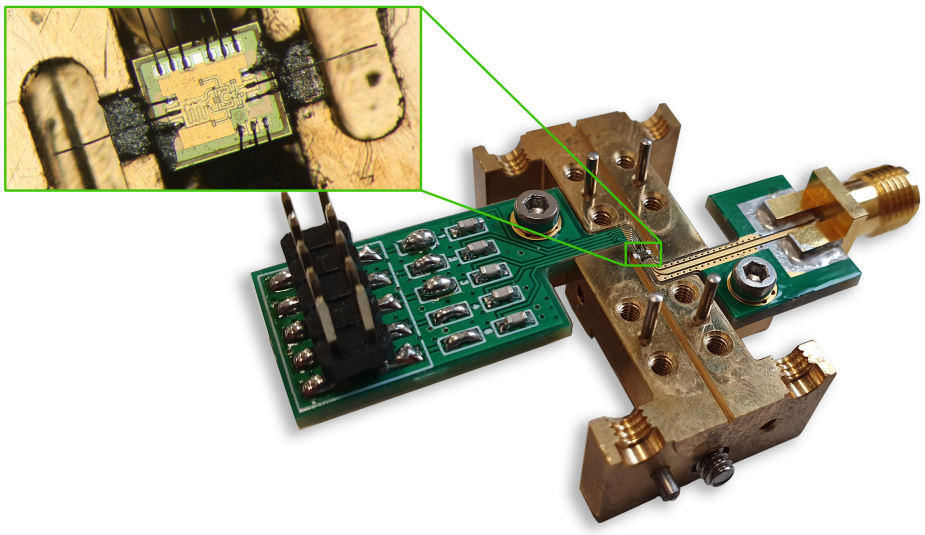

Figure 3.47: SRO waveguide module (lower part) with magnified chip transitions [7]♠ ©2020 IEEE

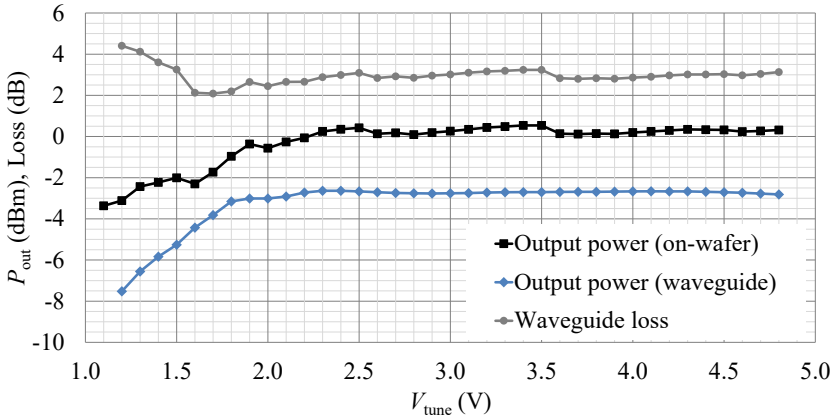

Figure 3.48: P_{out} as a function of V_{tune} from on-wafer and waveguide measurements. The waveguide packaging loss is also shown [7]♠ ©2020 IEEE

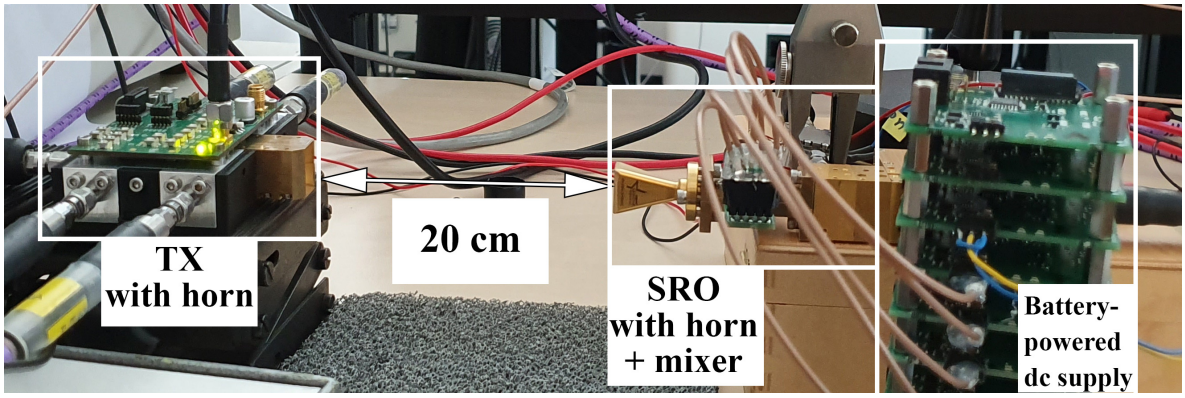

Figure 3.49: Wireless link setup photo with labeled blocks [7]♠ ©2020 IEEE

16QAM symbols and transmit them over the air. On the receiver side, the SRO module was used to recover the symbols, followed by a subharmonic mixer to mix down the pulses. The data was then digitized and processed similarly to section 3.3.3. A photo of the setup is shown in Figure 3.49 for a link range of 20 cm. A custom-design battery-powered dc supply module was used in order to stabilize the SRO center frequency and eliminate the low-frequency supply noise that could degrade the SNR.

Figure 3.50 shows the measured QAM-modulated IF pulses and the result of their down-conversion to complex-baseband. The constellation diagram is also presented, and shows successful recovery of 16QAM data at 4 GBaud, which corresponds to data transmission at 16 Gbit/s. This was the first demonstration of such a high data rate for a super-regenerative circuit, and still holds the world record at the time of writing.

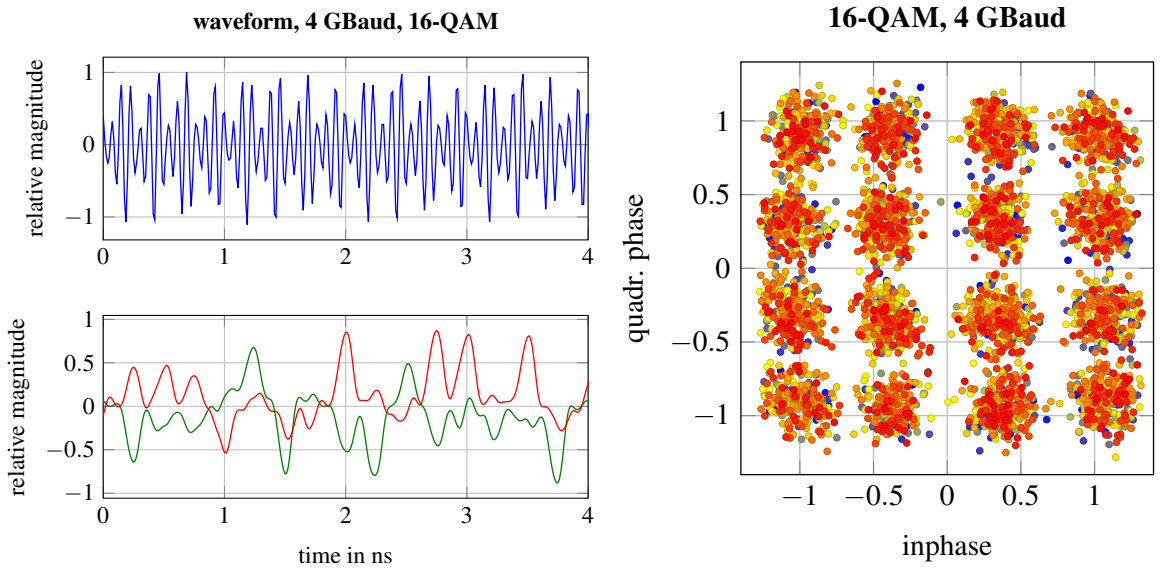

Figure 3.50: IF and complex baseband waveforms (left) and constellation diagram (right) for received 16QAM modulated pulses at 4 GBaud. The color map indicates the order of reception. EVM = -15.7 dB, BER = 8.5×10^{-3} [7]♠ ©2020 IEEE

4 Broadband High-Speed Circuits for Quench Waveform Shaping

The use of super-regenerative circuits for civil wireless communication applications presents additional system-level challenges, which have also been investigated in the course of this work. High data rates are increasingly sought after and are driving the push for more millimeter-wave and sub-terahertz circuits and systems. In order to achieve higher data rates in super-regenerative systems, there exist only two possibilities: (1) increase the symbol rate, or (2) the use of more complex modulation schemes. Since option (2) leads to high signal-to-noise ratio requirements, as well as higher system complexity, a modulation complexity up to 16-QAM was investigated as a proof of principle in this work. Therefore, the need for design techniques to increase the attainable symbol rate in a super-regenerative system arose.

As discussed in chapter 3, the SRO circuit is only able to regenerate modulated information during its start-up phase at the onset of oscillation. As the oscillation amplitude increases, the circuit sensitivity decreases until it reaches a steady-state amplitude. Thus, the circuit has to be quenched to receive the next symbol, as depicted in Figure 4.1. This defines the symbol period as the period from one quench event to the next, and the symbol rate is hence equal to the quench rate. Techniques to enable a high SRO quench rate at circuit level have been investigated and presented in chapter 3, such as by reducing the start-up time of the oscillator using custom load-pull methods. However, the slope of the quench signal also plays a role, as it superposes the start-up behavior of the oscillator. For example, a quench signal with a slow slope such as a sawtooth waveform would lead to a slower start-up than a rectangular waveform. Since multiple-GHz rectangular clock signals are not easily generated and routed in the lab or the system, sinusoidal RF quench signals are used instead. This creates the need for broadband high-speed circuits for quench waveform shaping, as shown in Figure 4.1.

Such circuits for SRO quench waveform shaping have to meet the following requirements:

- **Broadband** operation to allow flexible choice of quench rate up to high data rates. As an upper limit, in order to reach the very ambitious data rate of 100 Gbit/s with modulation of 16-QAM, a quench rate of 25 GHz would be required.

- **Low rise/fall times** to ensure fast turn-on and turn-off of the SRO and increase period efficiency.

- A **moderate to large output swing** to ensure noise immunity as well as full turn-ON and turn-OFF of the SRO, which prevents inter-symbol interference (ISI).
- **Low dc power consumption** to avoid degrading the power efficiency of the system.
- A **small area** for compact integration in a small footprint, which made peaking inductors unattractive.
- Optional: a **tunable duty cycle** allows an additional layer of flexibility to optimize the system performance at a fixed data rate e.g. to allow more time for oscillator start-up by increasing the duty cycle at high data rates, or to save dc power by reducing the SRO ON time at low data rates.

In the following, two circuits are presented, which have been designed using high-speed circuit techniques to fulfill the above requirements for quench waveform shaping. The first circuit in section 4.1 was based on a multi-stage limiting amplifier topology, thus requiring high gain to generate high-speed rectangular clock signals. The second circuit in section 4.2 is a high-speed Schmitt trigger, which uses positive feedback to reduce the gain requirements, hence achieving more power-efficient operation.

4.1 0.1-25 GHz Cherry-Hooper Limiting Amplifier

The high oscillation frequency of the SRO encourages the use of relatively high quench rates, which are desirable for the high symbol rates that they enable. Assuming the SRO can start up to steady-state amplitude within 10 oscillation periods, then a square-wave quench signal with one-twentieth of the frequency and 50% duty cycle can be employed. With mm-wave SROs, this frequency is already in the microwave range and is often not readily available in the system. Alternatively, a sinusoidal signal can be more easily synthesized and used for quenching, provided that it has sufficient amplitude. However, the relatively slow rise and fall times of the sine function then govern the startup and turnoff times of the oscillator, limiting the attainable speed. Thus, a limiting amplifier can be used in front of the quench signal source as shown in Figure 4.1 to speed up the switching transitions and achieve faster data rates [64]♠.

4.1.1 Circuit Design and Layout

A block diagram representing the cascaded stages of the limiting amplifier circuit is shown in Figure 4.2. An active balun input stage generates the differential components from a single-ended input. The limiting amplifier core follows, and is based on a modified Cherry-Hooper topology with embedded emitter followers in the feedback path. The output is buffered with two tapered emitter follower (EF) stages, as a compromise between speed and 50-Ω driving capability, which entails more power dissipation. The circuit uses three voltage supplies: V_{cc1} = 2.1 V for the balun, and V_{cc2}, V_{cc3} = 2.8 V for the limiting core and the output stage. All the stages are dc-coupled, and the total power consumption is 79 mW.

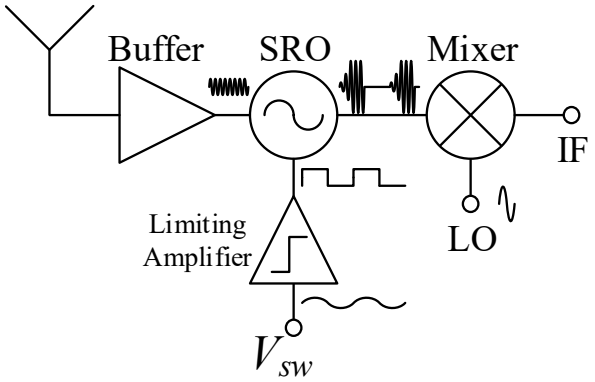

Figure 4.1: Super-regenerative receiver block diagram including a limiting amplifier for the generation of fast SRO quench signals [64]♠ ©2017 IEEE

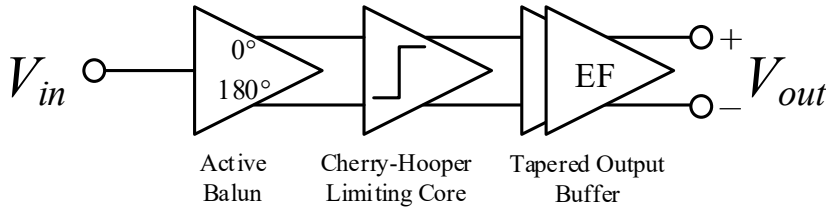

Figure 4.2: Stages of the limiting amplifier circuit [64]♠ ©2017 IEEE

Active Balun and Input Matching The design of the input stage was done using a topology that is similar to the one in [66]. An active approach is used to ensure uniform broadband operation down to low frequency. A schematic of the circuit is shown in Figure 4.3. Two differential pairs are designed in cascade with resistive loads R_{C1} and R_{C2}. The input of the first stage is tied to a shunt resistor R_{IN} for broadband input impedance matching to 50 Ω for connection to the lab instrumentation. The dc voltage at the bases of T_3 and T_4 is approximately V_{cc1} when the input is dc-blocked. The resistor R_E and capacitor C_E are used for emitter degeneration of the second differential pair, in order to increase the bandwidth of the input stage.

The single-ended input signal is converted to a differential signal at the output with broadband operation. Care was taken in the layout to ensure a good connection between the emitters of T_3 and T_4 with minimal parasitic resistance [66].

Cherry-Hooper Limiting Amplifier The Cherry-Hooper amplifier topology is commonly used in limiting amplifier design, especially for bipolar circuits, ever since it was initially proposed by E. M. Cherry and D. E. Hooper in 1963 [67]. It uses alternating series and shunt feedback to increase the gain bandwidth, and is capable of producing large output voltages. The embedding of emitter followers T_9 and T_{10}, as shown in Figure 4.4, further increases the speed by reducing the loading between stages. Furthermore, the addition of the load resistor R_2 has been introduced and shown to significantly increase the gain without deteriorating the bandwidth, when taking the output at the collectors of T_7 and T_8 [68]. This also reduces the collector-emitter voltage on those transistors, allowing the use of transistors with low breakdown voltages. However, this has the disadvantage that the output is no longer buffered,

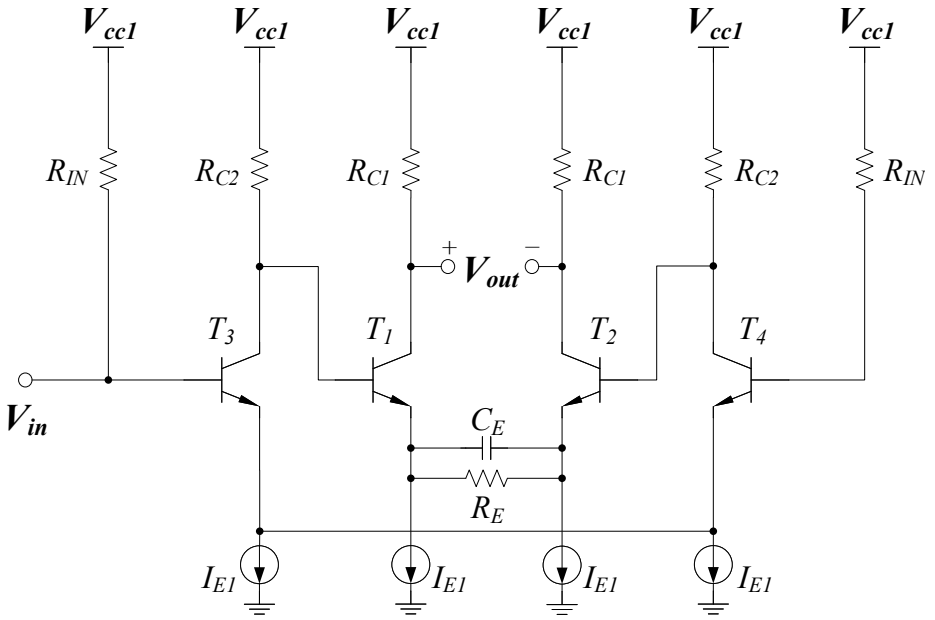

Figure 4.3: Schematic of the active balun input stage with 50 Ω input matching [64]♠ ©2017 IEEE

thus requiring an additional emitter follower stage, with its subsequent power consumption.

In this design, all transistors were sized as small as possible. The values for the resistors R_1, R_2 and R_f were chosen as a compromise between gain, bandwidth, and large-signal switching speed. It was shown in [69] that choosing a lower value of R_f/R_1 increases the 3-dB bandwidth, while a higher value increases the low-frequency gain. On the other hand, it can be seen from the simulated dc transfer characteristics in Figure 4.5 that a higher value of R_f/R_1 leads to more abrupt switching at low frequency. Simultaneously, choosing a higher value of R_2 leads to higher gain at the expense of higher voltage headroom. Therefore, in order to maintain a high value of gain as well as short rise and fall times up to 20 GHz, the resistor values were set proportionally for $R_f/R_1 = 2$.

Output Buffer As previously mentioned, the unbuffered output of the Cherry-Hooper amplifier requires an additional buffer stage to avoid the effects of loading from the subsequent stages. For the purpose of measuring the circuit using lab instrumentation, the capability to drive 50 Ω loads must also be provided. Thus, two tapered emitter follower stages are implemented in cascade as the output buffer, as shown in Figure 4.6. The tail bias current is scaled in proportion with the transistor size to deliver sufficient current at the output, leading to a factor 6 scaling of the emitter area and dc power consumption. The small transistor size at the input reduces the capacitive loading of the Cherry-Hooper amplifier output, leading to improved overall speed.

The last driving stage can be discarded in the system implementation in case the input impedance of the circuit at the quench node is large, resulting in a large reduction of dc power consumption of approximately 37 mW. Thus, the amplifier power consumption without the driving stage is almost cut down by half to 42 mW.

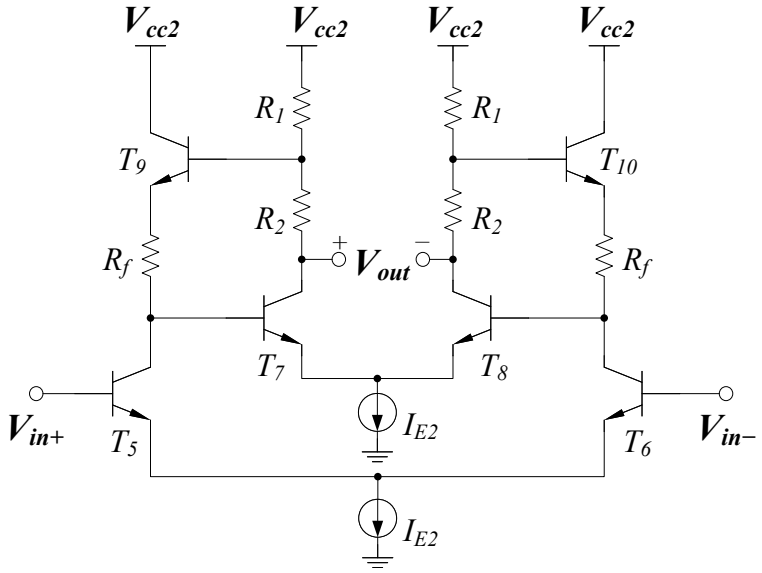

Figure 4.4: Schematic of the Cherry-Hooper limiting core with embedded emitter followers and additional load resistors [64]♠ ©2017 IEEE

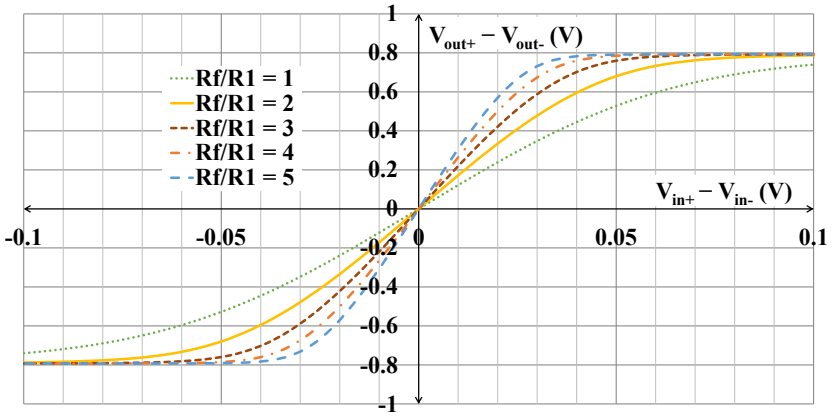

Figure 4.5: dc transfer characteristics of the Cherry-Hooper amplifier core from CAD simulations of the circuit [64]♠ ©2017 IEEE

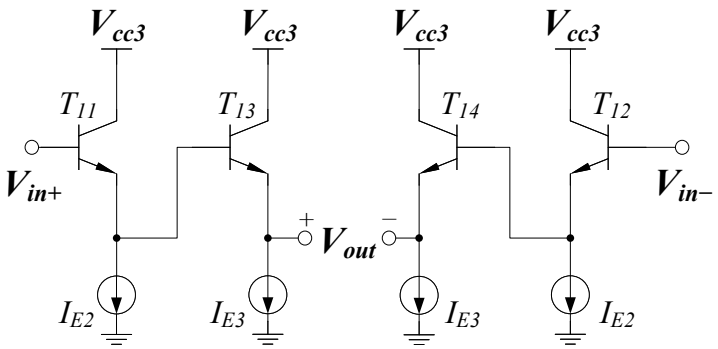

Figure 4.6: Schematic of the double emitter-follower output stage with tapered transistor sizes and bias currents [64]♠

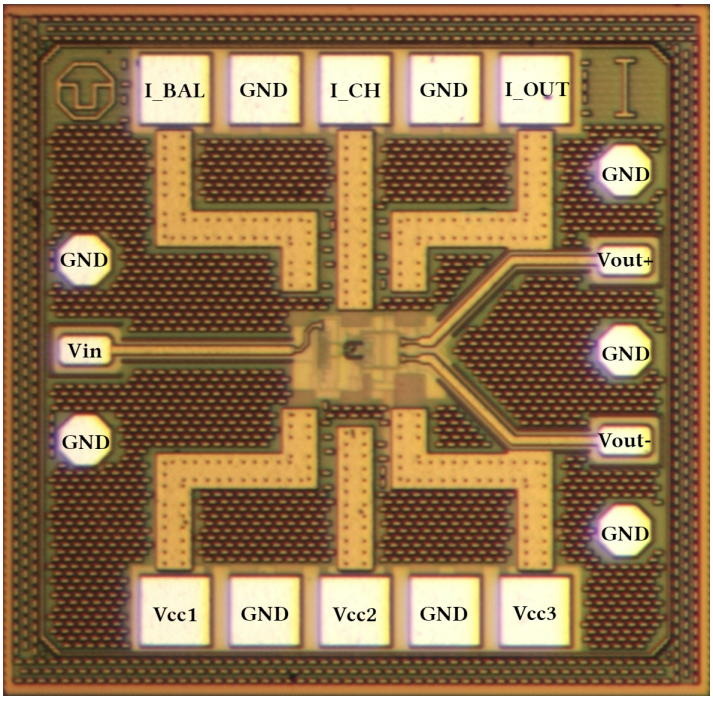

Figure 4.7: Micrograph of the limiting amplifier chip with all voltages and reference currents labeled. Total area = 760 μm $\times$ 740 μm, active area = 100 μm $\times$ 150 μm [64]♠ ©2017 IEEE

4.1.2 Experimental Results

To prove the concept, the circuit was fabricated in a 130m SiGe BiCMOS technology with f_T = 300 GHz [6]. A micrograph of the limiting amplifier chip is shown in Figure 4.7, including labels for all the required supply voltages and reference currents. As previously mentioned, the circuit has a single-ended input and a buffered differential output. Multilayer zero-Ohm transmission lines have been used for the distribution of the dc bias to the circuit, as they have been shown to possess several advantages over distribution networks based on decoupling capacitors [30], as previously discussed in section 3.3.2. Amongst these advantages are a very low impedance that only depends on the line dimensions, as well as high attenuation of ac signals, thus providing a reliable ac-ground where needed. All transmission lines used in the circuit were simulated using EM tools, and the parasitic resistances and capacitances of the transistor interconnects were considered using CAD extraction tools. Due to the compact inductor-less design, the circuit requires an active area of only 100 μm $\times$ 150 μm. However, for experimental testing in the lab, the total pad-limited chip area of 760 μm $\times$ 740 μm is required. The circuit was characterized by means of on-wafer probing, with V_{cc1} = 2.1 V and V_{cc2}, V_{cc3} = 2.8 V. The following sections describe the measurement setup and present the measurement results for S-parameters, 1-dB compression point, and large-signal oscilloscope and eye diagram measurements.

S-Parameters Due to the unbalanced-to-balanced nature of the circuit, a fairly complex 3-port calibration and measurement would be required for S-parameter characterization. Alternatively, the measurement is greatly simplified if one of the output ports is terminated in

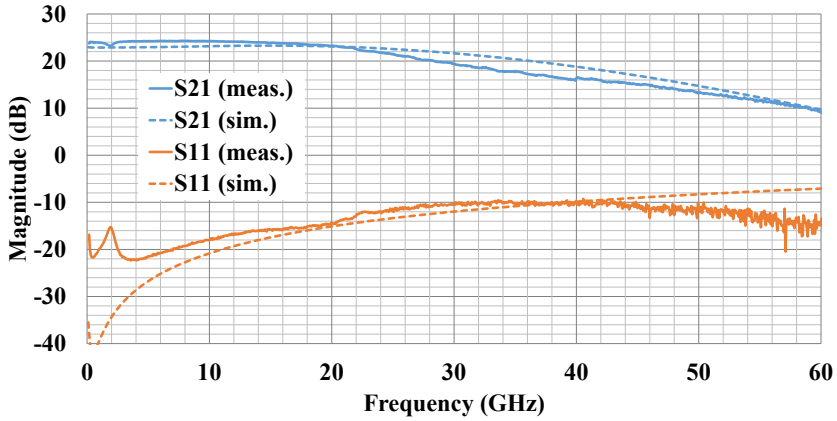

Figure 4.8: Measured and simulated S_{21} and S_{11} of the limiting amplifier circuit [64]♠ ©2017 IEEE

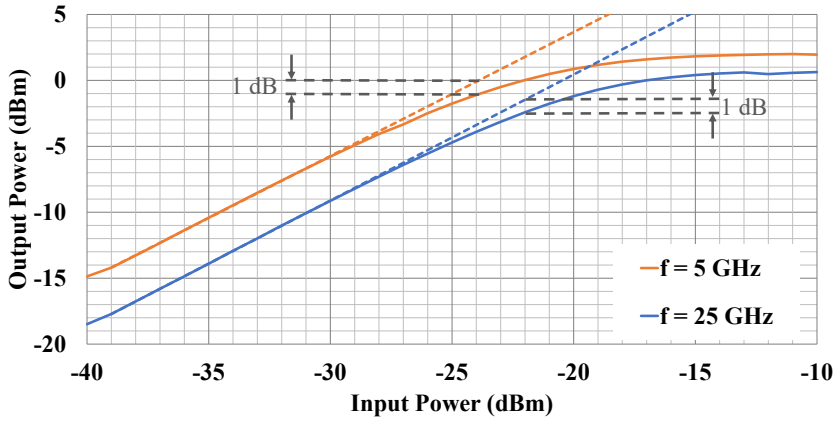

Figure 4.9: Measured output power against input power of the limiting amplifier at 5 GHz and 25 GHz [64]♠ ©2017 IEEE

a 50 Ω load, reducing the measurement to a simple 2-port setup. This is possible assuming the symmetry mismatch between the two ports is minimized. Thus, a GSGSG probe was used at the output with one of its signal pins terminated, and the calibration was performed on a 2-port GSG substrate. The measured and the simulated S_{21} and S_{11} of the circuit are shown in Figure 4.8. The circuit has a gain of 24.3 dB over a 3-dB bandwidth of 25 GHz. Thus, a differential gain of 27.3 dB can be deduced. The return loss is higher than 10 dB over the entire bandwidth, indicating good input matching. S_{22} is not considered as the circuit output is designed for large-signal operation.

1-dB Compression Point The 1-dB compression point is a good measure of amplifier linearity. It indicates the power level at which the circuit gain is compressed, resulting in a deviation of 1 dB from the hypothetical linear case. In the case of the limiting amplifier, however, the circuit is designed for nonlinear limiting of the output swing, thus lower values for the compression point are desired. Figure 4.9 shows the output power vs input power measurement of the circuit at 5 GHz and 25 GHz. The input-referred 1-dB compression points are calculated as -24 dBm and -22 dBm, respectively.

Frequency (GHz)	V_{p-p} **(mV)**	**Rise Time (ps)** 20%–80%	**Fall Time (ps)** 20%–80%
5	599	9.8	8.1
10	576	10.0	6.7
20	508	5.6	6.0
25	511	5.8	6.1

Table 4.1: Limiting amplifier single-output oscilloscope measurements at different frequencies [64]♠ ©2017 IEEE

Oscilloscope Measurements For the large-signal time-domain measurements, a two-channel sampling oscilloscope was used to measure the output of the circuit, with an RF signal source at the input. The source was simultaneously used to trigger the oscilloscope for precision time-base measurements, using a power divider. The circuit outputs were connected to the oscilloscope's probes using approximately equal-length cables. An automated skew-adjust function was used to further align the differential waveforms. Figure 4.10 (a,c,e,g) show the resulting waveforms for different frequencies. On the right, Figure 4.10 (b,d,f,h) show the mathematical difference of the waveforms, with a peak-to-peak differential swing of up to 1.2 V.

The main results are summarized in Table 4.1 for one of the outputs. The results were taken for one of the outputs to avoid any inaccuracies resulting from arbitrary phase alignment of the output waveforms in the differential waveform. It can be seen from the table that the output swing is lower at higher frequency, resulting in a difference of 90 mV between 5 and 20 GHz. The rise and fall times also decrease with frequency, but not proportionally to the reduction in switch period, resulting in an overall worsening of switching behavior. Nonetheless, the 20%–80% rise time of 5.6 ps at 20 GHz is considered very fast, as it roughly corresponds to one oscillation period of the SRO at 180 GHz.

Eye Diagrams The eye diagram is a useful method of presenting the large-signal behavior of an amplifier in the communication path. It provides a visual representation of the amplitude noise and time jitter which could lead to intersymbol interference and degrade the bit-error rate. The eye diagram is thus presented here to facilitate the comparison with other limiting amplifiers. A pseudo-random bit sequence (PRBS) generator was used for the input, and the eye diagrams were obtained from the oscilloscope connected to a single output. Figure 4.11 shows the eye diagrams for data rates up to 50 Gbit/s. The eye amplitude is greater than 500 mV and the eye opening is almost 400 mV at 50 Gbit/s. These values would roughly be doubled for full differential output driving.

4.1.3 Conclusion

This section presented a limiting amplifier, fabricated in a 130 nm SiGe BiCMOS technology with f_T = 300 GHz [6], for the generation of high-speed SRO quench waveforms. The limiting core is based on a modified differential Cherry-Hooper topology with embedded emitter followers. The circuit generates a balanced output from an unbalanced input, and achieves a

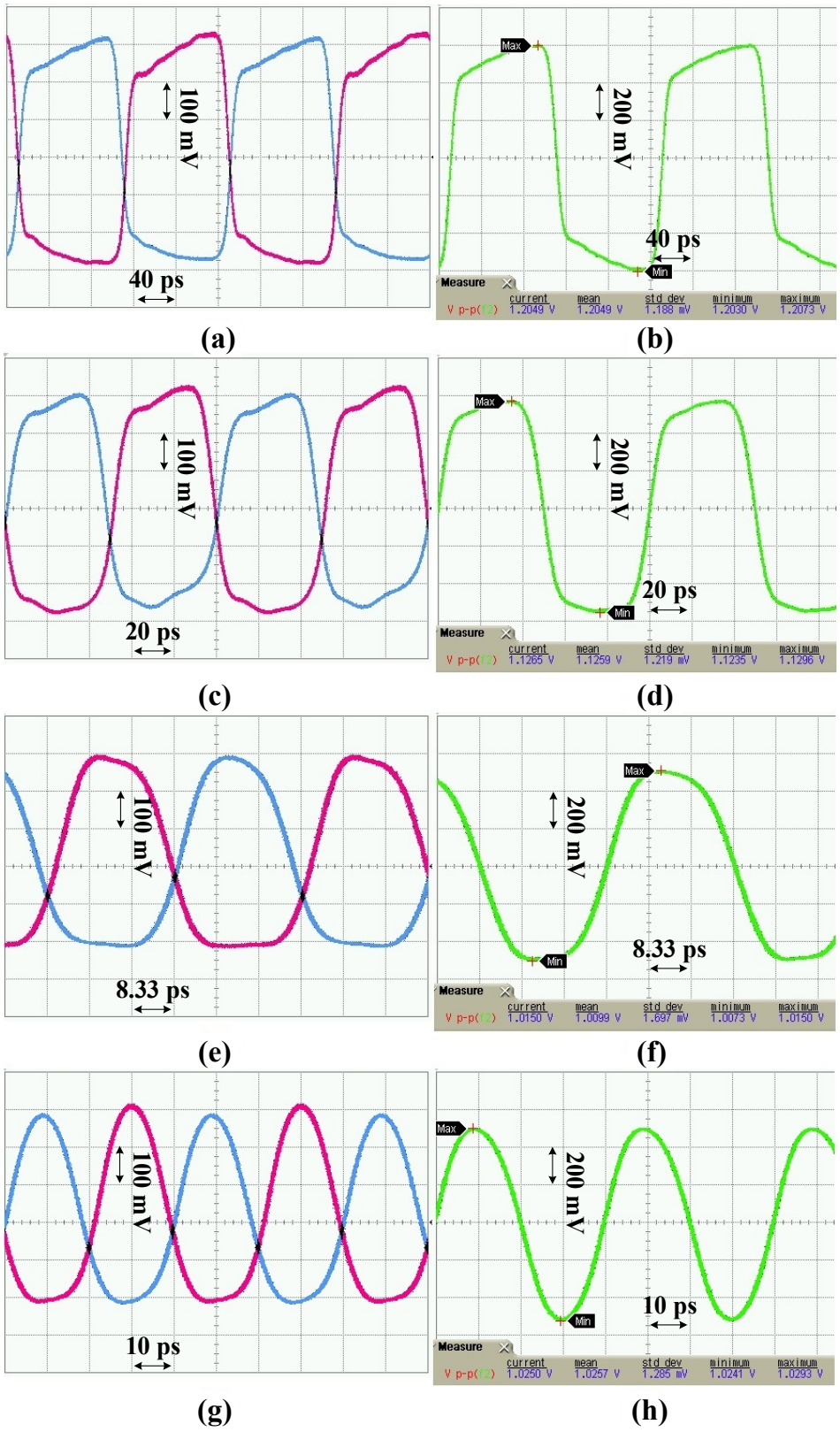

Figure 4.10: Measured time-domain output waveforms for input frequencies of (a,b) 5 GHz, (c,d) 10 GHz, (e,f) 20 GHz, and (g,h) 25 GHz. The left diagrams show the two single-ended outputs separately whereas the right diagrams show the corresponding mathematical difference of the waveforms [64]♠ ©2017 IEEE

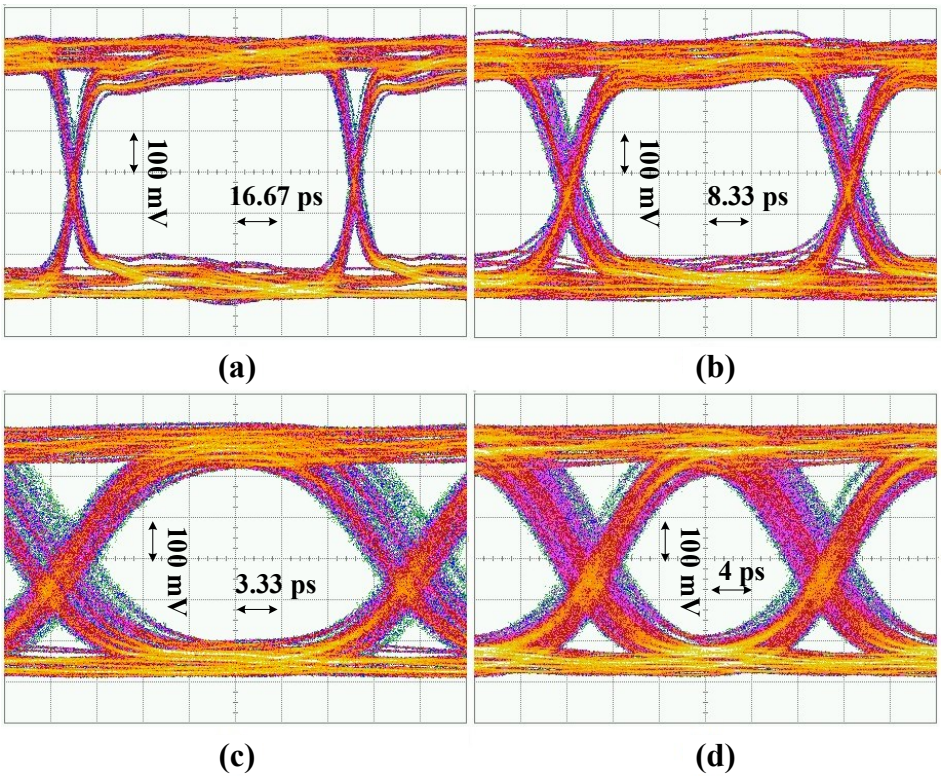

Figure 4.11: Measured eye diagrams at data rates of (a) 10 Gbit/s, (b) 20 Gbit/s, (c) 40 Gbit/s, and (d) 50 Gbit/s [64]♠ ©2017 IEEE

differential gain of 27.3 dB over a 25-GHz bandwidth. Table 4.2 presents a comparison of this work with other SiGe HBT limiting amplifiers in the literature. It can be seen that the amplifier in this work operates with competitively low power consumption, despite the high differential peak-to-peak output swing of 1.2 V. It has a relatively moderate gain bandwidth product, which trades against the goal of obtaining low rise and fall times. Thus, it achieves a very good 20%–80% rise time of 5.6 ps at 20 GHz, and a corresponding fall time of 6.0 ps. The design circumvents the need for large peaking inductors, resulting in a cost-efficient active area of 100 μm $\times$ 150 μm.

	[68]	[69]	[70]	[71]	[72]	**This work [64]♠**
SiGe Node	350 nm	350 nm	200 nm	200 nm	800 nm	**130 nm**
f_T (GHz)	47	47	120	120	80	**300**
Gain (dB)	60.0	19.7	42.0	36.0	54.0	**27.3**
BW (GHz)	15.0	13.7	24.0	26.0	9.0	**25**
P_{DC} (mW)	1100	34	550	390	364	**79**
V_{p-p} (mV)	2000	220	370	600	600	**1200**
Area (mm^2)	3.12	0.49	0.68	1.43	0.26	**0.56**

Table 4.2: Comparison of published SiGe limiting amplifiers [64]♠ ©2017 IEEE

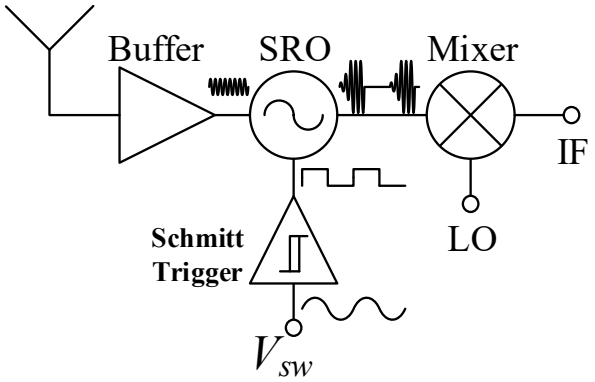

Figure 4.12: Block diagram showing the role of the proposed Schmitt trigger in a super-regenerative receiver frontend [65]♠ ©2019 IEEE

4.2 0.1-18 GHz Schmitt Trigger with Tunable Duty Cycle

It is desirable to maximize the operation frequency and minimize the rise and fall times of the quench signal in order to reach high data rates. Additionally, the ability to directly control the pulse width is needed to set the operation mode and adjust the gain and power consumption of the receiver frontend. Figure 4.12 shows a depiction of the receiver frontend, including the quench waveforms generation using the proposed Schmitt trigger [65]♠.

The Schmitt trigger is a bistable circuit that produces a binary logic output depending on the input waveform's instantaneous level [73]. It has thus been widely used as a decision and pulse-shaping circuit for communication and signal processing applications. This is aided by its hysteresis property, which leads to noise immunity and less transition errors. Fed with a periodic input, it also provides a simple approach to produce rectangular ac signals with sharp transition edges at different frequencies. By tuning its threshold levels, the duty cycle of the output waveform can be directly controlled without changing the frequency. This in turn leads to additional pulse–width modulation capabilities. The input signal V_{sw} therefore becomes a simple sine wave and can be easily generated and routed; either externally or by using a local oscillator.

4.2.1 Schmitt Trigger Analysis

For the purpose of generating high-speed quench signals with variable duty cycle, two alternatives are presented in Figure 4.13 for comparison. The first alternative in (a) comprises a differential pair with single-ended input/output. The second approach, depicted in (b), utilizes a conventional Schmitt trigger circuit consisting of an emitter-coupled transistor pair with tail current source I_0, and a resistor connected between the output of T_3 and the input of T_4. This circuit, however, uses a current source I_D to tune the feedback, instead of a voltage divider as in the typical case. Thus, it can be implemented as a voltage-dependent current

Acknowledgment: *This is to acknowledge that section 4.2 contains the results of a joint work on RF Schmitt trigger, for which my student at the time and later colleague at Technische Universität Dresden, Yu Zhu, was a major contributor. He was also a co-author of [65]♠, in which this work was first published. I would like to express my gratitude for his contributions.*

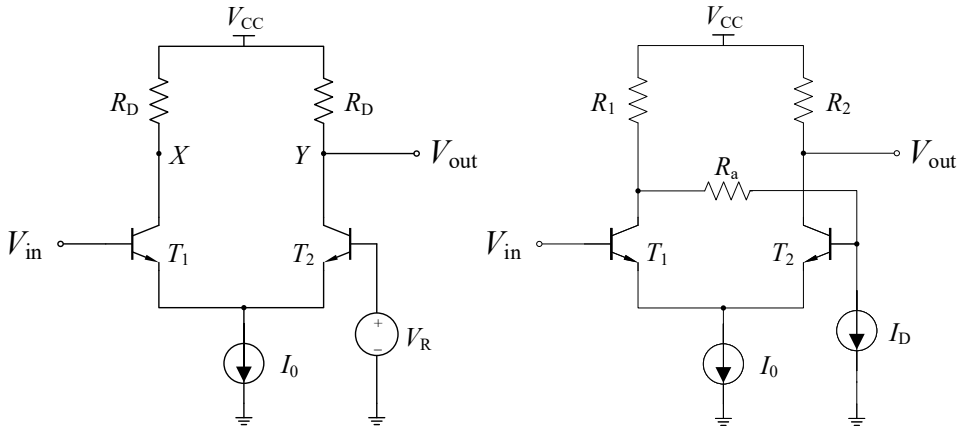

Figure 4.13: Circuit schematics of (a) differential pair with single-ended input and output, and (b) a Schmitt trigger circuit [65]♠ ©2019 IEEE

source using a MOS transistor.

The output of the differential pair in Figure 4.13 (a), follows the difference between V_{in} and V_R with its known large-signal characteristic. The Schmitt trigger in (b), on the other hand, reacts to the input when it crosses one of two thresholds. As the input level crosses the high threshold V_{HT}, transistor T_3 conducts current and its collector voltage falls. This in turn lowers the base potential of T_4, thus less current flows through it, further increasing the collector current of T_3 due to the fixed tail current. This positive feedback effect continues until the output of T_4 is high. Similarly, as the input level falls below V_{LT}, the output quickly falls to the low state. The difference between the two threshold levels is the hysteresis width.

For a reasonable comparison between the two circuits, the design parameters were chosen for similar dc bias conditions and power consumption. A circuit-level CAD simulation was run for the dc transfer characteristics, and the results are shown in Figure 4.14. It is seen that the transition edges of the Schmitt trigger are significantly sharper, thus leading to a fast amplitude-limiting behavior without the need for high small-signal gain. On the other hand, the differential pair offers the possibility of taking the output differentially between nodes X and Y. This leads to higher output voltage swing, but only if the following stage is differential.

An analysis of the circuit to determine the threshold voltage levels was performed, similar to [74] and [75], but including I_D, and the levels were found as follows

$$V_{HT} = V_{CC} - R_1 I_0 \frac{1}{x+1} - I_D(R_a + R_1) - V_T \ln x \tag{4.1}$$

$$V_{LT} = V_{CC} - R_1 I_0 \frac{x}{x+1} - I_D(R_a + R_1) + V_T \ln x \tag{4.2}$$

where

$$x = \frac{1}{2}\left(\frac{R_1 I_0}{V_T} - 2 + \sqrt{\left(2 - \frac{R_1 I_0}{V_T}\right)^2 - 4}\right) \tag{4.3}$$

The threshold levels predicted by (4.1)–(4.3) for the previous circuit are 2.15 V and 1.87 V, thus fitting with its simulation results with a difference of less than 5% each. This difference

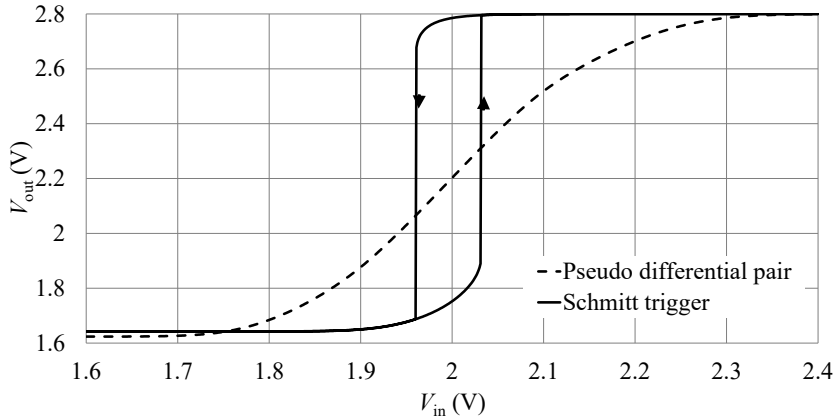

Figure 4.14: Large-signal characteristics of a differential pair vs a Schmitt trigger for the same bias and load conditions [65]♠ ©2019 IEEE

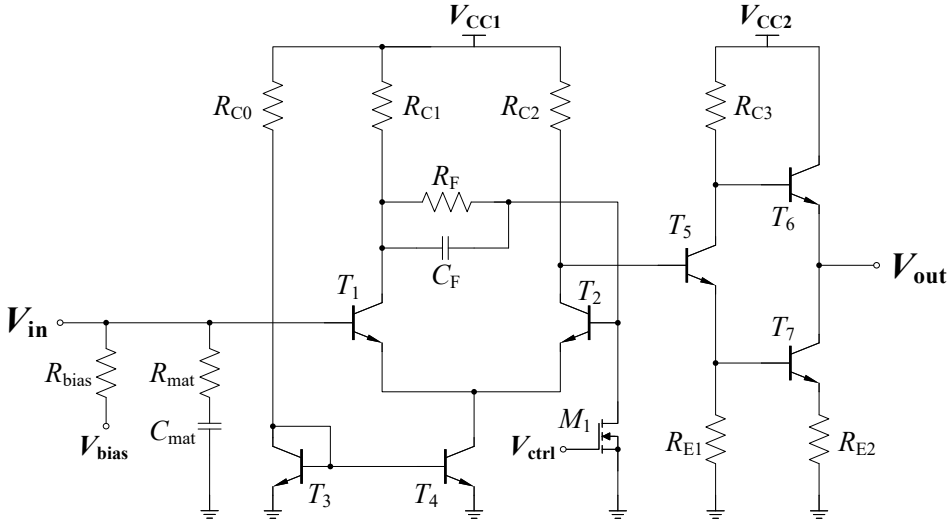

Figure 4.15: Circuit schematic of the Schmitt trigger and Totem-Pole output buffer [65]♠ ©2019 IEEE

can be attributed to the assumption that the base currents are negligible. The threshold levels are independent of R_2. Therefore, R_1 and I_D can be chosen for the required thresholds, whereas the product I_0R_2 sets the output voltage swing.

4.2.2 Circuit Design and Layout

The Schmitt trigger circuit was implemented using HBT transistors in a 130 nm SiGe BiCMOS process, with f_T and f_{max} up to 300 and 500 GHz, respectively [6]. A schematic of the Schmitt trigger circuit is shown in Figure 4.15 and includes all circuit component values. Transistors T_1 and T_2 make up the trigger, along with the current mirror T_3 and T_4.

The hysteresis width is designed as small as 60 mV in order to have better control over the duty cycle. Noise elimination is not required for this application as V_{in} is assumed to have low amplitude noise. The capacitor C_F bypasses RF at higher frequencies, forming a high-pass filter with a cutoff frequency of approximately 500 MHz and improving the rise and fall times

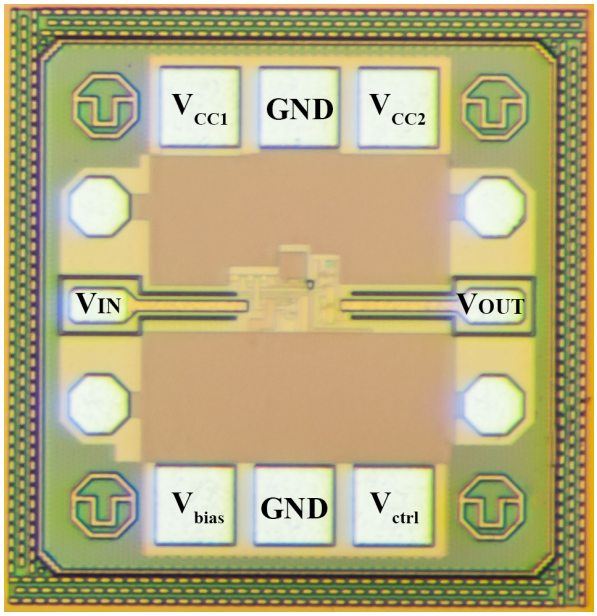

Figure 4.16: Micrograph of the Schmitt trigger IC including labels for pad signals. Total pad-limited area = 520 × 540 μm^2, active area = 120 × 90 μm^2 [65]♠ ©2019 IEEE

at higher switching speeds.

The nMOS transistor M_1 implements the tunable current source I_D. By tuning the gate voltage of M_1 through V_{ctrl}, its drain current is varied, thus shifting the high and low thresholds by the same amount. This varies the time between crossings for the periodically changing V_{in}, and consequently tunes the duty cycle of the output, thus enabling continuous pulse width modulation.

During layout, the circuit's interconnect lengths were minimized, so that they are much shorter than the wavelength at the highest frequency of operation. Parasitic RC extraction could then be performed in the post-layout simulation stage to predict the high-speed circuit's performance. The short interconnects and the inductor-free circuit topology led to the compact implementation, requiring an active area of only 0.02 mm^2. A micrograph of the fabricated IC is shown in Figure 4.16 with all signal pads respectively labeled. The test chip is limited by the size of the pads and requires a total area of 0.28 mm^2.

The dc routing network is implemented as a mesh of zero-Ohm lines, which are highly capacitive transmission lines with a very low characteristic impedance approaching 0 Ω [35], as previously discussed in section 3.3.2. These provide reliable dc connections with ac short circuit behavior, in addition to shielding the circuit from any high frequency spurs in the supply. Most importantly, they enable good modeling of the dc distribution network, since their impedance is largely dependent on the line dimensions. Thus, transmission line theory can be used to predict their performance with different load impedances. The compact layout in addition to the use of small transistors with high f_T/f_{max} lead to the reduction of device and interconnect parasitics, which could limit the operating speed of the circuit. The use of a high-pass filter between the circuit stages improves the switching performance at higher frequencies, and the broadband 50-ohm matching network ensures broadband operation over the desired frequency range.

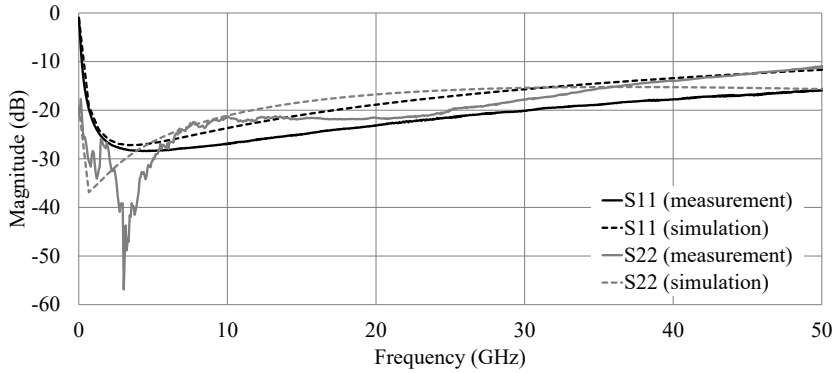

Figure 4.17: Simulated and measured return loss for input (S_{11}) and output (S_{22}) ports [65]♠ ©2019 IEEE

4.2.3 Experimental Results

To study the feasibility of the proposed research concepts, the circuit was characterized on-chip using a wafer prober with 67 GHz RF probes for V_{bias} = 2 V and V_{ctrl} = 1.7 V. The S-parameters were measured using a 67 GHz network analyzer to characterize the input and output matching. The measurement results are shown in Figure 4.17 vs post-layout simulations. The return loss is better than 20 dB in the operation frequency range, and a good fit between measurement and simulation results is observed.

For the time-domain measurements of the waveforms, an RF signal generator is used to provide the input sinusoidal signal at multiple frequencies with 0 dBm power level. A 70 GHz sampling oscilloscope is used to capture the output waveforms as well as the eye diagrams. Additionally, a 50 Gbit/s pseudo-random bit sequence generator with a bit pattern length of $2^7 - 1$ is used to generate the input sequences for the eye diagram measurements. It is noted that no post-processing has been done on the signals before presentation. Thus, the losses of the measurement setup (e.g. cable losses, probe tips) are not de-embedded and cause deterioration of the measured output.

Figure 4.18 shows the measured output waveforms at different input frequencies f_s, when V_{ctrl} was set for a duty cycle D = 50%. The frequency of the output signals was measured and consistently came out identical to f_s. It is noted that the waveforms appear to have a rectangular shape at lower frequencies of 1 GHz and below. The transitions are sharp, implying relatively low rise and fall times. As the frequency increases, the circuit's parasitic capacitance introduces poles that slow down the switching transitions. At 18 GHz, the waveform starts to resemble a sine wave. Table 4.3 summarizes the peak-to-peak voltage swing V_{p-p} and the 20%–80% rise and fall times at each measured frequency. The circuit produces waveforms with V_{p-p} of 300–400 mV, and rise/fall times as low as 10 and 13 ps at 10 GHz.

Figure 4.19 presents the circuit's duty cycle tuning range and the corresponding tuning voltages at 1 GHz and 5 GHz. At 1 GHz, the duty cycle could be tuned continuously in a wide range from 13% to 85%. At 5 GHz, the tuning range was slightly smaller, measuring 22% to 80%. This is due to the relatively slower trigger transitions, thus the output does not reach its full swing at the extreme duty cycles. It is worth noting that the observed level shifting does not come from the circuit itself, but is a result of the averaging done by the dc blocking capacitor in the measurement setup. The average value of the signal after the capacitor is a function of the duty cycle, thus shifts as the duty cycle is tuned. It is also noted that the duty

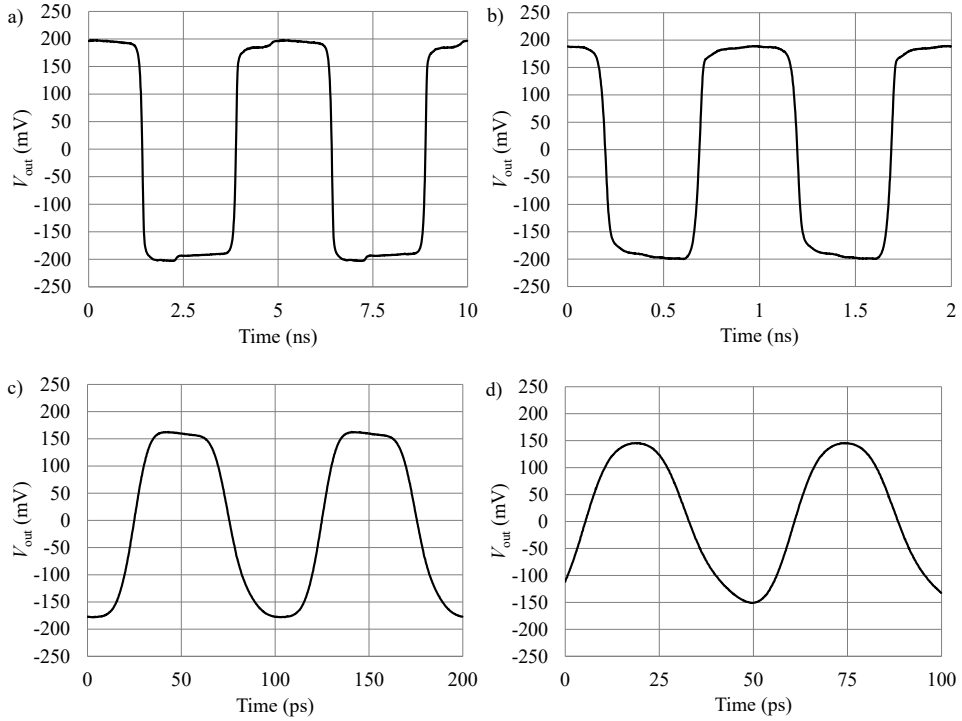

Figure 4.18: Measured output waveforms at a) f_s = 200 MHz, b) f_s = 1 GHz, c) f_s = 10 GHz, and d) f_s = 18 GHz. Tuning voltage V_{ctrl} was set for D = 50% [65]♠ ©2019 IEEE

Frequency (GHz)	V_{p-p} **(mV)**	**Rise Time (ps)** 20%–80%	**Fall Time (ps)** 20%–80%
0.2	407	76	76
1	393	32	37
5	359	13	16
10	346	10	13
18	301	8	10

Table 4.3: Schmitt trigger oscilloscope measurements at different frequencies [65]♠ ©2019 IEEE

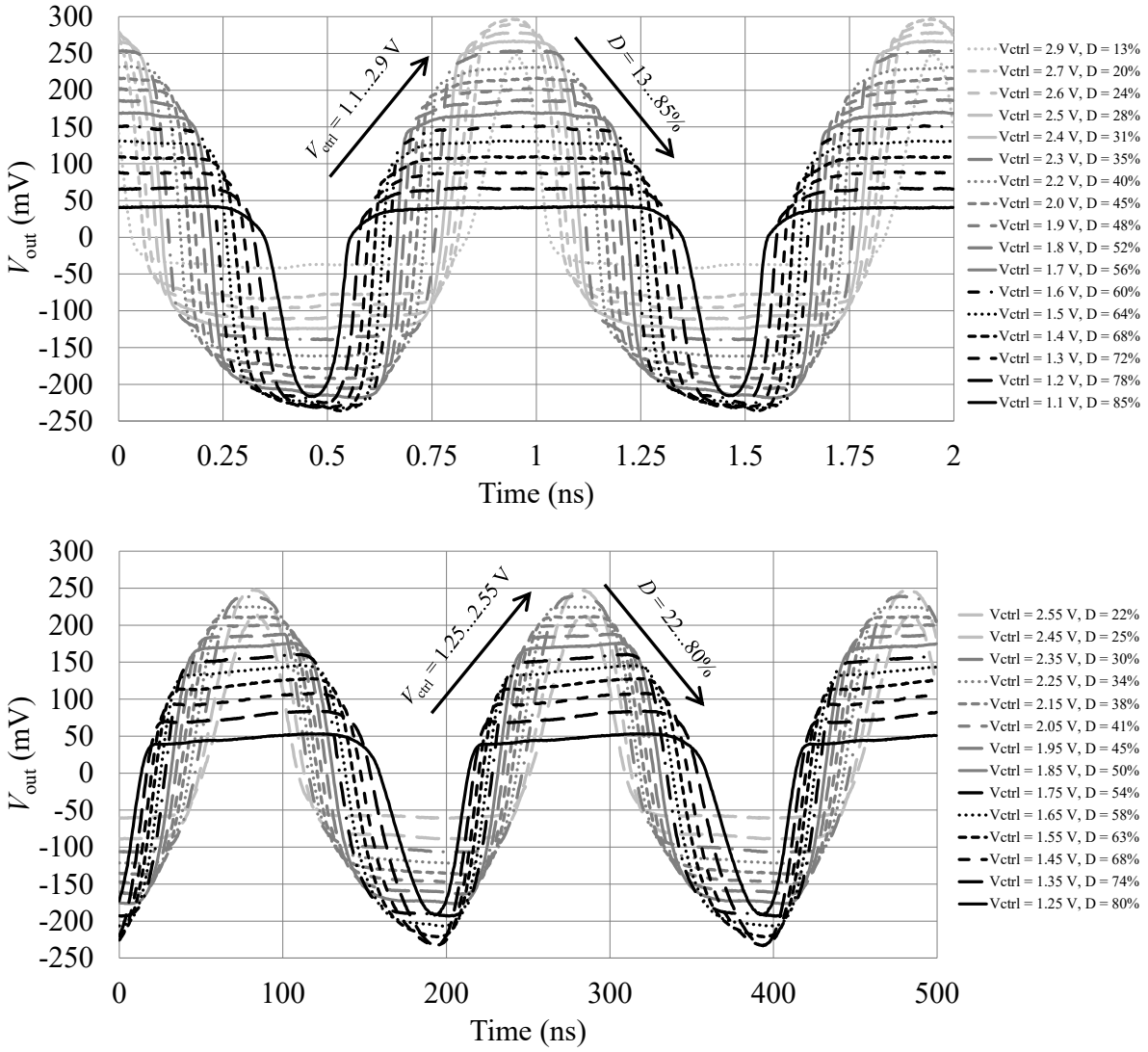

Figure 4.19: Measured output waveforms at f_s = 1 GHz (top) for different tuning voltages V_{ctrl} = 1.1–2.9 V, showing duty cycles D = 13–85%, and at f_s = 5 GHz (bottom) for V_{ctrl} = 1.25–2.55 V, showing duty cycles D = 22–80% [65]♠ ©2019 IEEE

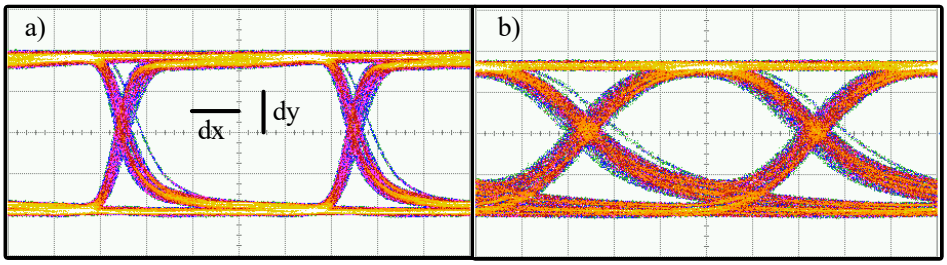

Figure 4.20: Measured eye diagrams at a) 10 Gbit/s, dx = 20 ps, dy = 100 mV, and b) 40 Gbit/s, dx = 5 ps, dy = 100 mV [65]♠ ©2019 IEEE

	[76]	[77]	[78]	**This work [65]♠**
f_s (GHz)	0.133	1	0.5	**0.1–18**
Technology	130 nm CMOS	40 nm CMOS	180 nm CMOS	**130 nm BiCMOS**
P_{DC} (mW)	4.2	N.A.	N.A.	**24.6**
V_{p-p} (V)	3.3	1	1.8	**0.4**
Area (mm^2)	0.0002*	Sim.	Sim.	**0.28**
Tunable duty cycle	no	no	yes	**yes**

Table 4.4: Comparison of published RF Schmitt triggers above 100 MHz [65]♠ ©2019 IEEE

cycle is inversely proportional to the tuning voltage due to the inverting nature of the output buffer.

Measurements of the eye diagram were also performed at 10 Gbit/s and 40 Gbit/s, in order to characterize the circuit's noise and jitter performance, and are shown in Figure 4.20. They show an open eye up to a very high data rate despite the slowing of the trigger transitions, indicating that the circuit does not introduce any significant amplitude noise. The r.m.s. jitter was measured and found to be between 1–2 ps for both waveforms.

The main results are summarized in Table 4.4 and compared against other RF Schmitt triggers in the literature. It can be seen that this work has by far the highest performance by maximum frequency of operation, and the first fabricated circuit relying on this topology for high-speed analog applications.

5 Super-Regeneration in 60-GHz FMCW Automotive Radar

In a smart interconnected world, sensing becomes a crucial component for the autonomy of smart devices if their dependence on human supervision should be reduced. Sensing their surrounding environment, devices can make decisions that enable them to function in more complex scenarios, beyond the simple use cases of motion-based door access and lighting control. One type of sensing is spatial awareness, which opens the door to many different applications, based on the localization of one device or the ranging between two or more different devices. This can be achieved by integrating FMCW radar transceivers, which have become ubiquitous in applications such as automotive driver assistance systems, due to several notable advantages. FMCW radars are resilient to interference, simplify the baseband signal processing, and most importantly, they can be integrated into a small silicon form factor, which lends itself to high volume production and brings the cost down.

Taking into consideration the actual increase of connected devices by a few billions each year, the energy efficiency of these devices begins to play a very significant role. The power consumption of each sensor must be kept as low as possible, hence highly efficient solutions must be explored. Here, too, super-regeneration could offer advantages of very large and energy-efficient gains. Due to their phase-sampling capabilities, super-regenerative circuits have been used as active reflectors for FMCW radar systems, regenerating and re-transmitting weak frequency chirp signals with much larger amplitude [37]. Additionally, since these SRO circuits make use of instability for their operation, they also overcome the stability concerns of active reflectors that are based on conventional amplifiers. This enables to increase the range and the number of sensors in FMCW radar systems, whereas the power consumption does not scale accordingly, leading to highly efficient and long-lasting battery operation.

5.1 FMCW Radar Autonomous Parking System

As a proof of concept for the use of SROs in FMCW radar, the following system and application scenarios were conceptualized. Within the range of functions that are possible in autonomous vehicles, it is desirable to achieve automated and autonomous car parking. This would minimize the number of parking-related accidents, as well as reduce the time and

energy waste that is incurred in traffic while searching for a parking place. For this purpose, a radar system would be built to determine the absolute position of vehicles in real time and with high precision. Typical use cases of that system would be in scenarios where existing positioning systems, such as GPS, either are not present, or are not sufficiently accurate. This is for example the case in indoor scenarios such as tunnels and parking garages, which are usually covered with thick attenuating walls, and where an accuracy of a few centimeters would be required for automated parking. In order to achieve this high ranging accuracy, a small spatial resolution is required, which in FMCW radar is inversely proportional to the chirp bandwidth. For the case of a reflective radar system with rectangular windowing, the range resolution ΔR was found to be [4]

$$\Delta R \approx 0.66 \cdot \frac{c}{B_{fm}}, \tag{5.1}$$

where c is the speed of light and B_{fm} is the linear chirp bandwidth. Therefore, a large unlicensed bandwidth would be required to achieve the resolution requirements. For a range resolution of 3 cm, a chirp bandwidth of 6.6 GHz would be required. Hence, the ISM band around 60 GHz was chosen for this study, since it offers up to 9 GHz of free unlicensed spectrum for industrial, scientific, and medical applications.

In order to solve the problem of autonomous car parking, a grid-based system would be implemented in a closed environment, such as a parking garage. Proximity sensors would indicate if a parking spot is free or occupied, and the parking spot would be defined as one grid cell, or a combination of cells. To accurately navigate the car to the parking spot, a number of solutions could be utilized. A camera-based system would allow the car to see and navigate its surroundings, but its location accuracy is limited, and it would not work in low light situations. Lidar technologies could be used, but the reliability is limited in bad weather e.g. foggy situations, and they cannot resolve situations where direct line of sight is obstructed e.g. due to walls or other parked cars. Microwave sensing using FMCW radar is able to overcome the previous limitations, and was therefore chosen for this work.

For the design of the FMCW radar system, several alternatives were also considered. A primary radar system could be used, in which the car contains a two-way radar transceiver, which enables it to sense its environment using reflections from the surroundings. However, in order to provide complete information for navigation to the parking spot, a complex imaging radar with many transmitters and receivers would be required. Additionally, it would be difficult to extract local coordinate information from such a system. Therefore, a secondary system was preferred, with active nodes inserted at locations with known coordinates in the infrastructure. Using triangulation from the closest infrastructure transceivers, the car location could be accurately determined.

The implementation of the fixed active nodes would conventionally be done as full one-way radar transceivers, with complete RF frontends consisting of transmitter and receiver blocks, and full baseband chains. This approach would typically need high power consumption and high complexity, as well as challenging clock synchronization requirements. In this work, an alternative based on SRO active reflectors is proposed, which greatly simplifies the implementation and enhances the performance. A diagram depicting the SRO based implementation is shown in Figure 5.1. The pros and cons of this SRO active reflector approach are compared against the conventional one-way radar in Table 5.1.

Although the focus of this work is placed on the novel use of mm-wave super-regenerative

	One-way radar	**SRO active reflectors**
Pros	• Large range if power amplifier is included • High precision due to large available bandwidth	• Ultra-efficient operation leading to low power consumption and long battery life • Medium range depending on SRO output power, high regenerative gain • Low component cost • Relaxed clock synchronization requirements
Cons	• High complexity and power consumption • High component cost • Challenging clock synchronization and phase noise requirements • High baseband processing requirements, low refresh rate	• High SRO bandwidth requirements • Range is limited by minimum SRO detectable signal and maximum output power

Table 5.1: Pros and cons of conventional one-way radar and SRO active reflectors for autonomous car parking system

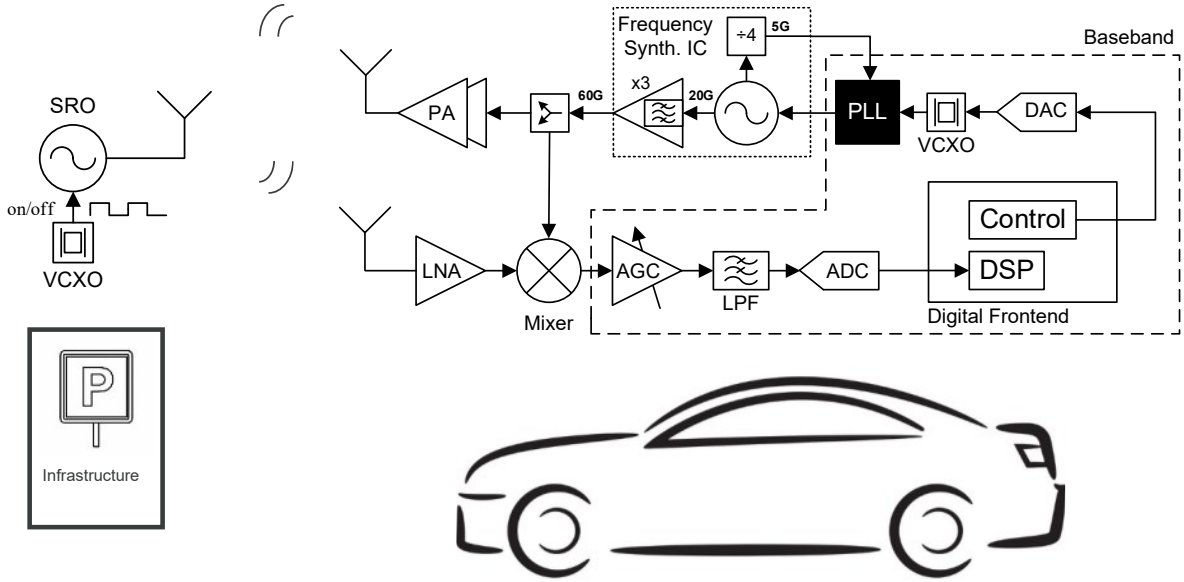

Figure 5.1: System concept of FMCW radar autonomous car parking using active reflector SROs, including the block diagrams of car transceiver and infrastructure reflector

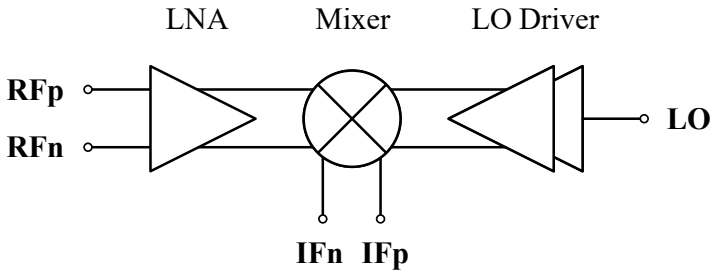

Figure 5.2: 60 GHz receiver frontend block diagram [79]♠ ©2021 IEEE

reflectors in automotive radar, additional 60-GHz receiver blocks have been investigated to realize the system, and are detailed in the following section.

5.2 A 60-GHz FMCW Receiver Frontend With Gain-Linearity Tuning

In this work, the design and measurement of a 60-GHz receiver circuit for down-conversion of incoming radar chirps is presented. A low-noise amplifier circuit and active mixing ensure good conversion gain and noise performance of the receiver. Linearization of the mixer transconductance stage results in a tunable linearity gain-tradeoff capability, which allows better linearity operation when needed [79]♠.

Figure 5.2 shows the block diagram of the proposed 60-GHz receiver frontend. It consists of a differential low-noise amplifier (LNA), a Gilbert-cell mixer, and an amplifier for the local oscillator (LO) signal, which also acts as a balun to simplify the generation of the LO signal.

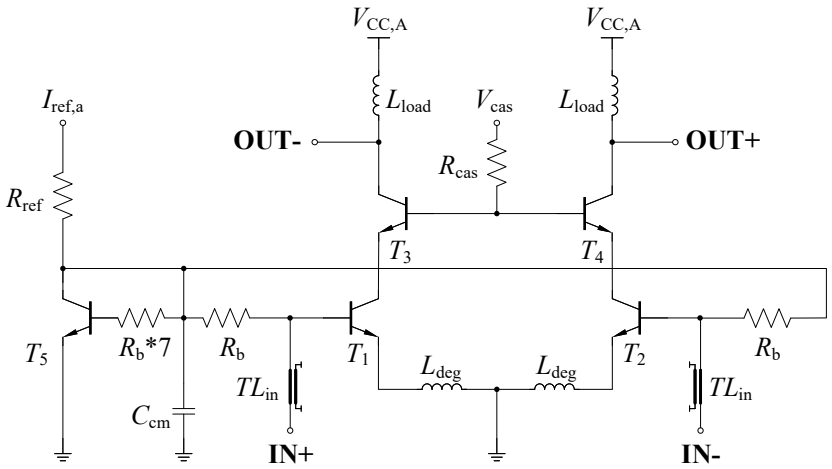

Figure 5.3: 60-GHz LNA circuit schematic [79]♠ ©2021 IEEE

5.2.1 Circuit Design and Layout

60-GHz Low-Noise Amplifier

A pseudo-differential cascode topology was chosen for the LNA design due to its typically large gain and bandwidth at a moderately low noise figure (NF). The LNA circuit schematic is shown in Figure 5.3. The input transistors $T_{1,2}$ were sized such that the real part of the optimum noise impedance $R_{s,opt}$ is equal to 50 Ω [81]. Additionally, the input impedance is tuned by using inductive degeneration L_{deg} at the emitters of $T_{1,2}$.

A transmission line TL_{in} is added at the bases to match the imaginary part, thus achieving a broadband input match around 60 GHz that minimizes the NF. Care is taken during layout to reduce the base shunt inductance and increase capacitance, to ensure stability. The load inductor L_{load} is implemented as a differential center-tapped inductor and used to feed the supply V_{CCA}. Current biasing is done using $I_{ref,a}$ through T_5 to set the optimum current density through the transistors $I_{c,opt}$, which yields the minimum NF.

60-GHz Gilbert Mixer

Unlike CMOS transistors, the low 1/f noise in bipolar transistors enables the use of active mixer stages, such as the Gilbert cell, down to low IF frequencies for e.g. FMCW radar applications. This results in notable advantages for the receiver gain and NF, and relaxes the requirements for LO signal power. A double-balanced architecture is helpful for reducing undesired common-mode and second-order signals. For these reasons, an active mixer based on the Gilbert architecture was designed as shown in Figure 5.4.

Linearity is an important parameter in FMCW receivers, as it mainly determines the dynamic range of the radar. In many cases, the overall receiver linearity is determined by the mixer linearity, which is mainly limited by the linearity of the input transconductance stage for a Gilbert mixer. Therefore, a combination of two linearization techniques was designed to enhance the mixer linearity. Resistive emitter degeneration was applied to the RF input transistors $T_{1,2}$ for a broadband linear response.

Additionally, a diode linearizer circuit $D_{1,2}$ was designed, which increases the base current to $T_{1,2}$ at higher input drive levels without dropping the base-emitter voltage V_{BE}, thus reducing

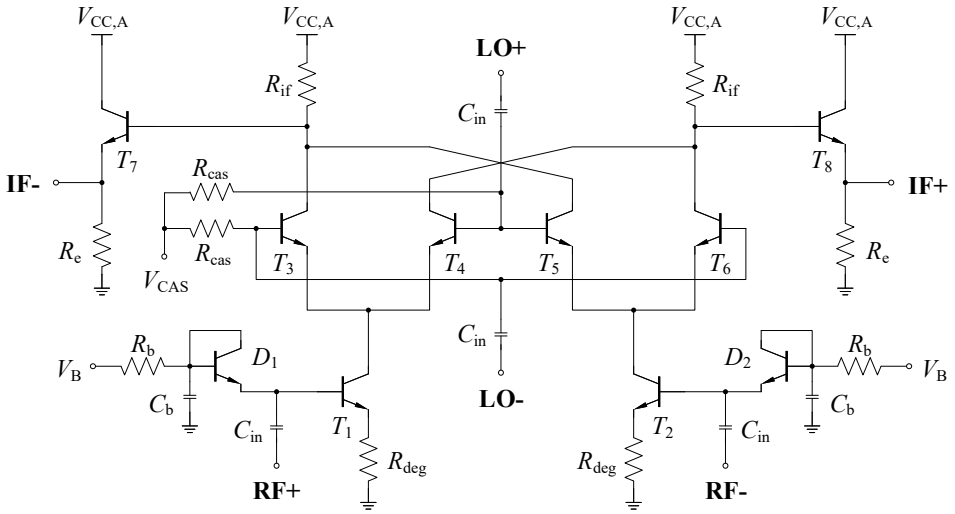

Figure 5.4: 60-GHz Gilbert mixer circuit schematic [79]♠ ©2021 IEEE

the early gain compression that is typically seen with conventional bias circuits [82].

Figure 5.5 shows schematic diagrams for a common-emitter transconductance stage in a Gilbert mixer with conventional bias, and the proposed linearized design, with the diode linearizer bias circuit and emitter degeneration. The simulation results of the two mixer circuits are presented in Figure 5.5, showing how V_{BE} is reduced for the conventional design above an input power of 15 dBm, whereas the linearized design achieves a peaking of V_{BE} at high input powers, leading to an increase in linearity.

60-GHz LO Driver

In order to simplify the generation and routing of LO signals, a two-stage amplifier/balun was designed as shown in Figure 5.6. The amplifier stages consist of differential pairs with an inductive load and a small resistor to limit the output at the required LO signal power. The unbalanced input is converted to a balanced output through the common-mode rejection of the emitter-coupled current source.

5.2.2 Experimental Results

To prove the proposed concepts, the receiver circuit was fabricated in a 130-nm BiCMOS HBT technology with f_T and f_{max} up to 300 and 500 GHz, respectively [6]. A micrograph of the receiver chip is shown in Figure 5.7 with pad labels and a circuit area of 1.1 mm^2. The circuit was measured on-wafer by using a vector network analyzer, which was reconfigured to measure conversion gain of a frequency-translating block. Power sensors were used to characterize the losses of the measurement setup and calibrate the results. NF was measured using a spectrum analyzer and two noise sources for different frequency ranges.

The measurement results are shown against frequency in Figure 5.8, as well as the corresponding simulation results for comparison. The receiver has a peak conversion gain of 34 dB for that linearity setting, and the gain is above 18 dB for the presented frequency range of 45-70 GHz. A minimum single-side-band NF (NF_{SSB}) of 6 dB is achieved at the center of the band. This is dominated by the differential LNA stage that precedes the mixer. The

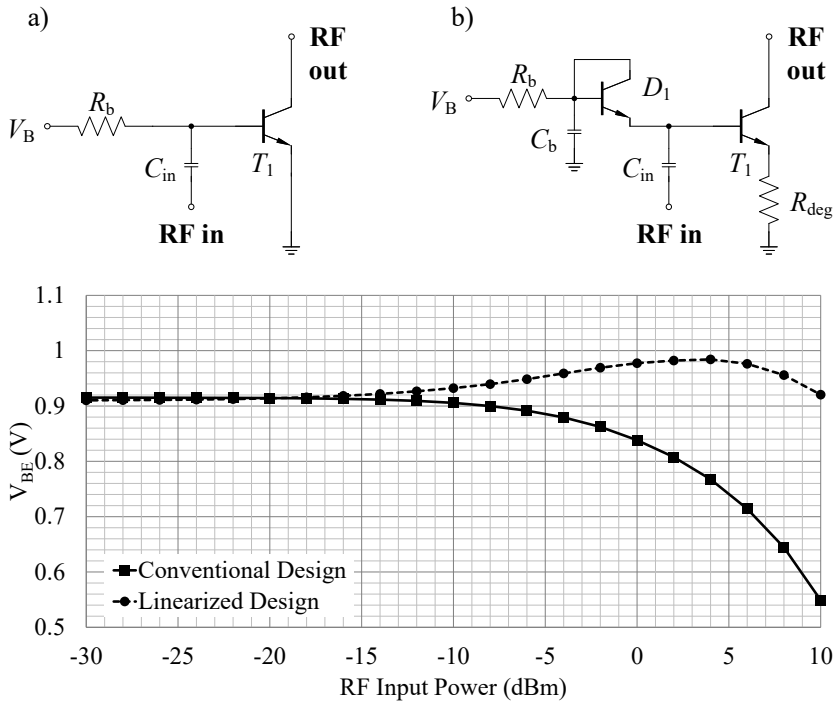

Figure 5.5: Circuit representation of a Gilbert mixer transconductance stage with (a) conventional bias circuit and (b) linearized design. Shown below is the simulated base-emitter voltage V_{BE} of the transistors against the RF input power for both designs [79]♠ ©2021 IEEE

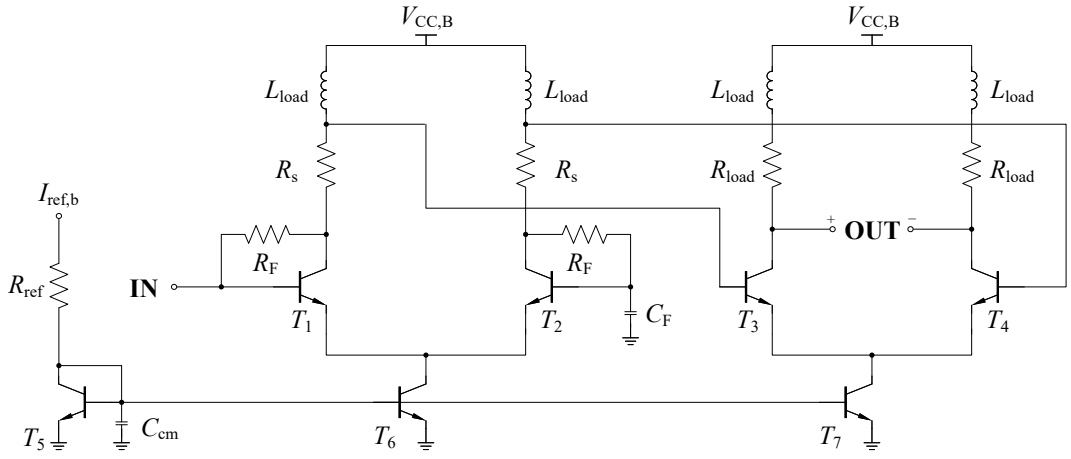

Figure 5.6: 60-GHz LO driver amplifier/balun circuit schematic [79]♠ ©2021 IEEE

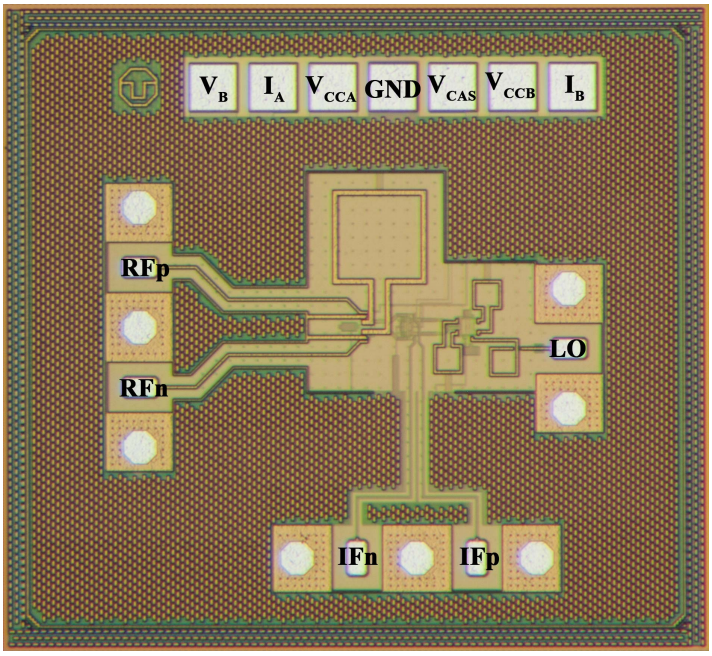

Figure 5.7: 60-GHz receiver circuit micrograph (area = 1100 × 1000 μm^2) [79]♠ ©2021 IEEE

input return loss is shown at the LO and RF ports. The differential RF input return loss shows a broadband response close to 10 dB, whereas the LO input return loss is narrowband and centered at 61.5 GHz. Signal loss due to reflections at the LO input is not critical and is compensated by the gain of the LO driver stage. Linearity measurements were carried out and the results are shown against simulations in Figure 5.9. It can be seen that tuning V_B leads to gain-linearity tuning, as the gain is reduced whereas a peaking shape occurs at higher input power, due to the effect depicted in Figure 5.5. The input-referred 1-dB compression points IP_{1dB} for V_B = 1.5, 1.7 and 1.9 V were calculated as -30, -34.4, and -41.9 dBm, respectively. The gain for these settings was 30.2, 33.9, and 35.9 dB, respectively. Therefore, 11.9 dB of input-referred linearity can be traded off for only 5.7 dB of gain.

Figure 5.10 shows the measured and simulated conversion gain against signal power at the LO driver input pad. The results are presented for three V_B bias settings, in order to show the effect of gain-linearity tuning on LO power requirements. It is possible to operate the receiver with LO power starting from -25 dBm due to the integrated driver, which simplifies system design considerations with regards to LO signal amplification and routing.

Table 5.2 shows a comparison of radar receiver ICs operating in or around the 60 GHz ISM frequency band. The proposed receiver has the highest conversion gain, except for one other work that includes a 3-stage LNA and a baseband amplifier. This work has the best measured noise figure, and a moderate dc power consumption due to the integrated LO driver amplifiers. Among the papers that report a built-in gain-linearity tuning capability, it has the best gain-linearity tradeoff ratio.

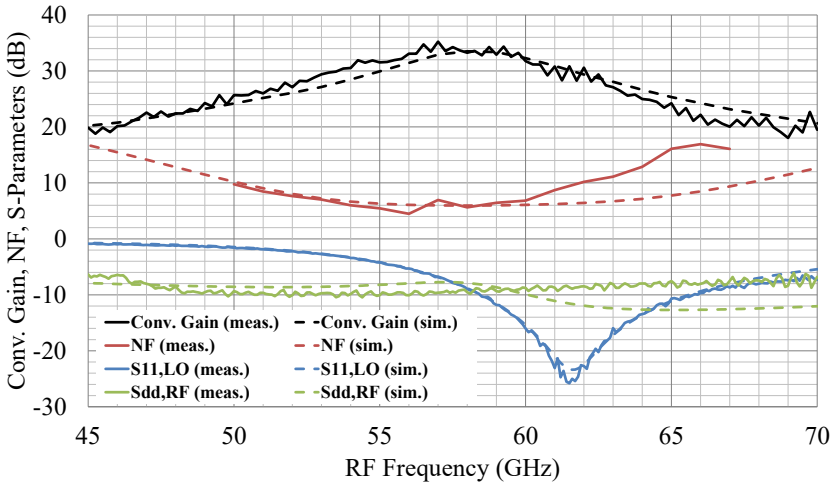

Figure 5.8: Measurement and simulation results for conversion gain for f_{IF} = 10 MHz, NF, and return loss at LO and RF ports [79]♠ ©2021 IEEE

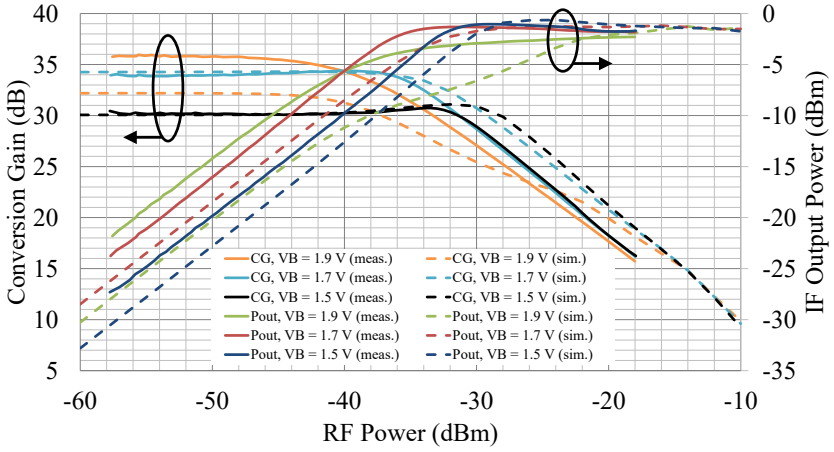

Figure 5.9: Linearity of conversion gain and IF output power against RF input power for f_{LO} = 57 GHz, P_{LO} = 15 dBm and f_{IF} = 10 MHz [79]♠ ©2021 IEEE

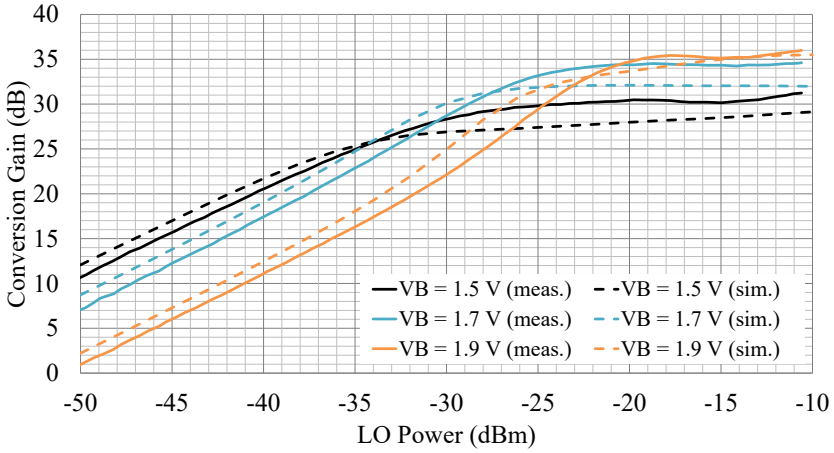

Figure 5.10: Conversion gain against signal power at LO driver input for f_{LO} = 57 GHz and f_{IF} = 10 MHz [79]♠ ©2021 IEEE

Ref.	**Technology**	**Frequency (GHz)**	**Supply (V)**	**Conversion Gain (dB)**	NF_{SSB} **(dB)**	IP_{1dB} **(dBm)**	P_{DC} **(mW)**	**Area (mm^2)**	**Gain-Linearity Tuning**
[83]	28 nm CMOS	57–64	0.9	17.2–19.3	10.5–11.2	-13	40	0.2$^{(1)}$	No
[84]	350 nm SiGe	57–64	3.3	19	9.5	-8.5	66	20.3$^{(2)}$	No
[85]	130 nm SiGe	53–65	3.3	23$^{(3)}$	5.5$^{(3)}$	-26$^{(3)}$	76$^{(3)}$	1.7$^{(2)}$	No
[86]	180 nm SiGe	57–64	3.3	13–23$^{(3)}$	5$^{(3)}$	-13 – -7$^{(3)}$	957$^{(2)}$	6.7$^{(2)}$	Yes
[87]	130 nm SiGe	58–64	3.3	14.8	7.8$^{(3)}$	-18.2$^{(3)}$	520$^{(2)}$	1.0$^{(2)}$	No
[88]	45 nm SOI CMOS	64–70	1.2	10$^{(3)}$	–	–	42$^{(2)}$	1.6$^{(2)}$	No
[89]	180 nm SiGe:C	57–64	3.3	35–70$^{(4)}$	7.0	-85 – -62$^{(4)}$	284	1.7	Yes
This work [79]♠	**130 nm SiGe**	**57–66**	**2.0, 3.0**	**30–36**	**6.0**	**-42 – -30**	**195**	**1.1**	**Yes**

$^{(1)}$ not including pads $^{(2)}$ full transceiver $^{(3)}$ simulation results $^{(4)}$ including baseband amplifier

Table 5.2: Performance summary and comparison of 60-GHz radar receiver ICs [79]♠ ©2021 IEEE

5.3 A 60-GHz Super-Regenerative Oscillator with 80 dB Gain

The availability of wide unallocated bandwidth in millimeter-wave frequency bands has led to numerous new system applications. The ISM band around 60 GHz is attractive since it offers a license-free bandwidth with several GHz of bandwidth, which can be used to implement high-resolution radars for civil automotive applications. At millimeter-wave frequencies, there are several basic research challenges, such as how to handle the high signal attenuation and the low transistor gains, which limit the possible range of the radar [80]♠.

Super-regenerative amplification enables a power-efficient low-complexity solution to expand the range of FMCW radar systems using active reflector tags. The principle utilizes positive feedback to re-transmit a weak incident chirp signal with very large gain [14]. The phase of the input signal is sampled during the sensitive initial stage of the oscillator start-up. The output signal grows exponentially while retaining the phase information, until it reaches full amplitude. The gain is then periodically quenched in order to return the system to the initial phase-sensitive mode. Among the research challenges is the achievement of high sensitivity at such high frequencies.

This paper presents a basic scientific research study of an SRO in 130 nm SiGe BiCMOS technology. It is designed as an active reflector for future 60 GHz FMCW civil automotive secondary radars. The next sections describe the circuit concept. As a proof of concept, a chip is realized and experimentally characterized, followed by a comparison with the state of the art.

5.3.1 Circuit Design and Layout

Super-Regenerative Oscillator

The SRO circuit is based on a cross-coupled oscillator network consisting of the bipolar transistors $T_{5,6}$ and the coupling capacitors C_k, as shown in the schematic in Figure 5.11. The transistors are sized for output powers larger than 0 dBm. Accordingly, the bias current is set by the current mirror $T_{1,2}$, and the diodes $T_{3,4}$ provide an offset voltage to enable a reference voltage close to V_{CC}. MOS varactors M_{var} are used as the frequency tuning elements through the tuning voltage V_{tune}. To increase the output power and the gain, a load transformation network is implemented at the output, which consists of the high-impedance transmission lines TL_{ad}, TL_{sh}, and TL_{sr}, as well as the capacitor C_{sr}. A Marchand balun is included to facilitate the connection with the antenna feed line, and the node OSC is used as input during oscillator start-up as well as output when the amplitude is large.

Periodic quenching is done at the SW node through the MOS transistor M_1. The large pull-down resistor R_{pd} enables a free-running oscillator mode when no signal is fed at SW. The MOS capacitance M_{cap} is connected in parallel to reduce the slope of quenching, which has been found to improve the sensitivity of the SRO [28]. This in turn increases the maximum gain of the circuit. The capacitance value is optimized and the layout is carefully done to reduce the inductive part. The antenna diode D_{ant} is connected to the substrate and protects M_1 gate from charge effects during fabrication.

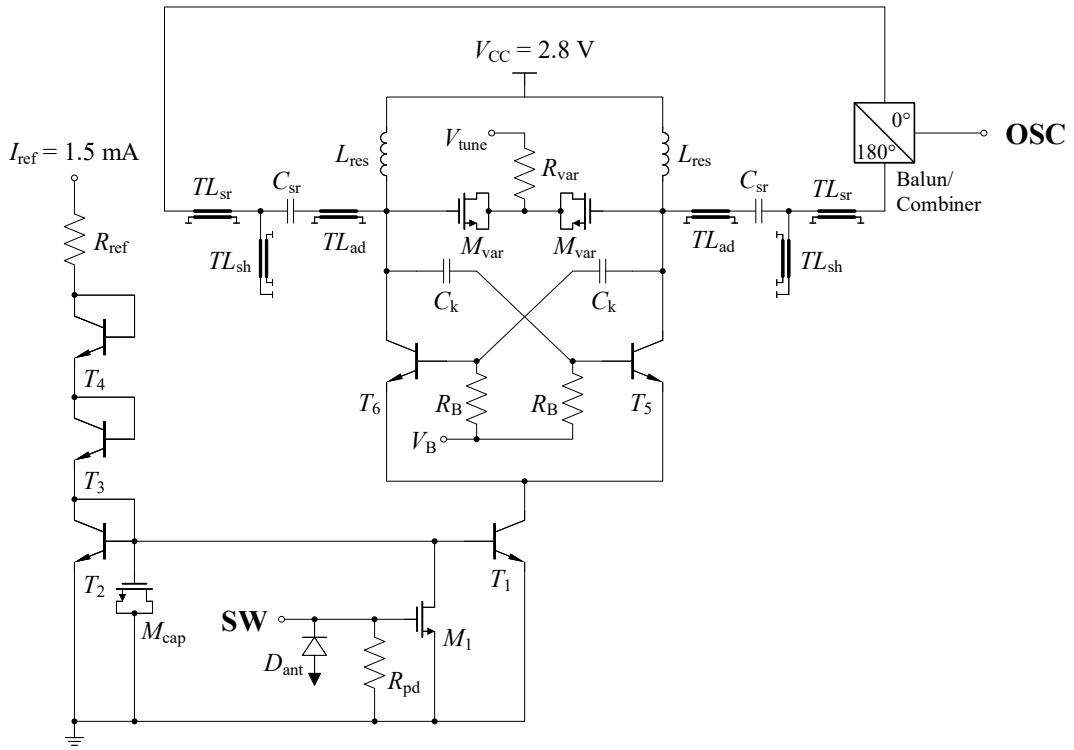

Figure 5.11: Schematic of the 60-GHz SRO circuit [80]♠ ©2022 IEEE

Marchand Balun

To combine the SRO with a single-ended antenna, a Marchand balun was designed for on-chip fabrication to achieve broadband performance. A 3D illustration of the balun and the corresponding metal layers are shown in Figure 5.12. The top two metal layers were chosen for compact broadside coupling and the width of the lines was optimized for an impedance of 50 Ω. The simulated S_{11} performance is better than 20 dB over the full band as shown in Figure 5.13. The insertion loss is 1.3 dB and the amplitude imbalance is less than 0.8 dB over the full band. The phase imbalance is 12° at 60 GHz.

5.3.2 Experimental Results

To prove the proposed concept, a chip was implemented and experimentally characterized. The circuit was fabricated in a 130 nm SiGe BiCMOS technology with f_T and f_{max} up to 300 GHz and 500 GHz, respectively [6]. Figure 5.14 shows a labeled micrograph of the fabricated circuit, with a total area of 0.87 mm^2.

The circuit was measured on wafer using the configuration shown in Figure 5.15. The OSC node was connected using RF signal probes to a spectrum analyzer through an RF power splitter/combiner to measure the output signal. The second combiner port was connected to a signal generator for the much weaker input signal. A pulse generator was connected at the SW node to provide the quench signal for SRO operation. The instruments were provided the same 10 MHz reference signal to ensure a common phase reference. The results were power calibrated by removing the losses of the cables and the setup.

Figure 5.16 shows the frequency tuning characteristics and output power of the free-running

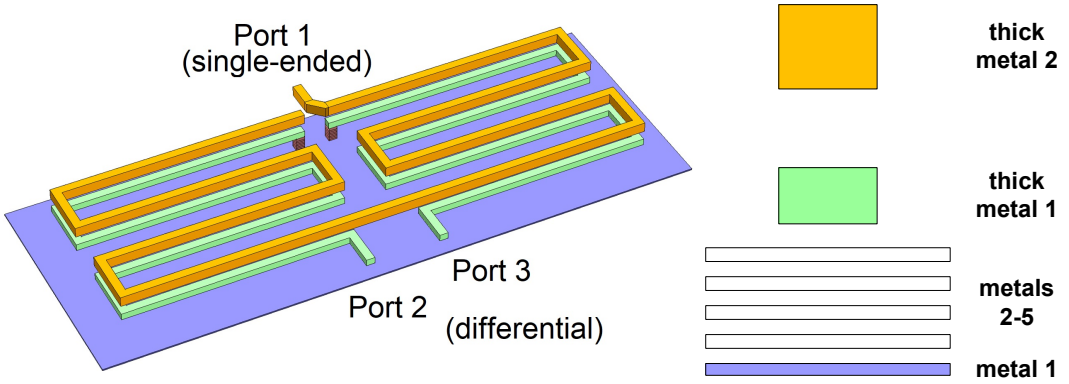

Figure 5.12: 3D drawing of Marchand balun (left) and cross-section of the corresponding metal layers drawn to scale (right) [80]♠ ©2022 IEEE

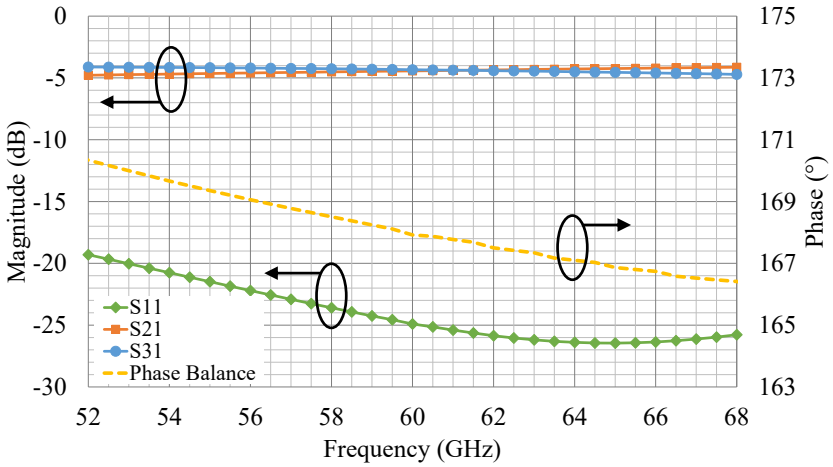

Figure 5.13: S-parameter magnitude and phase simulations of the 60-GHz Marchand balun [80]♠ ©2022 IEEE

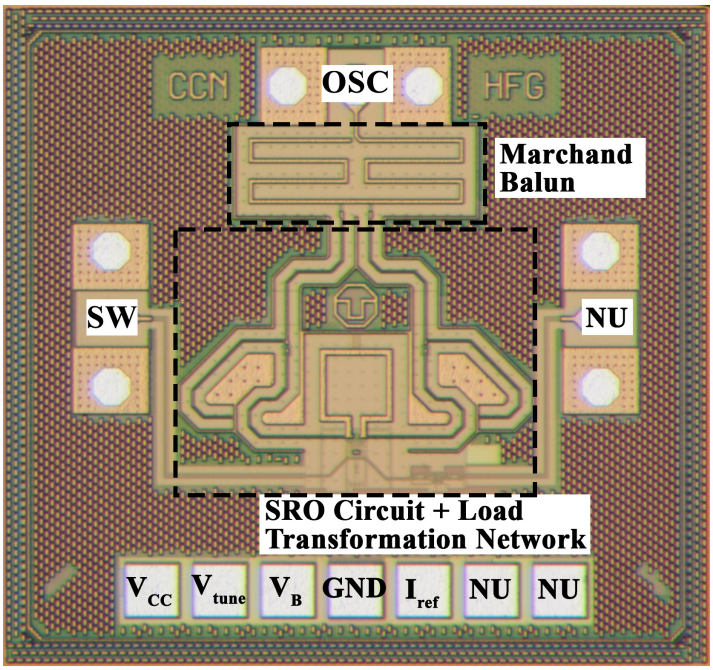

Figure 5.14: Micrograph of the 60-GHz SRO chip (area = 970 × 900 μm^2) [80]♠ ©2022 IEEE

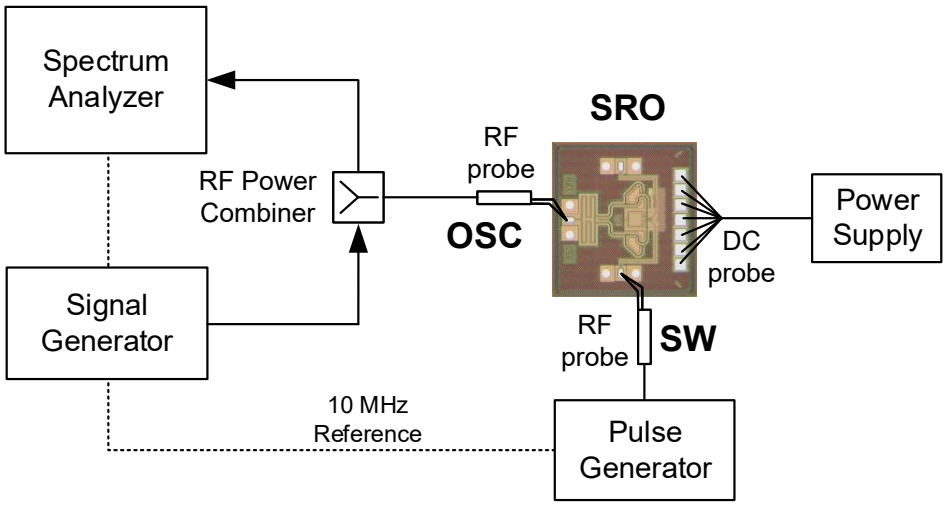

Figure 5.15: On-wafer measurement setup of the 60-GHz SRO circuit [80]♠ ©2022 IEEE

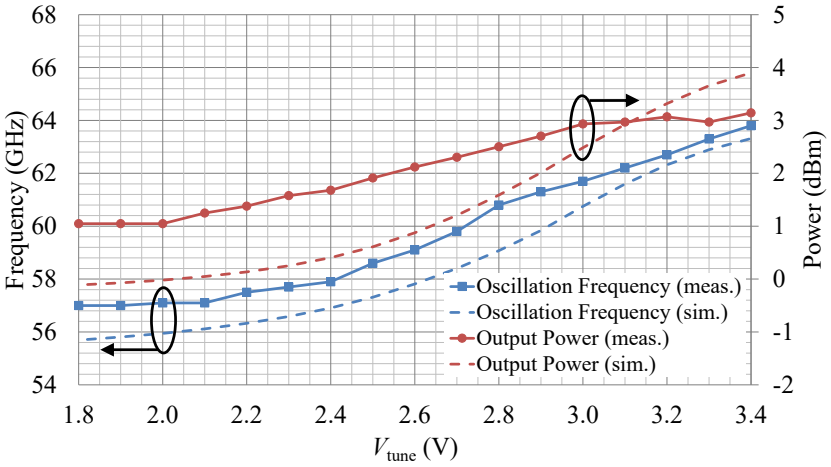

Figure 5.16: Oscillation frequency and output power of the 60-GHz SRO circuit against V_{tune} [80]♠ ©2022 IEEE

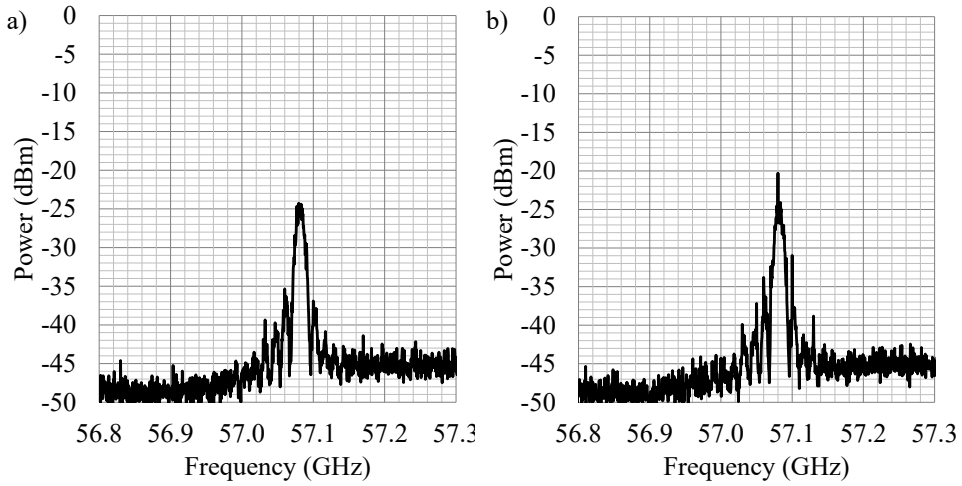

Figure 5.17: Measured SRO spectrum for f_{sw} = 10 MHz and f_{inj} = 57 GHz, with (a) P_{inj} = -82.5 dBm and (b) P_{inj} = -79.5 dBm [80]♠ ©2022 IEEE

SRO circuit when no quench signal was applied at SW. The tuning voltage V_{tune} was varied between 1.8 V and 3.4 V, and the oscillation frequency and output power were recorded. A good fit between measurement and simulation results is shown. The output power varies by approximately 2 dB in this range to reach a maximum of 3.1 dBm.

To test the super-regenerative operation of the circuit, a 10 MHz frequency pulse was used at SW node to facilitate the characterization. The pulse had an amplitude of 0.5 V and a duty cycle of 30% for periodic quenching of the oscillator, corresponding to a dc power dissipation of 25 mW. A weak input signal with frequency f_{inj} = 57 GHz was applied to the power combiner at OSC node, as shown in Figure 5.15. The output was measured in frequency domain using a spectrum analyzer.

An input signal that is too weak to be coherently regenerated by the SRO appears indistinguishable from noise in the spectrum. Due to the quenching action, the noise floor is superimposed by a sinc envelope, which is centered around the oscillation frequency of the

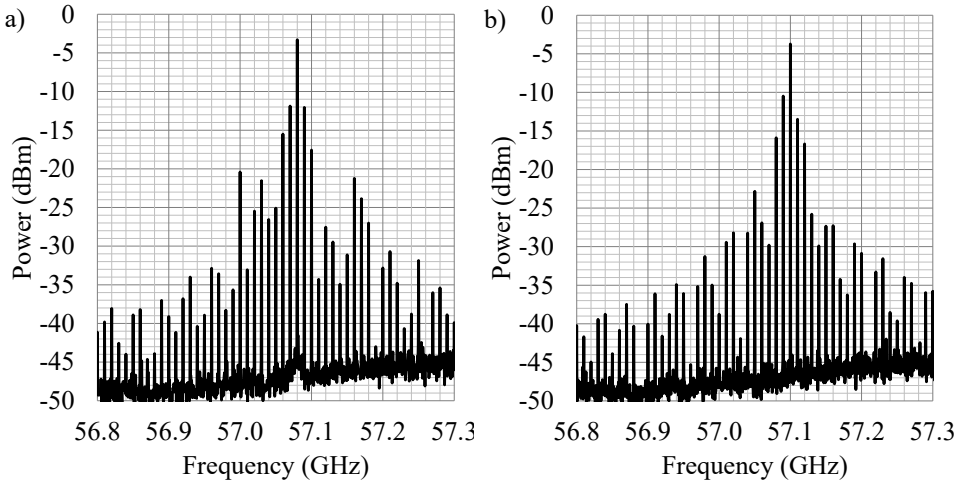

Figure 5.18: Measured SRO spectrum for f_{sw} = 10 MHz and P_{inj} = -38.5 dBm, with (a) f_{inj} = 57.0 GHz, and (b) f_{inj} = 57.1 GHz [80]♠ ©2022 IEEE

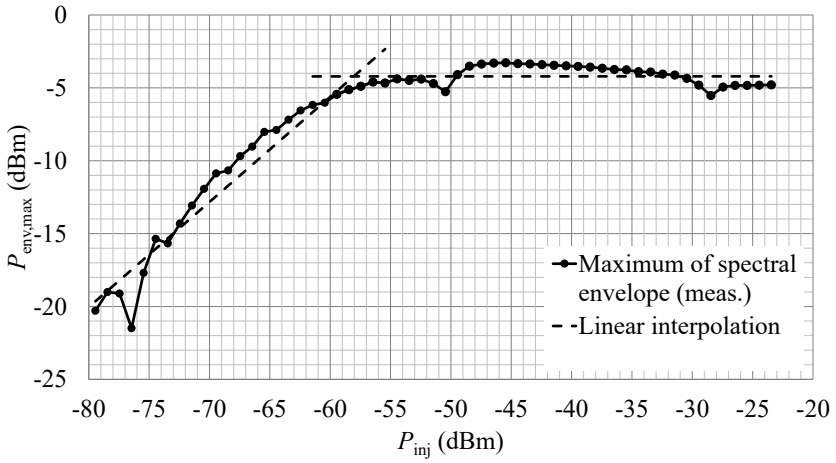

Figure 5.19: Plot of measured spectral envelope $P_{env,max}$ at varying input power P_{inj} [80]♠ ©2022 IEEE

SRO. This can be seen when the input power P_{inj} = -82.5 dBm as in Figure 5.17 (a). Increasing the power by 3 dB to P_{inj} = -79.5 dBm as in Figure 5.17 (b), a Dirac comb trail of impulses with 10 MHz is becoming visible, which indicates a phase-coherent regeneration of the input signal [19].

This defines the minimum detectable signal $P_{inj,min}$ of the SRO as -79.5 dBm. Reaching a steady-state output power of 1 dBm at 57 GHz, as shown in Figure 5.16, this $P_{inj,min}$ corresponds to a maximum regenerative gain capability of 80.5 dB. Figure 5.18 shows further spectrum measurements at higher input power P_{inj} = -38.5 dBm and an additional input frequency f_{inj} = 57.1 GHz. The noise around the center frequency is low at higher input power as the phase regeneration error is reduced, and the peak amplitude is also higher.

A sweep of the input power was performed and the maximum of the spectral envelope $P_{env,max}$ was recorded for every input power P_{inj}. The result is shown in Figure 5.19. The plot shows the transition of the circuit from linear mode at low input levels to logarithmic

mode at high input levels due to output level saturation. The parameter $P_{i,N}$, at which the input power corresponds to the transition from linear to logarithmic mode, is calculated from the intersection of the extrapolated lines as $P_{i,N}$ = -58 dBm [19].

Table 5.3 shows a comparison of the proposed SRO with the current state of the art, including one non-SRO active reflector circuit. The proposed circuit shows the highest maximum gain in this frequency range around 60 GHz, largely owing to the optimized quenching circuit for high sensitivity. It is worth noting that [3] employs quench waveform shaping techniques, which further enhance the sensitivity of the SRO. Similar techniques can also be combined with this work to achieve higher gain. This work also shows very competitive dc power dissipation, which is the best among the SiGe BiCMOS circuits, and is only surpassed by the CMOS circuits. Achieving this high efficiency was possible through the design of a passive load optimization network, leading to improved dc-to-RF efficiency. This work also achieves far higher gain and output power than non-SRO active reflectors, showing the advantages of the SRO concept over non-SRO active reflectors, which face stability issues with high gain performance.

Ref.	Technology	Concept of Operation	f_{osc} (GHz)	P_{out} (dBm)	P_{DC} (mW)	f_{sw} (MHz)	Area (mm^2)	$P_{inj,min}$ (dBm)	Max. Gain (dB)
[19]	SiGe BiCMOS	SRO	25.3	7.8	110	4.5	0.63	-110	117.8
[37]	SiGe BiCMOS	SRO	34.5	5.6	122	60	0.83	-80	85.6
[46]	SiGe BiCMOS	SRO	60	7.3	107	3100	0.75	-31	37
[47]	SOI CMOS	SRO	60	1.5	10	10000	0.49	-42	43.5
[90]	SOI CMOS	Non-SRO	77	-14	18	N.A.	0.50	N.A.	20
This work [80]♠	**SiGe BiCMOS**	**SRO**	**60**	**3.1**	**25**	**10**	**0.87**	**-79.5**	**80.5**

Table 5.3: Performance summary and comparison of FMCW radar active reflector ICs [80]♠ ©2022 IEEE

6 Conclusion and Outlook

To address the rising demands of a smart interconnected world, the communication and sensing devices are becoming increasingly numerous and power hungry. New innovative approaches are needed to improve the efficiency of electronic systems and save precious energy, while maintaining competitive levels of performance. This work presented the analysis, modeling, design, and characterization of super-regenerative receivers, and complementary system components, and discussed how these techniques can be useful for wireless communication and radar applications. This work advanced the state of the art in the following ways:

- Modeling and analysis were performed for SRO circuits, which are the main building blocks of super-regenerative receivers. The analysis covered aspects of SRO design that were previously unexplored in the literature, including amplitude start-up behavior, and the factors affecting phase sampling effectiveness. Design guidelines were drawn from the results of this analysis, such as how to characterize SRO circuits in spectrum, how to increase symbol rate for high data rate communication, and how to improve phase sensitivity in order to increase the regenerative gain.

- Millimeter-wave SRO circuits have been designed, implemented, and characterized, which proved the ability to perform simultaneous phase and amplitude modulation in SRO integrated circuits. Consequently, this has had a significant positive effect on the spectral efficiency and the maximum attainable data rate from such circuits, increasing the maximum data rate by a factor of 80 to 16 Gbit/s.

- For the previous advancement, it was also necessary to increase the operation frequency, in order to reach the respectively high bandwidth and symbol rate requirements. This work presented the characterization results of a phase sampling SRO that operated at a frequency of 180 GHz, which is an improvement by a factor of 3 against the state of the art. Additionally, the SRO frequency reached a challenging 36% of the peak technology f_{max}, which is known to complicate the SRO design due to the low transistor gain at this frequency. A highly competitive regenerative gain of 58 dB was achieved at 180 GHz, and another SRO presented here reached a gain of 80 dB at 60 GHz, which are better than any other phase sampling SRO above 35 GHz.

- Among millimeter-wave wireless communication systems around 200 GHz, this work improved the energy efficiency in wireless transmission experiments to 0.6 pJ/bit for a moderately high data rate of 16 Gbit/s. This is due to the large and highly efficient gain from the SRO circuit, with a pulsed dc power consumption of only 8.8 mW. Large gain in the SRO also allows the use of passive mixing in the following stage, which does not add to the power consumption and further improves the energy efficiency.

- In order to achieve high symbol rates, circuit techniques for generating high-speed rectangular quench waveforms have been explored. Two broadband circuits have

been designed and characterized, which were able to generate quench signals up to a frequency of 25 GHz. One of these circuits was an RF Schmitt trigger operating up to 18 GHz, which corresponds to an improvement by a factor of 18 compared to prior work.

The use of super-regenerative receivers in millimeter-wave communication and radar applications is a relatively new application, and many of the underlying challenges are still largely unexplored. Thus, the research presented in this work can be carried forward in a number of ways. Some of the key areas where millimeter-wave super-regenerative receivers can be better understood and improved are listed below:

- The theory of phase sampling in SROs can be extended to include all the factors affecting sampling effectiveness, including SRO transfer function, quench waveform, and noise. A comprehensive noise analysis could clarify the dependence of phase sampling errors on noise temperature and bandwidth, and would explain the dependence of SRO performance on noise figure and phase noise. Only then would the noise performance of SROs as a first gain stage in the receiver, similar to LNAs, and its impact on following stages be fully understood. Additionally, more careful quench waveform design could lead to better SRO phase sensitivity in FMCW radar active reflectors, but this might prove to be difficult in high data rate communication systems due to their high clock speeds.

- The energy efficiency of pulsed SRO systems could be further drastically improved by building them into wake-up receivers, which have the potential to reduce their power consumption to a few microwatts. SROs are exceptionally adapted for this type of systems as they inherently have an OFF-switch through their quenching circuits. Furthermore, if combined with passive mixers, this would even reduce the number of active components that have to be turned off in order to save power.

- The design of transmitters that are based on SRO circuits could be very beneficial to build a complete energy-efficient system using super-regenerative techniques. Several interesting research topics would arise, as in this case, SROs would be used as power amplifiers and would have different challenges to overcome. The output power would need to be improved, and the SROs would have to be designed as power oscillators, while still fulfilling the requirements of fast start-up and good phase sensitivity. Another challenge would be the synchronization of transmit and receiver pulses, which could be resolved using peak search algorithms in the receiver.

- IQ mixers could be designed and integrated into millimeter-wave super-regenerative receivers, which would facilitate the processing of quadrature modulation techniques. In turn, this would improve the spectral efficiency of SROs and enable higher data rates, but might increase the chip area and place higher requirements on SNR.

- Research on antennas could be done to determine their influence on high data rate SRO pulses, and to draw design guidelines. Such SRO pulses are short in time and have very fast transients, and could benefit from research that has already been done on antennas for UWB systems. Another interesting aspect could be the phase linearity over the large SRO bandwidth.

References

[1] F. Ellinger, *Radio Frequency Integrated Circuits and Technologies*. Berlin, Heidelberg: Springer Berlin Heidelberg, 2007, ISBN: 978-3-540-35788-9.

[2] T. S. Rappaport, Y. Xing, O. Kanhere, *et al.*, "Wireless Communications and Applications Above 100 GHz: Opportunities and Challenges for 6G and Beyond," *IEEE Access*, vol. 7, pp. 78 729–78 757, 2019, ISSN: 2169-3536.

[3] Document FCC 18-21, *Notice of Proposed Rulemaking*, Feb. 2018.

[4] N. Joram, "Design of a Dual Band Local Positioning System," Ph.D. thesis, Technische Universität Dresden, 2015.

[5] A. Strobel, "Geschaltete Oszillatoren für Hochfrequenz- Entfernungsmesssysteme," Ph.D. thesis, Technische Universität Dresden, 2014.

[6] B. Heinemann, R. Barth, D. Bolze, *et al.*, "SiGe HBT Technology with fT/fmax of 300GHz/500GHz and 2.0 ps CML Gate Delay," in *2010 International Electron Devices Meeting*, IEEE, Dec. 2010, pp. 30.5.1–30.5.4, ISBN: 978-1-4424-7418-5.

[7]♠ H. Ghaleb, C. Carlowitz, D. Fritsche, *et al.*, "A 180-GHz Super-Regenerative Oscillator with up to 58 dB Gain for Efficient Phase and Amplitude Recovery," *IEEE Trans. Microw. Theory Tech.*, vol. 68, no. 6, pp. 2011–2019, Jun. 2020.

[8]♠ H. Ghaleb, M. El-Shennawy, U. Jorges, C. Carta, and F. Ellinger, "Nonlinear modeling of cross-coupled regenerative sampling oscillators," in *13th Conference on Ph.D. Research in Microelectronics and Electronics (PRIME)*, vol. 1, IEEE, Jun. 2017, pp. 69–72, ISBN: 978-1-5090-6508-0.

[9] A. Ferschischi, H. Ghaleb, M. Schulz, U. Jorges, C. Carta, and F. Ellinger, "Nonlinear Analysis of Cross-Coupled Super-Regenerative Oscillators," *IEEE Transactions on Circuits and Systems I: Regular Papers*, vol. 68, no. 6, pp. 2368–2381, Jun. 2021, ISSN: 1549-8328.

[10] D. Fritsche, P. Starke, C. Carta, and F. Ellinger, "A Low-Power SiGe BiCMOS 190-GHz Transceiver Chipset With Demonstrated Data Rates up to 50 Gbit/s Using On-Chip Antennas," *IEEE Transactions on Microwave Theory and Techniques*, pp. 1–12, 2017, ISSN: 0018-9480.

[11] C. Carlowitz, T. Girg, H. Ghaleb, and X.-q. Du, "Efficient Ultra-High Speed Communication with Simultaneous Phase and Amplitude Regenerative Sampling (SPARS)," *Frequenz*, vol. 71, no. 9-10, pp. 449–461, Sep. 2017, ISSN: 2191-6349.

[12] C. Carlowitz and M. Vossiek, "Concept for a novel low-complexity QAM transceiver architecture suitable for operation close to transition frequency," in *2015 IEEE MTT-S International Microwave Symposium*, IEEE, May 2015, pp. 1–4, ISBN: 978-1-4799-8275-2.

[13] C. Carlowitz and M. Vossiek, "Demonstration of an efficient high speed communication link based on regenerative sampling," in *2017 IEEE MTT-S International Microwave Symposium (IMS)*, IEEE, Jun. 2017, pp. 71–74, ISBN: 978-1-5090-6360-4.

[14] J. Whitehead, *Super-Regenerative Receivers*. Cambridge University Press, 1950.

[15] G. MacFarlane and J. Whitehead, "The theory of the super-regenerative receiver operated in the linear mode," *Journal of the Institution of Electrical Engineers - Part III: Radio and Communication Engineering*, vol. 95, no. 35, pp. 143–157, May 1948, ISSN: 2054-0604.

[16] A. Strobel, M. Schulz, F. Ellinger, C. Carlowitz, and M. Vossiek, "Analysis of phase sampling noise of switched injection-locked oscillators," in *2014 IEEE Topical Conference on Wireless Sensors and Sensor Networks (WiSNet)*, IEEE, Jan. 2014, pp. 43–45, ISBN: 978-1-4799-2300-7.

[17] B. van der Pol, "The Nonlinear Theory of Electric Oscillations," *Proceedings of the IRE*, vol. 22, no. 9, pp. 1051–1086, Sep. 1934, ISSN: 0096-8390.

[18] M. Schulz, N. Joram, C. Tzschoppe, and F. Ellinger, "Design of a switched injection-locked oscillator as an active backscatter transponder for a 2.45 GHz FMCW radar system," *GeMiC 2016 - 2016 German Microwave Conference*, pp. 267–270, 2016.

[19] M. V. Thayyil, S. Li, N. Joram, and F. Ellinger, "A K-Band SiGe Superregenerative Amplifier for FMCW Radar Active Reflector Applications," *IEEE Microw. Wirel. Components Lett.*, vol. 28, no. 7, pp. 603–605, Jul. 2018, ISSN: 1531-1309.

[20] M. Vossiek and P. Gulden, "The switched injection-locked oscillator: A novel versatile concept for wireless transponder and localization systems," *Microwave Theory and Techniques, ...*, vol. 56, no. 4, pp. 859–866, 2008.

[21] X. Ge, M. Arcak, and K. N. Salama, "Nonlinear analysis of cross-coupled oscillator circuits," in *2008 47th IEEE Conference on Decision and Control*, IEEE, Jun. 2008, pp. 13–18, ISBN: 978-1-4244-3123-6.

[22] M. El-Shennawy, N. Joram, and F. Ellinger, "Nonlinear modelling of automatic gain control loops considering loop dynamics and stability," in *12th Conference on Ph.D. Research in Microelectronics and Electronics (PRIME)*, IEEE, Jun. 2016, pp. 1–4, ISBN: 978-1-5090-0493-5.

[23]♠ H. Ghaleb, M. El-Shennawy, C. Carta, and F. Ellinger, "A 148-GHz regenerative sampling oscillator," in *12th European Microwave Integrated Circuits Conference (EuMIC)*, IEEE, Oct. 2017, pp. 65–68, ISBN: 978-2-87487-048-4.

[24]♠ H. Ghaleb, P. V. Testa, S. Schumann, C. Carta, and F. Ellinger, "A 160-GHz Switched Injection-Locked Oscillator for Phase and Amplitude Regenerative Sampling," *IEEE Microwave and Wireless Components Letters*, vol. 27, no. 9, pp. 821–823, Sep. 2017, ISSN: 1531-1309.

[25]♠ H. Ghaleb, D. Fritsche, C. Carta, and F. Ellinger, "Design and characterization of a 180-GHz on-chip integrated broadband balun," in *2018 IEEE Radio Wirel. Symp.*, IEEE, 2018, pp. 237–239, ISBN: 978-1-5386-0710-7.

[26]♠ H. Ghaleb, C. Carlowitz, D. Fritsche, C. Carta, and F. Ellinger, "A 180-GHz Super-Regenerative Oscillator with up to 58 dB Gain for Efficient Phase Recovery," in *2019 IEEE Radio Freq. Integr. Circuits Symp.*, IEEE, Jun. 2019, pp. 131–134, ISBN: 978-1-7281-1701-0.

[27]♠ H. Ghaleb, D. Fritsche, M. El-Shennawy, P. Starke, C. Carta, and F. Ellinger, "A 180-GHz Passive Integrated SiGe Down-Conversion Mixer with Low Loss and a Broadband Rat-Race Coupler Design," in *2019 14th Eur. Microw. Integr. Circuits Conf.*, IEEE, Sep. 2019, pp. 172–175, ISBN: 978-2-87487-056-9.

[28] J. Bohorquez, A. Chandrakasan, and J. Dawson, "Frequency-Domain Analysis of Super-Regenerative Amplifiers," *IEEE Trans. Microw. Theory Tech.*, vol. 57, no. 12, pp. 2882–2894, Dec. 2009, ISSN: 0018-9480.

[29] C. Carlowitz, A. Esswein, R. Weigel, and M. Vossiek, "Regenerative sampling self-mixing receiver: A novel concept for low complexity phase demodulation," in *2013 IEEE MTT-S International Microwave Symposium Digest (MTT)*, IEEE, Jun. 2013, pp. 1–4, ISBN: 978-1-4673-6176-7.

[30] D. Fritsche, G. Tretter, C. Carta, and F. Ellinger, "Millimeter-Wave Low-Noise Amplifier Design in 28-nm Low-Power Digital CMOS," *IEEE Transactions on Microwave Theory and Techniques*, vol. 63, no. 6, pp. 1910–1922, Jun. 2015, ISSN: 0018-9480.

[31] A. Barghouthi, C. Carta, U. Jörges, and F. Ellinger, "On the oscillation limits of HBT cross-coupled oscillators," *International Journal of Microwave and Wireless Technologies*, vol. 4, no. 4, pp. 435–440, Aug. 2012, ISSN: 1759-0787.

[32] B. Van Der Pol, "The Effect of Regeneration on the Received Signal Strength," *Proceedings of the IRE*, vol. 16, no. 8, pp. 1045–1052, Aug. 1928, ISSN: 0096-8390.

[33] D. Fritsche, S. Li, N. Joram, C. Carta, and F. Ellinger, "Design and characterization of a 190-GHz voltage-controlled oscillator," in *2016 46th Eur. Microw. Conf.*, IEEE, Oct. 2016, pp. 493–496, ISBN: 978-2-87487-043-9.

[34] B. Gilbert, "The MICROMIXER: a highly linear variant of the Gilbert mixer using a bisymmetric Class-AB input stage," *IEEE Journal of Solid-State Circuits*, vol. 32, no. 9, pp. 1412–1423, 1997, ISSN: 00189200.

[35] G. Tretter, D. Fritsche, J. Leufker, C. Carta, and F. Ellinger, "Zero-Ohm transmission lines for millimetre-wave circuits in 28 nm digital CMOS," *Electronics Letters*, vol. 51, no. 11, pp. 845–847, May 2015, ISSN: 0013-5194.

[36] K. Wu, S. Muralidharan, and M. M. Hella, "Decoupling Structures for Millimeter Wave Integrated Circuits in Digital CMOS Processes," *IEEE Transactions on Electron Devices*, vol. 65, no. 2, pp. 788–792, Feb. 2018, ISSN: 0018-9383.

[37] A. Strobel, C. Carlowitz, R. Wolf, F. Ellinger, and M. Vossiek, "A Millimeter-Wave Low-Power Active Backscatter Tag for FMCW Radar Systems," *IEEE Trans. Microw. Theory Tech.*, vol. 61, no. 5, pp. 1964–1972, May 2013, ISSN: 0018-9480.

[38] G. Feng, C. C. Boon, F. Meng, and X. Yi, "A 100-GHz 0.21-K NETD 0.9-mW/pixel Charge-Accumulation Super-Regenerative Receiver in 65-nm CMOS," *IEEE Microwave and Wireless Components Letters*, vol. 26, no. 7, pp. 531–533, Jul. 2016, ISSN: 1531-1309.

[39] S. Ma, H. Yu, Q. J. Gu, and J. Ren, "A 7.52-dB Noise Figure 128.75–132.25-GHz Super-Regenerative Receiver With 0.615-fW/$\sqrt{\text{Hz}}$ NEP by Coupled Oscillator Networks for Portable Imaging System in 65-nm CMOS," *IEEE Transactions on Microwave Theory and Techniques*, vol. 66, no. 9, pp. 4095–4107, Sep. 2018, ISSN: 0018-9480.

[40] Y. Shang, H. Yu, S. Hu, Y. Liang, X. Bi, and M. A. Arasu, "High-sensitivity CMOS super-regenerative receiver with quench-controlled high-q metamaterial resonator for millimeter-wave imaging at 96 and 135 GHz," *IEEE Transactions on Microwave Theory and Techniques*, vol. 62, no. 12, pp. 3095–3106, Dec. 2014, ISSN: 0018-9480.

[41] A. Tang and M.-C. F. Chang, "183GHz 13.5mW/pixel CMOS regenerative receiver for mm-wave imaging applications," in *2011 IEEE International Solid-State Circuits Conference*, IEEE, Feb. 2011, pp. 296–298, ISBN: 978-1-61284-303-2.

[42] D.-G. Lee and P. P. Mercier, "A 1.65 mW PLL-free PSK receiver employing super-regenerative phase sampling," in *2015 IEEE Biomedical Circuits and Systems Conference (BioCAS)*, IEEE, Oct. 2015, pp. 1–4, ISBN: 978-1-4799-7234-0.

[43] M. Schulz, A. Strobel, N. Joram, and F. Ellinger, "Design of a switched injection-locked oscillator at 2.45 GHz for a local positioning system," in *2014 9th European Microwave Integrated Circuit Conference*, IEEE, Oct. 2014, pp. 116–119, ISBN: 978-2-8748-7036-1.

[44] M. Schulz, N. Joram, and F. Ellinger, "Design of a common-base Colpitts switched injection-locked oscillator at 2.45 GHz for a FMCW radar system," in *2015 IEEE 16th Annual Wireless and Microwave Technology Conference (WAMICON)*, IEEE, Apr. 2015, pp. 1–5, ISBN: 978-1-4799-7521-1.

[45] A. Esswein, R. Weigel, T. Ussmueller, C. Carlowitz, and M. Vossiek, "An Improved Switched Injection-Locked Oscillator for Ranging and Communication Systems," in *Proceedings of the 43rd European Microwave Conference*, 2013, pp. 592–595, ISBN: 9782874870323.

[46] A. Ferchichi, H. Ghaleb, C. Carta, and F. Ellinger, "Analysis and Design of 60-GHz Switched Injection-Locked Oscillator with up to 38 dB Regenerative Gain and 3.1 GHz Switching Rate," in *2018 IEEE 61st International Midwest Symposium on Circuits and Systems (MWSCAS)*, IEEE, 2018, pp. 340–343, ISBN: 9781538673928.

[47] A. Ferschischi, H. Ghaleb, Z. Tibenszky, C. Carta, and F. Ellinger, "A power efficient 60-GHz super-regenerative oscillator with 10-GHz switching rate in 22-nm FD-SOI CMOS," in *IEEE MTT-S International Microwave Symposium Digest*, 2020, pp. 349–352, ISBN: 9781728168159.

[48] D. Fritsche, G. Tretter, P. Starke, C. Carta, and F. Ellinger, "A Low-Power SiGe BiCMOS 190-GHz Receiver With 47-dB Conversion Gain and 11-dB Noise Figure for Ultralarge-Bandwidth Applications," *IEEE Transactions on Microwave Theory and Techniques*, vol. 65, no. 10, pp. 4002–4013, Oct. 2017, ISSN: 0018-9480.

[49] U. R. Pfeiffer, E. Ojefors, and Y. Zhao, "A SiGe quadrature transmitter and receiver chipset for emerging high-frequency applications at 160GHz," in *2010 IEEE International Solid-State Circuits Conference - (ISSCC)*, vol. 53, IEEE, Feb. 2010, pp. 416–417, ISBN: 978-1-4244-6033-5.

[50] J. Dirk Leufker, A. Strobel, C. Carta, and F. Ellinger, "A wideband planar microstrip to coplanar stripline transition (balun) at 35 GHz," in *Proceedings of the 2013 9th Conference on Ph.D. Research in Microelectronics and Electronics (PRIME)*, IEEE, Jun. 2013, pp. 305–308, ISBN: 978-1-4673-4581-1.

[51] V. Issakov, M. Wojnowski, and G. Sommer, "Technique for Accurate Characterization of Baluns Using One-Port S-Parameters Measurements," in *IEEE EuMC*, 2011, pp. 305–308, ISBN: 9782874870224.

[52] M. Goldfarb and R. Pucel, "Modeling via hole grounds in microstrip," *IEEE Microwave and Guided Wave Letters*, vol. 1, no. 6, pp. 135–137, Jun. 1991, ISSN: 1051-8207.

[53] H. J. Ng, M. Jahn, R. Feger, C. Wagner, and A. Stelzer, "An Efficient SiGe Double-Balanced Mixer with a Differential Rat-Race Coupler," in *2013 Eur. Microw. Integr. Circuit Conf.*, 2013, pp. 580–583, ISBN: 9782874870323.

[54] S. Maas, *Microwave Mixers*, 1st ed. Artech House, 1986, ISBN: 0890066051.

[55] D. Fritsche, J. D. Leufker, G. Tretter, C. Carta, and F. Ellinger, "A Low-Power Broadband 200 GHz Down-Conversion Mixer with Integrated LO-Driver in 0.13 μm SiGe BiCMOS," *IEEE Microw. Wirel. Components Lett.*, vol. 25, no. 9, pp. 594–596, Sep. 2015, ISSN: 1531-1309.

[56] E. Ojefors, B. Heinemann, and U. R. Pfeiffer, "Subharmonic 220- and 320-GHz SiGe HBT Receiver Front-Ends," *IEEE Transactions on Microwave Theory and Techniques*, vol. 60, no. 5, pp. 1397–1404, May 2012, ISSN: 0018-9480.

[57] M. Elkhouly, Y. Mao, S. Glisic, C. Meliani, F. Ellinger, and J. C. Scheytt, "A 240 GHz direct conversion IQ receiver in 0.13 μm SiGe BiCMOS technology," in *2013 IEEE Radio Frequency Integrated Circuits Symposium (RFIC)*, IEEE, Jun. 2013, pp. 305–308, ISBN: 978-1-4673-6062-3.

[58] Y. Mao, K. Schmalz, J. Borngraber, and J. C. Scheytt, "245-GHz LNA, Mixer, and Subharmonic Receiver in SiGe Technology," *IEEE Transactions on Microwave Theory and Techniques*, vol. 60, no. 12, pp. 3823–3833, Dec. 2012, ISSN: 0018-9480.

[59] O. Inac, A. Fung, and G. M. Rebeiz, "Double-balanced 130-180 GHz passive and balanced 145-165 GHz active mixers in 45 nm CMOS," in *2011 IEEE Custom Integrated Circuits Conference (CICC)*, IEEE, Sep. 2011, pp. 1–4, ISBN: 978-1-4577-0222-8.

[60] Y. Sun and C. J. Scheytt, "A 122 GHz Sub-Harmonic Mixer With a Modified APDP Topology for IC Integration," *IEEE Microwave and Wireless Components Letters*, vol. 21, no. 12, pp. 679–681, Dec. 2011, ISSN: 1531-1309.

[61] W. L. Chang and C. Meng, "A Miniature 200-GHz Subharmonic Mixer With a Folded 180° Hybrid Using Equal-Length Edge- and Broadside-Coupled Lines," *IEEE Microwave and Wireless Components Letters*, vol. 28, no. 4, pp. 338–340, Apr. 2018, ISSN: 1531-1309.

[62] B. Khamaisi and E. Socher, "130-320-GHz CMOS Harmonic Down-Converters Around and Above the Cutoff Frequency," *IEEE Transactions on Microwave Theory and Techniques*, vol. 63, no. 7, pp. 2275–2288, Jul. 2015, ISSN: 0018-9480.

[63] P. Stärke, C. Carta, F. Ellinger, and S. Member, "Direct Chip-to-Waveguide Transition Realized with Wire Bonding for 140 GHz to 220 GHz G-Band," *IEEE Trans. Terahertz Sci. Technol.*, pp. 1–7, 2020.

[64]♠ H. Ghaleb, G. Belfiore, C. Carta, and F. Ellinger, "A SiGe HBT limiting amplifier for fast switching of mm-wave super-regenerative oscillators," in *Proceedings of the 30th Symposium on Integrated Circuits and Systems Design Chip on the Sands - SBCCI*, Fortaleza, Brazil: ACM Press, 2017, pp. 114–119, ISBN: 9781450351065.

[65]♠ H. Ghaleb, Y. Zhu, C. Carta, and F. Ellinger, "A 0.2–18 GHz Schmitt Trigger with up to 13%-–85% Duty-Cycle Tuning in 130nm SiGe BiCMOS," in *2019 12th German Microwave Conference (GeMiC)*, IEEE, Mar. 2019, pp. 107–110, ISBN: 978-3-9812668-9-4.

[66] G. Belfiore, L. Szilagyi, R. Henker, U. Jörges, and F. Ellinger, "Design of a 56 Gbit/s 4-level pulse-amplitude-modulation inductor-less vertical-cavity surface-emitting laser driver integrated circuit in 130 nm BiCMOS technology," *IET Circuits, Devices & Systems*, vol. 9, no. 3, pp. 213–220, May 2015, ISSN: 1751-858X.

[67] E. Cherry and D. Hooper, "The design of wide-band transistor feedback amplifiers," English, *Proceedings of the Institution of Electrical Engineers*, vol. 110, 375–389(14), 2 Feb. 1963, ISSN: 0020-3270.

[68] Y. Greshishchev and P. Schvan, "A 60-dB gain, 55-dB dynamic range, 10-Gb/s broadband SiGe HBT limiting amplifier," *IEEE Journal of Solid-State Circuits*, vol. 34, no. 12, pp. 1914–1920, 1999, ISSN: 00189200.

[69] C. Holdenried, J. Haslett, and M. Lynch, "Analysis and design of HBT Cherry-Hooper amplifiers with emitter-follower feedback for optical communications," *IEEE Journal of Solid-State Circuits*, vol. 39, no. 11, pp. 1959–1967, Nov. 2004, ISSN: 0018-9200.

[70] R. Krithivasan, J. Comeau, Wei-Min Lance Kuo, Yuan Lu, J. Cressler, and A. Joseph, "A 24 GHz broadband SiGE HBT limiting amplifier," in *Proceedings of the Bipolar/BiCMOS Circuits and Technology Meeting*, IEEE, 2005, pp. 208–211, ISBN: 0-7803-9309-0.

[71] O. Wohlgemuth, P. Paschke, and Y. Baeyens, "SiGe broadband amplifiers with up to 80 GHz bandwidth for optical applications at 43 Gbit/s and beyond," in *33rd European Microwave Conference Proceedings*, vol. 3, IEEE, 2003, 1087–1090 Vol.3, ISBN: 1-58053-834-7.

[72] Y. Su, G. Liu, and H. Schumacher, "Limiting Amplifiers for Bits Recovery of Gbps Analog BPSK / QPSK Demodulator," in *Ph.D. Research in Microelectronics and Electronics (PRIME), 2010 Conference on*, 2010, pp. 1–4, ISBN: 9783981375404.

[73] O. H. Schmitt, "A thermionic trigger," *Journal of Scientific Instruments*, vol. 15, no. 1, pp. 24–26, Jan. 1938, ISSN: 0950-7671.

[74] C. Ridders, "Accurate determination of threshold voltage levels of Schmitt trigger," *IEEE Transactions on Circuits and Systems*, vol. 32, no. 9, pp. 969–970, Sep. 1985, ISSN: 0098-4094.

[75] S. Roy, "Comments on "Accurate Determination of Threshold Voltage Levels of a Schmitt Trigger"," *IEEE Transactions on Circuits and Systems*, vol. 33, no. 7, pp. 734–735, Jul. 1986, ISSN: 0098-4094.

[76] Shih-Lun Chen and Ming-Dou Ker, "A new Schmitt trigger circuit in a 0.13-um 1/2.5-V CMOS process to receive 3.3-V input signals," *IEEE Transactions on Circuits and Systems II: Express Briefs*, vol. 52, no. 7, pp. 361–365, Jul. 2005, ISSN: 1057-7130.

[77] Z. Chen and S. Chen, "A high-speed low voltage CMOS Schmitt Trigger with adjustable hysteresis," in *2017 IEEE/ACIS 16th International Conference on Computer and Information Science (ICIS)*, IEEE, May 2017, pp. 293–297, ISBN: 978-1-5090-5507-4.

[78] F. Yuan, "A high-speed differential CMOS Schmitt trigger with regenerative current feedback and adjustable hysteresis," *Analog Integrated Circuits and Signal Processing*, vol. 63, no. 1, pp. 121–127, Apr. 2010, ISSN: 0925-1030.

[79]♠ H. Ghaleb, A. Ferschischi, N. Joram, and F. Ellinger, "A 60-GHz Receiver Frontend With Gain-Linearity Tuning for FMCW Radar Applications," in *IEEE Radio and Wireless Symposium (RWS)*, IEEE, Jan. 2021, pp. 22–25, ISBN: 978-1-7281-8062-5.

[80]♠ H. Ghaleb, N. Joram, and F. Ellinger, "A 60-GHz Super-Regenerative Oscillator with 80 dB Gain in SiGe BiCMOS for FMCW Radar Active Reflectors," in *IEEE 22nd Topical Meeting on Silicon Monolithic Integrated Circuits in RF Systems (SiRF)*, Las Vegas: IEEE, 2022.

[81] G. Girlando, E. Ragonese, A. Italia, and G. Palmisano, "Bipolar LNA design at different operating frequencies," in *Proceedings of the 2003 International Symposium on Circuits and Systems, 2003. ISCAS '03.*, vol. 1, IEEE, Aug. 2003, pp. I–213–I–216, ISBN: 0-7803-7761-3.

[82] B. Shi, "Mixer linearization using dynamic bias circuit with an integrated diode linearizer," in *2016 IEEE Region 10 Conference (TENCON)*, IEEE, Nov. 2016, pp. 2517–2520, ISBN: 978-1-5090-2597-8.

[83] R. Ciocoveanu, R. Weigel, and V. Issakov, "A Highly-Integrated 60 GHz Receiver for Radar Applications in 28 nm Bulk CMOS," in *2019 IEEE International Conference on Microwaves, Antennas, Communications and Electronic Systems (COMCAS)*, IEEE, Nov. 2019, pp. 1–5, ISBN: 978-1-5386-9549-4.

[84] I. Nasr, R. Jungmaier, A. Baheti, *et al.*, "A Highly Integrated 60 GHz 6-Channel Transceiver With Antenna in Package for Smart Sensing and Short-Range Communications," *IEEE Journal of Solid-State Circuits*, vol. 51, no. 9, pp. 2066–2076, Sep. 2016, ISSN: 0018-9200.

[85] E. Ozturk, D. Genschow, U. Yodprasit, *et al.*, "A 60 GHz SiGe BiCMOS double receive channel transceiver for radar applications," in *2017 12th European Microwave Integrated Circuits Conference (EuMIC)*, vol. 2017-Janua, IEEE, Oct. 2017, pp. 269–272, ISBN: 978-2-87487-048-4.

[86] R. Agethen, M. PourMousavi, H. P. Forstner, *et al.*, "60 GHz industrial radar systems in silicon-germanium technology," in *2013 IEEE MTT-S International Microwave Symposium Digest (MTT)*, IEEE, Jun. 2013, pp. 1–3, ISBN: 978-1-4673-6176-7.

[87] E. Ozturk, D. Genschow, U. Yodprasit, *et al.*, "A 60-GHz SiGe BiCMOS Monostatic Transceiver for FMCW Radar Applications," *IEEE Transactions on Microwave Theory and Techniques*, vol. 65, no. 12, pp. 5309–5323, Dec. 2017, ISSN: 0018-9480.

[88] S Shopov, M. G. Girmat, J. Hascht, and S. P. Voinigescu, "An ultra-low-power 4-channel 60-GHz radar sensor," in *2017 IEEE MTT-S International Microwave Symposium (IMS)*, IEEE, Jun. 2017, pp. 1520–1523, ISBN: 978-1-5090-6360-4.

[89] M. Ortner, H. P. Forstner, L. Verweyen, and T. Ostermann, "A fully integrated homodyne downconverter MMIC in SiGe:C for 60 GHz wireless applications," in *2011 IEEE 11th Topical Meeting on Silicon Monolithic Integrated Circuits in RF Systems*, IEEE, Jan. 2011, pp. 145–148, ISBN: 978-1-4244-8060-9.

[90] M. S. Dadash, J. Hasch, and S. P. Voinigescu, "A 77-GHz active millimeter-wave reflector for FMCW radar," in *2017 IEEE Radio Frequency Integrated Circuits Symposium (RFIC)*, IEEE, Jun. 2017, pp. 312–315, ISBN: 978-1-5090-4626-3.

List of Original Publications

The doctoral research conducted during the time for completion of my degree was presented at the following forums. As noted at the beginning of each chapter, certain material was taken from the following publications, which were also referenced in the text.

First-Author Journal Publications

1. **H. Ghaleb**, C. Carlowitz, D. Fritsche, P. Stärke, F. Protze, C. Carta and F. Ellinger, "A 180-GHz Super-Regenerative Oscillator with up to 58 dB Gain for Efficient Phase and Amplitude Recovery," *IEEE Transactions on Microwave Theory and Techniques (TMTT)*, vol. 68, no. 6, pp. 2011–2019, Jun. 2020. (*Corresponding reference in text:* **[7]**♠)

2. **H. Ghaleb**, P. V. Testa, S. Schumann, C. Carta and F. Ellinger, "A 160-GHz Switched Injection-Locked Oscillator for Phase and Amplitude Regenerative Sampling," *IEEE Microwave and Wireless Component Letters (MWCL)*, vol. 27, no. 9, pp. 821–823, Sep. 2017. (*Corresponding reference in text:* **[24]**♠)

First-Author Conference Publications

1. **H. Ghaleb**, N. Joram and F. Ellinger, "A 60-GHz Super-Regenerative Oscillator with 80 dB Gain in SiGe BiCMOS for FMCW Radar Active Reflectors," *2022 IEEE 22nd Topical Meeting on Silicon Monolithic Integrated Circuits in RF Systems (SiRF)*, Las Vegas, NV, USA, Jan. 2022. (*Corresponding reference in text:* **[80]**♠)

2. **H. Ghaleb**, A. Ferschischi, N. Joram and F. Ellinger, "A 60-GHz Receiver Frontend With Gain-Linearity Tuning for FMCW Radar Applications," *2021 IEEE Radio and Wireless Symposium (RWS)*, San Diego, CA, USA, Jan. 2021. (*Corresponding reference in text:* **[79]**♠)

3. **H. Ghaleb**, D. Fritsche, M. El-Shennawy, P. Stärke, C. Carta and F. Ellinger, "A 180-GHz Passive Integrated SiGe Down-Conversion Mixer with Low Loss and a Broadband Rat-Race Coupler Design," *2019 14th European Microwave Integrated Circuits Conference (EuMIC)*, Paris, France, Oct. 2019. (*Corresponding reference in text:* **[27]**♠)

4. **H. Ghaleb**, C. Carlowitz, D. Fritsche, C. Carta and F. Ellinger, "A 180-GHz Super-Regenerative Oscillator with up to 58 dB Gain for Efficient Phase Recovery," *2019 IEEE Radio Frequency Integrated Circuits Symposium (RFIC)*, Boston, MA, USA, Jun. 2019. (*Corresponding reference in text:* **[26]**♠)

5. **H. Ghaleb**, Y. Zhu, C. Carta and F. Ellinger, "A 0.2–18 GHz Schmitt Trigger with up to 13%–85% Duty-Cycle Tuning in 130nm SiGe BiCMOS," *2019 12th German*

Microwave Conference (GeMiC), Stuttgart, Germany, Mar. 2019. (*Corresponding reference in text:* **[65]♠**)

6. **H. Ghaleb**, D. Fritsche, C. Carta and F. Ellinger, "Design and Characterization of a 180-GHz On-Chip Integrated Broadband Balun," *2018 IEEE Radio Wireless Symposium (RWS)*, Anaheim, CA, USA, Jan. 2018. (*Corresponding reference in text:* **[25]♠**)

7. **H. Ghaleb**, M. El-Shennawy, C. Carta and F. Ellinger, "A 148-GHz Regenerative Sampling Oscillator," *2017 12th European Microwave Integrated Circuits Conference (EuMIC)*, Nuremberg, Germany, Oct. 2017. (*Corresponding reference in text:* **[23]♠**)

8. **H. Ghaleb**, G. Belfiore, C. Carta and F. Ellinger, "A SiGe HBT Limiting Amplifier for Fast Switching of mm-Wave Super-Regenerative Oscillators," *2017 30th Symposium on Integrated Circuits and Systems Design (SBCCI)*, Fortaleza, Brazil, Aug. 2017. (*Corresponding reference in text:* **[64]♠**)

9. **H. Ghaleb**, M. El-Shennawy, U. Jörges, C. Carta and F. Ellinger, "Nonlinear Modeling of Cross-Coupled Regenerative Sampling Oscillators," *2017 13th Conference on Ph.D. Research in Microelectronics and Electronics (PRIME)*, Taormina, Italy, Jun. 2017. (*Corresponding reference in text:* **[8]♠**)

Other Co-Authored Publications

1. A. Ferschischi, **H. Ghaleb**, M. Schulz, U. Jörges, C. Carta and F. Ellinger, "Nonlinear Analysis of Cross-Coupled Super-Regenerative Oscillators," *IEEE Transactions on Circuits and Systems I: Regular Papers (TCAS-I)*, vol. 68, no. 6, pp. 2368–2381, Apr. 2021. (*Corresponding reference in text:* **[9]**)

2. A. Ferschischi, **H. Ghaleb**, C. Carta and F. Ellinger, "61.5-GHz Energy-Efficient Super-Regenerative Oscillator with Tunable Quench Duty Cycle," accepted for publication at *2022 IEEE/MTT-S International Microwave Symposium (IMS)*, Denver, CO, USA, Jun. 2022.

3. Y. Zhu, **H. Ghaleb**, V. Rieß, N. Joram and F. Ellinger, "A 60 GHz Frequency Doubler with 3.4-dBm Output Power and 4.4% DC-to-RF-Efficiency in 130-nm SiGe BiCMOS," accepted for publication at *2021 16th European Microwave Integrated Circuits Conference (EuMIC)*, London, UK, Apr. 2022.

4. A. Ferschischi, **H. Ghaleb**, S. U. Rehman, C. Carta and F. Ellinger, "A Broadband 60-GHz Low Noise Amplifier with 3.2 dB Noise Figure and 24 dB Gain," *2020 15th European Microwave Integrated Circuits Conference (EuMIC)*, Utrecht, Netherlands, Jan. 2021.

5. A. Ferschischi, **H. Ghaleb**, Z. Tibenszky, C. Carta and F. Ellinger, "A Power Efficient 60-GHz Super-Regenerative Oscillator with 10-GHz Switching Rate in 22-nm FD-SOI CMOS," *2020 IEEE/MTT-S International Microwave Symposium (IMS)*, Los Angeles, CA, USA, Aug. 2020.

6. M. V. Thayyil, **H. Ghaleb**, N. Joram and F. Ellinger, "A 28 GHz Superregenerative Amplifier for FMCW Radar Reflector Applications in 45 nm SOI CMOS," *2018 Asia-Pacific Microwave Conference (APMC)*, Kyoto, Japan, Nov. 2018.

7. A. Ferchichi, **H. Ghaleb**, C. Carta and F. Ellinger, "Analysis and Design of 60-GHz Switched Injection-Locked Oscillator with up to 38 dB Regenerative Gain and 3.1 GHz Switching Rate," *2018 IEEE 61st International Midwest Symposium on Circuits and Systems (MWSCAS)*, Windsor, ON, Canada, Aug. 2018.

8. C. Carlowitz, T. Girg, **H. Ghaleb**, and X.-Q. Du, "Efficient Ultra-High Speed Communication with Simultaneous Phase and Amplitude Regenerative Sampling (SPARS)," *Frequenz*, vol. 71, no. 9–10, pp. 449–461, Sep. 2017.

List of Abbreviations

5G	5th generation cellular standard
6G	6th generation cellular standard
ac	alternating current
ADC	analog-to-digital converter
AGC	automatic gain control
BEOL	back end of line
BER	bit error rate
BiCMOS	integration of bipolar and CMOS transistors
CAD	computer-aided design
CMOS	complementary metal oxide semiconductor
DAC	digital-to-analog converter
dc	direct current
DFG	German Research Foundation
DSP	digital signal processing
EF	emitter follower
EM	electromagnetic
EVM	error vector magnitude
FCC	United States Federal Communications Commission
FMCW	frequency-modulated continuous wave
GCPW	grounded coplanar waveguide
HBT	heterojunction bipolar transistor
IC	integrated circuit
IF	intermediate frequency
ISI	inter-symbol interference
LNA	low-noise amplifier
LO	local oscillator
LPF	low-pass filter
LSB	lower side band
MIM	metal-insulator-metal capacitor
MOS	metal oxide semiconductor
NF	noise figure
PA	power amplifier
PDK	process development kit
PLL	phase-locked loop
PRBS	pseudo-random bit sequence
PSK	phase shift keying
PVT	process, voltage and temperature
QAM	quadrature amplitude modulation

QPSK	quadrature phase shift keying
RF	radio frequency
SiGe	silicon germanium
SILO	switched injection-locked oscillator
SNR	signal-to-noise ratio
SoC	system on a chip
SRO	super-regenerative oscillator
U	unilateral gain
USB	upper side band
VCXO	voltage-controlled crystal oscillator

List of Symbols

$A_{E,min}$	minimum emitter area
A_{in}	input amplitude
A_{out}	output amplitude
$A(\mathrm{j}\omega)$	forward transfer function
$\beta(\mathrm{j}\omega)$	feedback transfer function
β	small-signal current gain
B_{fm}	radar chirp bandwidth
BV_{CEO}	collector-emitter breakdown voltage
c	speed of light
C	commonly used for capacitors
C_π	intrinsic base-emitter capacitance
D	duty cycle
D_{sw}	switching duty cycle
ΔR	radar range resolution
f_{3dB}	3 dB corner frequency
f_{IF}	signal frequency at IF port of a mixer
f_{inj}	SRO input frequency
f_{LO}	signal frequency at LO port of a mixer
f_{osc}	SRO oscillation frequency
f_{RF}	signal frequency at RF port of a mixer
f_{sw}	SRO quench frequency
f_T	transit frequency
f_{max}	maximum oscillation frequency
G_L	loop gain
$G_{SRO,max}$	maximum SRO gain
I_0	tail current
I_C	collector current
$I_{c,opt}$	optimum collector current for minimum NF
I_{diff}	differential current in the cross-coupled pair
I_{ref}	reference current
I_S	saturation current
κ	cross-coupling feedback factor
λ	wavelength
L	commonly used for inductors
NF_{SSB}	single-side-band noise figure
ω_0	natural resonance angular frequency
ω_{in}	input angular frequency
P_{1dB}, IP_{1dB}	input-referred 1-dB compression point power

P_{dc}, P_{DC}	dc power consumption
$P_{dc,ON}$	dc power consumption in case of free-running SRO
P_{inj}	SRO input power
$P_{inj,min}$	SRO input sensitivity, minimum detectable signal
P_{LO}	signal power at LO port of a mixer
P_{out}	output power
$P_{out,max}$	maximum steady-state output power
$P_{out,pk}, P_{env,max}$	peak value of spectral power
P_{RF}	signal power at RF port of a mixer
ϕ_{in}	initial phase of the input signal
ϕ_{out}	initial phase of the output signal
R	commonly used for resistors
$R_{s,opt}$	real part of optimum impedance for minimum NF
S_{ij}	scattering parameters for ports i and j
t_d	SRO start-up delay time
T_{on}	SRO ON time before quenching
$T_{on,lin}$	SRO ON time in linear mode
$T_{on,log}$	SRO ON time in logarithmic mode
t_r	SRO start-up time to reach 90% of steady-state level
T_{sw}	SRO quench cycle period
τ	time constant
V_{be}, V_{BE}	base-emitter voltage
V_{in}	input voltage
V_{ctrl}	control voltage
V_{ENV}	output voltage envelope
V_{out}	output voltage
V_{p-p}	peak-to-peak voltage swing
V_{sw}, V_{SW}	quench signal voltage
V_T	thermal voltage
V_{tune}	tuning voltage
Z_0	characteristic impedance of a transmission line

List of Figures

List of Tables

Curriculum Vitae

Hatem Ghaleb,
born on 23/06/1987 in Cairo, Egypt.
E-mail: hatem.ghaleb@tu-dresden.de,
hatem.ghaleb@gmail.com.

Education

2014 – 2020	Ph.D. in Electrical Engineering from Technische Universität Dresden, Dresden, Germany.
2009 – 2011	M.Sc. in Communications Technology from Universität Ulm, Ulm, Germany.
2004 – 2009	B.Sc. in Information Engineering and Technology from Germany University in Cairo (GUC), Cairo, Egypt.
2001 – 2004	Cambridge International General Certificate of Secondary Education (IGCSE) from Modern Education Schools, Cairo, Egypt.

Work Experience

06/2020 – present	Radar System & Applications Engineer at NXP Semiconductors Germany GmbH, Munich, Germany.
11/2014 – 04/2020	mm-Wave IC Designer and Ph.D. Candidate at Technische Universität Dresden, Dresden, Germany.
08/2011 – 09/2014	RF Design Consultant at Rohde & Schwarz, on behalf of VISPIRON Engineering GmbH, Munich, Germany.
04/2010 – 09/2010	Radar Sensor Frontend Trainee at Continental AG, Lindau, Germany.

Interests

Piano and rock keyboards, music in general, travel, learning languages, running, technology and human rights.